


For Reference

NOT TO BE TAKEN FROM THIS ROOM

Ex libris
UNIVERSITATIS
ALBERTAENSIS





Digitized by the Internet Archive
in 2022 with funding from
University of Alberta Library

<https://archive.org/details/John1984>

T H E U N I V E R S I T Y O F A L B E R T A

RELEASE FORM

NAME OF AUTHOR BOBAN KURIAKOSE JOHN

TITLE OF THESIS PART 1: DENSITY MATRIX SIMULATION OF TWO-
DIMENSIONAL AND MULTIPLE-PULSE
NMR EXPERIMENTS.

PART 2: NUCLEAR RELAXATION STUDY OF
HEXAMETHYLPHOSPHORAMIDE

DEGREE FOR WHICH THESIS WAS PRESENTED Ph.D.

YEAR THIS DEGREE GRANTED 1984

Permission is hereby granted to THE UNIVERSITY OF ALBERTA LIBRARY to reproduce single copies of this thesis and to lend or sell such copies for private, scholarly or scientific research purposes only.

The author reserves other publication rights, and neither the thesis nor extensive extracts from it may be printed or otherwise reproduced without the author's written permission.

THE UNIVERSITY OF ALBERTA

PART 1: DENSITY MATRIX SIMULATION OF TWO-DIMENSIONAL
AND MULTIPLE-PULSE NMR EXPERIMENTS

PART 2: NUCLEAR RELAXATION STUDY OF
HEXAMETHYLPHOSPHORAMIDE

by



BOBAN KURIAKOSE JOHN

A THESIS

SUBMITTED TO THE FACULTY OF GRADUATE STUDIES AND RESEARCH
IN PARTIAL FULFILMENT OF THE REQUIREMENTS FOR THE DEGREE
DOCTOR OF PHILOSOPHY

DEPARTMENT OF CHEMISTRY

EDMONTON, ALBERTA

FALL, 1984

THE UNIVERSITY OF ALBERTA
FACULTY OF GRADUATE STUDIES AND RESEARCH

The undersigned certify that they have read, and recommend to the Faculty of Graduate Studies and Research, for acceptance, a thesis entitled PART 1: DENSITY MATRIX SIMULATION OF TWO-DIMENSIONAL AND MULTIPLE-PULSE NMR EXPERIMENTS; PART 2: NUCLEAR RELAXATION STUDY OF HEXA METHYL PHOSPHORAMIDE submitted by BOBAN KURIAKOSE JOHN in partial fulfilment of the requirements for the degree of DOCTOR OF PHILOSOPHY.

TO MY LOVED ONES

ABSTRACT

This thesis consists of two parts:

Part 1: Density Matrix Simulation of Two-Dimensional and Multiple-Pulse Experiments

A simulation program to analyze multiple-pulse and two-dimensional FT NMR experiments using density matrix theory has been implemented. The program computes analytical expressions for NMR signals arising from an $I_m S_n$ spin system (where I and S are spin 1/2 nuclei and $1 \leq n, m \leq 3$), after the application of a pulse sequence specified by the input data. The simulation program has been designed to be quite general and incorporates a number of features including irradiation from a broadband decoupler, effects of phase cycling of the pulses and receiver, and pulses of any given flip angle.

The state of a spin system during a multiple-pulse experiment is followed by monitoring the evolution of the density matrix. During each step in the sequence, the effective Hamiltonian operator will be time independent in a suitable rotating frame, and the equation of motion for the density matrix in this frame can be solved in a straightforward manner. The evolution of the density matrix through a pulse sequence is thereby reduced to a series of successive transformations on the density

matrix. The simulation program has been implemented in such a manner that the transformations of the density matrix, under radiofrequency pulses, free-precession periods, periods of broadband decoupling, etc., are effected by various independent program modules which have access to the density matrix data structure.

A detailed investigation of the effects of ordinary noise decoupling and spherical randomization decoupling on the elements of the density matrix for $I_m S_n$ spin systems has been carried out. It has been shown that under strong decoupler irradiation, the density matrix elements reach steady state values in the rotating frame of the decoupled nuclei. The steady state values are found to be linear combinations of the density matrix at the beginning of the decoupling period, and often involve mixing of populations with multiple quantum coherences, and mixing of the perpendicular components of the magnetization with higher coherences. The transformation of the density matrix during the decoupling period is carried out by the linear combination procedure using coefficients stored in the program.

The application of the program in the analysis of multiple-pulse and two-dimensional experiments has been demonstrated by simulating the distortionless enhanced polarization transfer (DEPT) experiment, a two-dimensional

version of the DEPT experiment for multiplet-selective heteronuclear shift correlation, the INADEQUATE experiment and three variants of the gated decoupler 2D J- δ resolved experiment which illustrate certain unexpected effects of spin decoupling. These examples demonstrate the usefulness of the program in simulating experiments in which the spin dynamics cannot always be followed using classical magnetization vector diagrams.

Part 2: Nuclear Relaxation Study of HexaMethyl-
Phosphoramidate

The spin-lattice relaxation times of ^{31}P , ^{14}N and ^1H in hexamethylphosphoramidate (HMPA) and of ^{31}P and ^2H in the deuterated analog (HMPD) have been measured over the temperature range 290 K - 450 K. The relaxation of the ^{31}P nucleus in HMPD has been assumed to be entirely due to spin-rotation interactions and the angular momentum correlation time (τ_J) has been determined. It has been found that the quadrupolar interaction in ^{14}N in HMPA is modulated by a time dependence characterized by two correlation times: the overall molecular tumbling correlation time (τ_θ) and that for the internal rotation about the P-N bond (τ_i^{PN}). τ_θ was determined using the Hubbard relation with τ_J obtained from the ^{31}P data in HMPD. τ_i^{PN} has been determined from the ^{14}N data. The

activation energy for the internal motion was found to be 3.4 ± 0.2 kcal/mole.

The relaxation rate of ^2H in HMPD was found to be governed by three correlation times: τ_θ , τ_i^{PN} and that for the rotation of CD_3 groups (τ_i^{CN}). The rotation of CD_3 groups was found to possess a relatively high activation energy 3.0 ± 0.1 kcal/mole. The delineation of the contributions to the relaxation rate of ^{31}P in HMPA was carried out using the above results and data from the temperature studies of the diffusion coefficient of HMPA.

ACKNOWLEDGEMENTS

I take this opportunity to express my deep gratitude to Professor R.E.D. McClung for his guidance and enthusiasm during the course of this work. He has patiently spent countless hours leading me through the rough terrain of density matrix and spin relaxation theories.

I owe special gratitude to Dr. T.T. Nakashima for many stimulating discussions and collaboration in many experiments.

I am also grateful to Professor R.B. Jordan for his help with instrumentation and experimental aspects.

I thank Dr. J. Ripmeester for measuring the phosphorus spectrum of solid hexamethylphosphoramide.

Special thanks are due to Annabelle Wiseman for her expert help in typing this manuscript.

To all my friends, I express my sincere appreciation, especially to Dipak Ghosh and Swapan Chowdhury for their continuous support.

Financial assistance from the Department of Chemistry and Natural Science and Engineering Research Council of Canada is gratefully acknowledged.

TABLE OF CONTENTS

CHAPTER		PAGE
PART 1:	DENSITY MATRIX SIMULATION OF TWO-DIMENSIONAL AND MULTIPLE-PULSE NMR EXPERIMENTS.....	1
I.	APPLICATION OF DENSITY MATRIX THEORY IN PULSED FT NMR	2
I.1	Introduction.....	2
I.2	Definition of Density Matrix and Equations for Physical Observables.....	3
I.3	Equation of Motion of the Density Matrix.....	5
I.4	Rotating Frame Transformation.....	7
I.5	Inclusion of Relaxation Effects and Chemical Exchange.....	12
I.6	Density Matrix Method and Bloch Equations Approach.....	14
I.7	Applications to Pulsed FT NMR.....	17
I.8	Analysis of a Simple FT Experiment.....	22
I.9	Summary.....	28
II.	DESCRIPTION OF THE SIMULATION PROGRAM.....	30
II.1	Introduction.....	30
II.2	Objectives of the Simulation Program....	31

CHAPTER		PAGE
II.3	Implementation of the Simulation Program.....	33
	a. Description of Input Commands.....	39
II.4	Choice of Basis Set.....	49
II.5	Construction of Spin Operator Representation Matrices.....	50
II.6	Computation of the Thermal Equilibrium Density Matrix.....	53
II.7	Transformation of the Density Matrix by rf Pulse Operators.....	55
II.8	Transformation of the Density Matrix During Free Precession Periods.....	61
II.9	Transformation of Density Matrix During Broad-Band Decoupling.....	62
II.10	Computation and Simplification of Signal Expressions.....	63
II.11	Identification of ν_I and ν_S as Frequency Offsets from Transmitter.....	66
II.12	Other Features of the Simulation Program.....	75
II.13	Limitations of and Suggested Extensions to the Simulation Program.....	76
II.14	Summary.....	78

CHAPTER	PAGE
III. THEORY AND IMPLEMENTATION OF THE HETERONUCLEAR NOISE DECOUPLING SCHEME.....	80
III.1 Introduction.....	80
III.2 Theoretical Treatment.....	81
a. IS_2 Spin System.....	83
b. IS and IS_3 Spin Systems.....	91
c. Spherical Randomization Decoupling..	95
III.3 General Effects of Noise Decoupling on the Density Matrix.....	100
III.4 Implementation of the Decoupling Scheme.....	102
III.5 Summary.....	104
IV. APPLICATIONS.....	106
IV.1 Introduction.....	106
IV.2 Simulation of Experiments.....	107
a. DEPT Experiment.....	107
b. Selective 2D Heteronuclear Shift Correlation Experiment.....	130
c. INADEQUATE Experiment.....	140
d. Unexpected Effects of Spin Decoupling.....	149
IV.3 Summary.....	174

CHAPTER	PAGE
PART 2: NUCLEAR RELAXATION STUDY OF HEXAMETHYL-	
PHOSPHORAMIDE.....	176
V. DESCRIPTION OF SPIN RELAXATION MECHANISMS.....	177
V.1 Introduction.....	177
V.2 Spin Relaxation and Applications of Relaxation Studies.....	177
V.3 Spin Relaxation Mechanisms.....	182
a. Dipolar Interactions.....	184
1. Random Rotation.....	186
2. Translational Motion.....	188
b. Spin-Rotation Interaction.....	189
c. Nuclear Quadrupole Interaction.....	191
V.4 Brief Review of Rotational Diffusion Models.....	193
V.5 Objectives of the Project.....	198
V.6 Summary.....	199
VI. EXPERIMENTAL.....	200
VI.1 Introduction.....	200
VI.2 Sample Preparation.....	200
VI.3 Instrumentation.....	201
VI.4 Measurement of T_1 Relaxation Time.....	204
a. Inversion Recovery Experiment.....	204
b. Triplet Sequence.....	205

CHAPTER		PAGE
VI.5	Measurement of Translational Diffusion Coefficients.....	207
VI.6	Summary.....	211
VII.	RESULTS AND DISCUSSION.....	212
VII.1	Introduction.....	212
VII.2	^{31}P T_1 (HMPD) Results and Analysis.....	212
VII.3	^{14}N T_1 Results and Analysis.....	221
VII.4	^2H T_1 Results and Analysis.....	230
VII.5	^{31}P T_1 (HMPA) Results and Analysis.....	236
	a. Calculation of Spin-Rotation Relaxation Rates.....	239
	b. Calculation of Intermolecular Dipolar Relaxation Rates.....	241
	c. Calculation of the Intramolecular Dipole Relaxation Rates.....	243
	d. Comparison of Calculated and Experimental Relaxation Rates.....	244
VII.6	Conclusions.....	246
VII.7	Summary.....	249

REFERENCES.....	250
-----------------	-----

LIST OF TABLES

TABLE	DESCRIPTION	PAGE
1	Program input format for density matrix elements.....	49
2	Relaxation data and results for ^{31}P in HMPD.....	214
3	Relaxation data and results for ^{14}N in HMPA.....	222
4	Relaxation Data and Results for ^2H Nucleus.....	231
5	Relaxation Data for ^{31}P in HMPA.....	238
6	Comparison of calculated and observed ^{31}P relaxation rates in HMPA.....	241
7	Translational diffusion coefficients of HMPA.....	242

LIST OF FIGURES

FIGURE	DESCRIPTION	PAGE
1	Block diagram of the simulation program....	37
2	Pulse sequence for calibration of pulse width.....	68
3	Pulse sequence and input data for simulation of the CH DEPT experiment.....	108
4	Output of the DEPT simulation for CH system.....	110
5	Magnetization diagrams for CH DEPT experiment.....	112
6	Input data and output from the simulation of CH coupled DEPT experiment...	118
7	Simulation of θ -pulse angle dependence in CH DEPT experiment.....	119
8	Density matrix and output from the simulation of CH ₂ DEPT experiment.....	121
9	Density matrix and output from the simulation of CH ₃ DEPT experiment.....	122
10	Magnetization diagrams for CH ₂ DEPT experiment.....	123
11	Magnetization diagrams for CH ₃ DEPT experiment.....	124

FIGURE	DESCRIPTION	PAGE
12	Output from the simulation of CH ₂ coupled DEPT experiment.....	126
13	Simulation of θ -pulse angle dependence in CH ₂ DEPT experiment.....	127
14	Output from the simulation of CH ₃ coupled DEPT experiment.....	129
15	Simulation of θ -pulse angle dependence in CH ₃ DEPT experiment.....	130
16	The selective 2D heteronuclear chemical shift correlation pulse sequence.....	132
17	Input data and output from the simulation of CH selective shift correlation experiment.....	134
18	Input data and output from the simulation of CH ₂ selective shift correlation experiment.....	135
19	Input data and output from the simulation of CH ₃ selective shift correlation experiment.....	136
20	Input data and output from the 4-phasecycle CH selective shift correlation experiment.....	139

FIGURE	DESCRIPTION	PAGE
21	Pulse sequence and input data for simulation of the INADEQUATE experiment on ^{13}C - ^{13}C fragment.....	141
22	Output data from simulation of INADEQUATE experiment on ^{13}C - ^{13}C fragment.....	143
23	Output data from simulation of INADEQUATE experiment on ^{13}C - ^{12}C fragment..	146
24	Output data from simulation of INADEQUATE experiment on ^{13}C - ^{13}C - ^{13}C fragment.....	148
25	2D gated decoupler ^{13}C J- δ resolved pulse sequences.....	152
26	Input data and output from simulation of gated decoupler pulse sequences A and B on CH system.....	154
27	Output data from simulation of gated decoupler pulse sequence A on CH_2 system...	155
28	Output data from simulation of gated decoupler pulse sequence B on CH_2 system...	156
29	Output data from simulation of gated decoupler pulse sequences A and B on CH_3 system.....	157

FIGURE	DESCRIPTION	PAGE
30	2D J- δ resolved spectrum of 2-butanol obtained with pulse sequence C (with decoupled acquisition).....	163
31	Input data and output from simulation of gated decoupler pulse sequence C (with decoupled acquisition) on CH system.....	164
32	Output data from simulation of gated decoupler pulse sequence C (with decoupled acquisition) on CH ₂ system.....	165
33	Output data from simulation of gated decoupler pulse sequence C (with decoupled acquisition) on CH ₃ system.....	166
34	2D J- δ resolved spectrum of 2-butanol obtained with pulse sequence C (with coupled acquisition).....	170
35	Output data from simulation of gated decoupler pulse sequence C (with coupled acquisition) on CH system.....	171
36	Output data from simulation of gated decoupler pulse sequence C (with coupled acquisition) on CH ₂ system.....	173
37	Output data from simulation of gated decoupler pulse sequence C (with coupled acquisition) on CH ₃ system.....	174

FIGURE	DESCRIPTION	PAGE
38	Observed relaxation rates of ^{31}P in HMPD...	215
39	Observed ^{31}P spectrum of solid HMPD.....	219
40	Observed relaxation rates of ^{14}N in HMPA...	223
41	Variation of τ_θ with τ_J for HMPD.....	227
42	Observed relaxation rates of ^2H in HMPD....	232
43	Comparison of calculated and observed ^{31}P relaxation rates in HMPA.....	237

"The outcome of any serious research can only be to make two questions grow where only one grew before."

Thorstein Veblen, 1919

PART 1

DENSITY MATRIX SIMULATION OF TWO-DIMENSIONAL AND
MULTIPLE-PULSE NMR EXPERIMENTS

CHAPTER I

APPLICATION OF DENSITY MATRIX THEORY IN PULSED FT NMR

I.1 Introduction

This chapter discusses the application of the density matrix method in analyzing pulsed FT NMR experiments. A brief review of the basic aspects of density matrix theory is given, starting with the definition of the density matrix, prescriptions for the derivation of physical observables from the density matrix, the equation of motion of the density matrix and its solution, followed by a discussion of the incorporation of relaxation and chemical exchange phenomena into the equation of motion. The differences between the density matrix method and the classical approach, Bloch equations, are pointed out. Finally, the application of density matrix theory to pulsed FT NMR experiments is illustrated by following the evolution of the density matrix through a typical pulsed FT NMR experiment.

I.2 Definition of Density Matrix and Equations for Physical Observables

The time-dependent Schroedinger equation for a system described by a wavefunction Ψ is given by

$$\hat{H}\Psi = i\hbar \frac{\partial \Psi}{\partial t} , \quad [1-1]$$

where \hat{H} is the total Hamiltonian of the system (1). The wavefunction Ψ can be represented in a complete orthonormal basis set $\{|m\rangle\}$ as

$$\Psi(t) = \sum_m C_m(t) |m\rangle , \quad [1-2]$$

where $C_m(t)$ are time-dependent coefficients.

The value of any observable property O , associated with the corresponding quantum mechanical operator \hat{O} , is given by (1,2)

$$Q(t) = \langle \Psi(t) | \hat{O} | \Psi(t) \rangle \quad [1-3]$$

$$= \sum_{m,n} C_m^*(t) C_n(t) \langle m | \hat{O} | n \rangle .$$

Since $Q(t)$ is given in terms of products of coefficients, it is convenient to define a matrix \tilde{P} whose elements are the products of coefficients arranged so as to give

$$P_{ij} = C_i(t) C_j^*(t) . \quad [1-4]$$

Equation [1-3] can then be written as

$$Q(t) = \sum_{m,n} P_{nm}(t) \langle m | \hat{Q} | n \rangle \quad [1-5]$$

$$= \sum_{m,n} P_{nm}(t) Q_{mn} = \sum_n (\hat{P}(t) \hat{Q})_{nn} = \text{Trace}(\tilde{P}(t) \tilde{Q}) .$$

Equation [1-5] describes the property $Q(t)$ for a particular molecule, but experimental measurements give the average $\langle Q(t) \rangle$ per molecule in the ensemble. Averaging over the ensemble, we obtain

$$\langle Q(t) \rangle = \text{Trace} (\tilde{\rho}(t) \tilde{Q}) , \quad [1-6]$$

where the density matrix $\tilde{\rho}(t)$ is the ensemble average of $\tilde{P}(t)$ and has elements

$$\rho_{ij}(t) = \overline{C_i(t) C_j(t)^*} ,$$

where the bar denotes an ensemble average (1,2). Equation [1-6] gives the prescription for deriving average values of properties from the density matrix $\tilde{\rho}(t)$.

The density matrix ρ is the quantum mechanical analog of the classical ensemble density. ρ contains all of the time dependence of the system and defines the system completely. The density matrix ρ is the representation of the density operator $\hat{\rho}$ in a particular basis set, with elements

$$\rho_{ij} = \langle i | \hat{\rho} | j \rangle .$$

Since the representation of any operator depends on the particular basis set used, the density matrix has different forms when represented in different basis sets. Although the form of the matrices, ρ and Q depend on the particular basis set chosen, the trace of their product, i.e. the average value of the observable, is independent of the basis set. Hence the density operator can be represented in any convenient basis set.

I.3 Equation of Motion of the Density Matrix

The time-dependence of the density matrix can be ascertained from the time-dependent Schroedinger equation. The time derivative of the density matrix element ρ_{nm} is given by

$$\frac{d\rho_{nm}}{dt} = \overline{C_n(t) \frac{dC_m^*(t)}{dt}} + \overline{\frac{dC_n(t)}{dt} C_m^*(t)} . \quad [1-7]$$

From Equations [1-1] and [1-2], one obtains

$$\sum_m C_m \hat{H} |m\rangle = i\hbar \sum_m \frac{dC_m}{dt} |m\rangle , \quad [1-8]$$

from which the time derivatives of the coefficients $C_n(t)$ can be obtained as

$$i\hbar \frac{dC_n}{dt} = \sum_{m'} C_{m'} \langle n | \hat{H} | m' \rangle$$

and [1-9]

$$-i\hbar \frac{dC_n^*}{dt} = \sum_{m'} C_{m'}^* \langle m' | \hat{H} | n \rangle .$$

Substitution of Equation [1-9] into [1-7] gives

$$\frac{d\rho_{nm}}{dt} = \frac{1}{i\hbar} \sum_{m'} \overline{C_{m'} C_m^*} \langle n | \hat{H} | m' \rangle - \frac{1}{i\hbar} \sum_{m'} \overline{C_n C_{m'}^*} \langle m' | \hat{H} | m \rangle ,$$

which can be rearranged to give

$$\frac{d\rho_{nm}}{dt} = \frac{i}{\hbar} \{ [\rho, H] \}_{nm} ,$$

or, in operator form, as (1)

$$\frac{d\hat{\rho}}{dt} = \frac{i}{\hbar} [\hat{\rho}, \hat{H}] . \quad [1-10]$$

In the absence of any explicit time dependence in \hat{H} , the solution to Equation [1-10] is given by

$$\hat{\rho}(t) = \exp\{-i\hat{H}t/\hbar\} \hat{\rho}(0) \exp\{i\hat{H}t/\hbar\} , \quad [1-11]$$

where $\hat{\rho}(0)$ is the density operator at time $t = 0$. Provided the Hamiltonian \hat{H} is time-independent, the density matrix at any further instant in time can be computed from the matrix representation of Equation [1-11].

I.4 Rotating Frame Transformation

When the Hamiltonian contains a periodically time-dependent term, the equation of motion for $\hat{\rho}$ is solved by transforming the density operator into a suitable rotating frame so that the effective Hamiltonian in the rotating frame is time-independent. When the Hamiltonian $\hat{H}(t)$ is expressed as

$$\hat{H}(t) = \hat{H}_0 + \hat{H}_1(t) ,$$

the equation of motion for the density operator is given by

$$\frac{d\hat{\rho}}{dt} = \frac{i}{\hbar} [\hat{\rho}, \hat{H}_0 + \hat{H}_1(t)] . \quad [1-12]$$

In a frame rotating at frequency ω about the laboratory z-axis, the density operator $\hat{\rho}^*(t)$ is related to the laboratory frame density operator by

$$\hat{\rho}^*(t) = \exp(-i\omega\hat{I}_z t) \hat{\rho}(t) \exp(i\omega\hat{I}_z t) , \quad [1-13]$$

where \hat{I}_z is the z-component of the total spin angular momentum of the system. The equation of motion for $\hat{\rho}^*$ is obtained from Equation [1-12] by recognizing that

$$\frac{d\hat{\rho}^*}{dt} = i[\hat{\rho}^*, \omega\hat{I}_z] + \exp(-i\omega\hat{I}_z t) \frac{d\hat{\rho}}{dt} \exp(i\omega\hat{I}_z t). \quad [1-14]$$

One obtains

$$\frac{d\hat{\rho}^*}{dt} = \frac{i}{\hbar} [\hat{\rho}^*, \hat{H}_0 + \hbar\omega\hat{I}_z + \hat{H}_1^*(t)] \quad [1-15]$$

where

$$\hat{H}_1^*(t) = \exp(-i\omega\hat{I}_z t) \hat{H}_1(t) \exp(i\omega\hat{I}_z t) \quad [1-16]$$

is the time-dependent interaction in the rotating frame. In all cases of interest in magnetic resonance, $\hat{H}_1^*(t)$ has a time-independent part which causes important changes in $\hat{\rho}^*$, and a time-dependent part which is far off-resonance and has no influence on the magnetizations of the system. One therefore takes the equation of motion for $\hat{\rho}^*$ to be

$$\frac{d\hat{\rho}^*}{dt} = \frac{i}{\hbar} [\hat{\rho}^*, \hat{H}_{\text{eff}}] , \quad [1-17]$$

where $\hat{H}_{\text{eff}} = \hat{H}_0 + \hbar\omega\hat{I}_z$ + time-independent part of \hat{H}_1^* .

Since \hat{H}_{eff} is time-independent, the solution to Equation [1-17] is given by

$$\hat{\rho}^*(t) = \exp(-i\hat{H}_{\text{eff}}t/\hbar) \hat{\rho}^*(0) \exp(i\hat{H}_{\text{eff}}t/\hbar) \quad [1-18]$$

and the density operator in the laboratory frame will be

$$\hat{\rho}(t) = \exp(i\omega\hat{I}_zt) \hat{\rho}^*(t) \exp(-i\omega\hat{I}_zt) . \quad [1-19]$$

It is instructive to illustrate some of the features of the rotating frame transformation by considering some simple nuclear magnetic resonance experiments on a single

spin 1/2 particle. The following examples also serve to illustrate the similarities between this quantum mechanical rotating frame and the rotating frames introduced in the solution of the Bloch equations. First, the case of a time-independent Hamiltonian is considered. The spin 1/2 particle is subjected to a constant magnetic field of strength H_0 , along the z-axis. The Hamiltonian for this system can be written as

$$\begin{aligned}\hat{H}_0 &= -\gamma\hbar H_0 \hat{I}_z \\ &= -\hbar\omega_0 \hat{I}_z ,\end{aligned}\tag{1-20}$$

where ω_0 is the Larmor frequency (in radians sec^{-1}), γ is the magnetogyric ratio of the nucleus, and \hat{I}_z is the z-component of the nuclear spin angular momentum operator. The Hamiltonian operator of the system in the frame rotating at angular frequency ω , is given by

$$\begin{aligned}\hat{H}_{\text{eff}} &= \hat{H}_0 + \hbar\omega \hat{I}_z \\ &= -\hbar(\omega_0 - \omega) \hat{I}_z .\end{aligned}\tag{1-21}$$

When the system is exactly "on resonance", $\omega_0 = \omega$ and $\hat{H}_{\text{eff}} = 0$. This leads to the result (Equation [1-17])

$$\frac{d\hat{\rho}^*}{dt} = 0 , \quad [1-22]$$

which implies that $\hat{\rho}^*$ is time-independent (in the rotating frame). The Bloch equations give exactly the same result in terms of magnetization vectors in the classical rotating frame (3,4).

The case where the Hamiltonian has a periodic time-dependence will now be considered. The system is subjected to an additional oscillating radio frequency field in a direction perpendicular to the constant field H_0 . The Hamiltonian is given by

$$\hat{H} = -\hbar\omega_0\hat{I}_z - \gamma\hbar H_1 \cos \omega t \hat{I}_x , \quad [1-23]$$

where H_1 is the amplitude of the time-dependent magnetic field oscillating at a frequency ω . Transformation into the rotating frame yields (Equation [1-16])

$$\hat{H}_1^* = -\frac{\gamma\hbar H_1 \hat{I}_x}{2} - \frac{\gamma\hbar H_1}{2} (\hat{I}_x \cos 2\omega t - \hat{I}_y \sin 2\omega t). \quad [1-24]$$

The first term in Equation [1-24] is time-independent and is the "on resonance" component of the rf field. The last term represents a field oscillating at frequency 2ω in the opposite direction. This counter-rotating component is

far from resonance and has virtually no effect on the magnetizations. The last term can therefore be neglected. The effective Hamiltonian in the rotating frame is then written as

$$\hat{H}_{\text{eff}} = -\hbar(\omega_0 - \omega) \hat{I}_z - \frac{\gamma \hbar H_1}{2} \hat{I}_x, \quad [1-25]$$

where \hat{H}_{eff} is time-independent. For the exact "on-resonance" condition, it reduces to

$$\hat{H}_{\text{eff}} = \frac{-\gamma \hbar H_1}{2} \hat{I}_x. \quad [1-26]$$

Equation [1-26] shows that, at resonance, the effective field in the rotating frame is just the H_1 field along the x-axis. Bloch equations also give the same result.

I.5 Inclusion of Relaxation Effects and Chemical Exchange

The effect of spin relaxation caused by a stationary random perturbation $\hat{H}_1(t)$, has been incorporated into the equation of motion of the density matrix by Redfield (5). Using perturbation theory and making use of the ensemble average properties of $H_1(t)$, he has shown that the equation of motion of the density matrix due to relaxation is given by

$$\left(\frac{d\rho_{\alpha\alpha'}}{dt}\right)_{\text{relaxation}} = \sum_{\beta, \beta'} R_{\alpha\alpha'; \beta\beta'} (\rho_{\beta\beta'} - \rho_{\beta\beta'}^0) , \quad [1-27]$$

where $R_{\alpha\alpha'; \beta\beta'}$ is the relaxation matrix element given by

$$R_{\alpha\alpha'; \beta\beta'} = \frac{1}{2\hbar} [J_{\alpha\beta\alpha', \beta'}(\alpha' - \beta') + J_{\alpha\beta\alpha', \beta}(\alpha - \beta) - \delta_{\alpha'\beta'} \sum_{\gamma} J_{\gamma\beta\gamma\alpha}(\gamma - \beta) - \delta_{\alpha\beta} \sum_{\gamma} J_{\gamma\alpha'\gamma\beta'}(\gamma - \beta')] , \quad [1-28]$$

where $\alpha - \beta$ is the frequency corresponding to the transition states α and β , and $J_{\alpha\alpha', \beta\beta'}(\omega)$ are the spectral densities (1),

$$J_{\alpha\alpha', \beta\beta'}(\omega) = \overline{\int_{-\infty}^{\infty} \langle \alpha | \hat{H}_1(t) | \alpha' \rangle \langle \beta' | \hat{H}_1(t+\tau) | \beta \rangle e^{-i\omega\tau} d\tau} [1-29]$$

where the bar indicates an ensemble average.

The equation of motion of the density operator has been further modified to account for the chemical exchange processes (6). A chemical exchange process has the effect of permuting the nuclear spin states, and the average rate of change of the density operator can be given by

$$\left(\frac{d\hat{\rho}}{dt}\right)_{\text{exchange}} = \frac{1}{\tau} (\hat{P}\hat{\rho}\hat{P}^+ - \hat{\rho}) , \quad [1-30]$$

where an exchange event occurs on the average every τ seconds and \hat{P} is the permutation operator. This approach to chemical exchange is elegant for simple product basis sets, but tends to be complicated when product bases are unsuitable (strongly coupled systems).

I.6 Density Matrix Method and Bloch Equations Approach

The Bloch equations provide the classical description of the motion of non-interacting spins. These equations (1,3,4), are the equations of motion for the magnetization components M_x , M_y and M_z , in the presence of relaxation effects:

$$\frac{dM_z}{dt} = \gamma(\vec{M} \times \vec{H})_z + \frac{M_0 - M_z}{T_1} ,$$

$$\frac{dM_x}{dt} = \gamma(\vec{M} \times \vec{H})_x - \frac{M_x}{T_2} , \quad [1-31]$$

$$\frac{dM_y}{dt} = \gamma(\vec{M} \times \vec{H})_y - \frac{M_y}{T_2} ,$$

where M_0 is the thermal equilibrium magnetization and T_1 and T_2 are the longitudinal and transverse relaxation times respectively.

The Bloch equations can be derived from density matrix theory in some situations by evaluating the expressions for the expectation values of the magnetization components. Both methods, the density matrix theory and Bloch equations approach, yield identical results, in the description of many experiments, for the observable components of magnetization in weakly coupled spin systems. However, the applicability of the Bloch equations is limited. Some of the major differences between these methods are amplified in the following:

(i) Exact expressions for the relaxation terms can be derived using the density matrix method, as was done in the Redfield relaxation equations. In contrast, the relaxation terms included in the Bloch equations are purely empirical. The inclusion of these terms is justifiable only because they seem to explain experimental observations. Density matrix theory provides, in addition, the conditions under which the Bloch equations are applicable.

(ii) The classical description of NMR experiments, given by the Bloch equations, are not applicable for strongly coupled spins. Here it is necessary to introduce quantum mechanical energy levels and operators rather than classical magnetization vectors. For weakly coupled spin systems, the simple products of the eigenfunctions of the

separated spins are eigenfunctions of the time-independent Hamiltonian \hat{H}_0 for the complete spin system, and hence the transitions between various energy levels are identifiable as corresponding to the spin flips of individual nuclei. In such cases it is possible to write down Bloch equations for the magnetization components of each individual nucleus. However, in strongly coupled spin systems, the simple product functions are not eigenfunctions of the Hamiltonian H_0 and the transitions cannot be identified as arising from the spin flip of any particular nuclei. Density matrix theory must be used to describe the time dependence of such strongly coupled spin systems.

(iii) The Bloch equations are concerned only with magnetization components (one quantum coherences), not with zero quantum and multiple quantum coherences, and hence fail to describe the creation and evolution of these invisible (directly unobservable) coherences in multiple-pulse experiments. These coherences can be produced in a spin system initially at thermal equilibrium by application of two radiofrequency pulses separated by a delay (7). Multiple quantum coherence phenomena have been utilized in multiple pulse and two dimensional FT experiments to provide additional information about the spin system. In such situations, the density matrix theory must be used in order to describe the signals and the quantum mechanical state of the system.

I.7 Applications to Pulsed FT NMR

The density matrix theory can be used to describe pulsed FT and CW NMR experiments. Since the theory is capable of explaining the origin and behaviour of multiple quantum coherences, it is especially useful in the analysis of many multiple pulse FT experiments. However, the explicit computation of the density matrix can become tedious depending on the size of the spin system and the pulse sequence employed.

A typical pulsed FT NMR experiment consists of the application of a set of pulses to the spin system, separated by periods of free precession followed by an acquisition period where the transverse components of the magnetizations are sampled. The pulses may act on all nuclei (homonuclear systems) or may be selective and act only on one group of nuclei (heteronuclear systems). The flip angles and phases of the pulses, duration of the free precession periods, spin decoupling during precession and/or acquisition periods, etc., can be used to select the information about the spin system which is obtained in the measured response. The transverse components of the magnetization are measured as a time varying signal referred to as the free induction decay (FID). In order

to improve the signal-to-noise ratio, the signals from a number of scans are co-added to obtain the final FID. During the individual scans, the phases of the pulses may be varied to suppress undesirable or spurious signals or to correct for pulse-length imperfections, pulse-phase abnormalities, and for differentiating magnetization arising from various orders of coherence, i.e. zero quantum, single quantum, and multiple quantum coherences. The final FID is Fourier transformed to obtain the conventional frequency domain NMR spectrum.

Recently, two dimensional FT experiments have been developed (8). Here the signal is collected as a function of two time variables. It is then Fourier transformed in both time domains to yield a frequency spectrum which is a function of two independent frequency variables (9-12). The advantage of two dimensional experiments over the conventional FT experiments is the simplification of complex spectra which can be achieved by selectively presenting a particular type of spectral information (e.g. chemical shift) along one frequency dimension while simultaneously displaying another spectral parameter (e.g. spin-spin coupling) along the second dimension (13-15). Thus the total information content of the conventional spectrum is partitioned along two dimensions, which greatly simplifies the interpretation of spectra,

particularly those of large molecules. Another application of two dimensional experiments is in correlating the chemical shifts of coupled nuclei in homonuclear and heteronuclear systems (16). The correlation of chemical shifts is effected through some mechanism for magnetization transfer between the nuclei involved (17). The different coupling mechanisms utilized for magnetization transfer are scalar J coupling interaction (18-22), dipole-dipole interactions (23-25), and chemical exchange processes (26,27). Depending on the shift correlation information desired, a two dimensional experiment can be performed utilizing any of the above mechanisms for magnetization transfer. Pulse sequences can also be designed to utilize the multiple quantum coherences in spectrum editing (7,28-30). It is possible, for example, to edit the spectrum so as to differentiate signal components arising from various spin subsystems. This technique has been used to distinguish between signals arising from CH, CH₂, and CH₃ spin systems (31).

Pulse sequences for all types of NMR experiments can be represented as a series of radiofrequency pulses and free precession periods applied to a spin system which is initially at thermal equilibrium. In applying the density matrix theory to the description of these experiments, one begins with the thermal equilibrium density matrix. It is

convenient to choose a basis whose members are the eigenfunctions of \hat{H}_0 , the Hamiltonian operator in the absence of radiofrequency pulses. The Hamiltonian operator corresponding to a multiple pulse experiment would be different at each stage in the pulse sequence. Hence it is preferable to think of the entire pulse sequence as a sequence of steps, such that during any particular step, the Hamiltonian operator has a definite time dependence. The state of the spin system during the experiment can then be followed by monitoring the evolution of the density matrix in each successive step. In a multiple-pulse sequence, there are basically two types of Hamiltonian operators acting on the spin system in a sequential manner: radiofrequency pulses and free precession periods. Solving the equation of motion of the density matrix during the free precession is straightforward since the Hamiltonian is time-independent (Equation [1-11]). The time dependence of the Hamiltonian during the application of an rf pulse can be removed by transforming the system into a rotating frame with an angular frequency equal to the frequency of the rf pulse irradiation and the solution of the equation of motion for the density matrix (Equation [1-17]) is again straightforward (Equation [1-19]).

The time evolution of the density matrix in a multiple pulse sequence can be represented as follows: Let $\hat{\rho}(0)$ be the thermal equilibrium density matrix operator and let $\hat{H}_1, \hat{H}_2, \dots, \hat{H}_n$ be the sequence of Hamiltonian operators representing the pulse sequence. The operators are time-ordered with the earliest one leftmost and successive ones to the right. Here it is assumed that the time-dependence of the operators has been removed by appropriate rotating frame transformation. The final density operator at the end of the pulse sequence is given by

$$\hat{\rho} = \hat{T}_n(\dots(\hat{T}_2(\hat{T}_1\hat{\rho}(0)\hat{T}_1^+)\hat{T}_2^+\dots)\hat{T}_n^+ , \quad [1-32]$$

where \hat{T}_i is the propagator during the i th time interval. Using this prescription it is then possible to follow the evolution of the density operator under any given pulse sequence. However, at the computation stage, it is preferable to work with the matrix representations of the operators rather than the operators themselves since it is easier to apply the matrix transformations rather than evaluate operator transformation equations.

I.8 Analysis of a Simple FT Experiment

The application of density matrix theory in the description of pulsed FT experiments is nicely illustrated by considering the pulse sequence used for routine measurement of spectra. The sequence consists of a 90° pulse followed by signal acquisition. The detailed evolution of $\hat{\rho}$ during this sequence will be considered for an ensemble of systems containing a single spin $1/2$ nucleus.

The system is subjected to a static magnetic field of strength H_0 , along the z axis. The Hamiltonian for the system is given by Equation [1-20] with eigenfunctions $|\alpha\rangle$ and $|\beta\rangle$, corresponding to eigenvalues $-\hbar\omega_0/2$ and $+\hbar\omega_0/2$ respectively. From statistical thermodynamics, the thermal equilibrium density operator $\hat{\rho}(0)$ can be written as

$$\hat{\rho}(0) = (1/z) \exp(-\hat{H}_0/kT) , \quad [1-33]$$

where z is the partition function of the system. The density matrix will be diagonal at thermal equilibrium. In the high temperature limit,

$$\exp(-\hat{H}_0/kT) \cong \hat{1} - \hat{H}_0/kT , \quad [1-34]$$

and the density matrix elements are

$$\rho(0)_{\alpha\alpha} = (1+\Delta)/2, \quad \rho(0)_{\beta\beta} = (1-\Delta)/2 \quad \text{and} \quad \rho(0)_{\alpha\beta} = \rho(0)_{\beta\alpha} = 0,$$

where $\Delta = \gamma\hbar H_0/2kT$.

The magnetization per molecule for the ensemble at thermal equilibrium can now be determined from Equation [1-6] and has components

$$\langle M_i \rangle = \text{Trace} (\rho \tilde{M}_i) ; \quad i = x, y, z, \quad [1-35]$$

where

$$\tilde{M}_i = \gamma\hbar \tilde{I}_i ,$$

and \tilde{I}_i , $i = x, y, z$ are given by the Pauli spin matrices. Evaluation of the magnetization components gives

$$\langle M_x \rangle = 0, \quad \langle M_y \rangle = 0, \quad \text{and} \quad \langle M_z \rangle = (1/2) \gamma\hbar \Delta . \quad [1-36]$$

As expected, the x and y components of the magnetization vanish since the off-diagonal elements of the density matrix are all zero. Note that $\langle M_x \rangle$ is proportional to

$(\rho_{\alpha\beta} + \rho_{\beta\alpha})$ and $\langle M_Y \rangle$ is proportional to $(\rho_{\alpha\beta} - \rho_{\beta\alpha})$ so that transverse magnetizations are present only if ρ has non-zero off-diagonal elements. The value of $\langle M_Z \rangle$ is proportional to $(\rho_{\alpha\alpha} - \rho_{\beta\beta})$ and, in this case, is simply the thermal equilibrium magnetization.

In the presence of the rf pulse, the Hamiltonian for the system is given by Equation [1-23]. As discussed in Section I.4, the time dependence of the Hamiltonian \hat{H} can be removed by transforming the system into a frame rotating at frequency ω about the field H_0 , such that $\gamma H_1 \gg (\omega - \omega_0)$. The equation of motion of the density operator in the rotating frame, then becomes

$$\frac{d\hat{\rho}^*}{dt} = \frac{-i\gamma H_1}{2} [\hat{\rho}^*, \hat{I}_x] , \quad [1-37]$$

with solution,

$$\hat{\rho}^*(\tau) = \exp\left(\frac{i\gamma H_1 \tau \hat{I}_x}{2}\right) \hat{\rho}^*(0) \exp\left(\frac{-i\gamma H_1 \tau \hat{I}_x}{2}\right) . \quad [1-38]$$

$(1/2)\gamma_1 H_1 \tau$ is the angle through which the magnetization is tipped by the pulse and will be denoted by θ (in radians). The representation of the exponential operator can be obtained from its series expansion, from which we have

$$\exp(i\theta \tilde{I}_x) = \begin{bmatrix} \cos \frac{\theta}{2} & i \sin \frac{\theta}{2} \\ i \sin \frac{\theta}{2} & \cos \frac{\theta}{2} \end{bmatrix}. \quad [1-39]$$

For an rf pulse of flip angle 90° , $\theta = \pi/2$, and the representation matrix in Equation [1-39] reduces to

$$\exp(i\frac{\pi}{2} \tilde{I}_x) = \frac{1}{\sqrt{2}} \begin{bmatrix} 1 & i \\ i & 1 \end{bmatrix}. \quad [1-40]$$

For simplicity the density matrix is viewed in the rotating frame in the following discussion. After the transformation indicated in Equation [1-38], the density matrix in the rotating frame is given by

$$\tilde{\rho}^*(\tau) = \frac{1}{2} \begin{bmatrix} 1 & 0 \\ 0 & 1 \end{bmatrix} + \frac{1}{2} \begin{bmatrix} 0 & -i\Delta \\ i\Delta & 0 \end{bmatrix}. \quad [1-41]$$

Evaluating the components of the magnetization per molecule in the rotating frame, we obtain

$$\langle M_x(\tau) \rangle = 0, \langle M_y(\tau) \rangle = \frac{\Delta}{2}, \text{ and } \langle M_z(\tau) \rangle = 0. \quad [1-42]$$

The 90° pulse along the x-axis of the rotating frame has rotated the magnetization from the z-axis to the y-axis of the rotating frame in keeping with simple magnetization vector diagrams.

The spin system is now allowed to precess freely. The effective Hamiltonian is given by Equation [1-21]. The representation of $\exp(i\hat{H}_{\text{eff}} t_1)$ is diagonal in the simple product basis, given by

$$\exp(i\hat{H}_{\text{eff}} t_1) = \begin{bmatrix} \exp\{i(\omega - \omega_0)t_1/2\} & 0 \\ 0 & \exp\{-i(\omega - \omega_0)t_1/2\} \end{bmatrix}, \quad [1-43]$$

where t_1 is the acquisition time variable. The density matrix during the free precession, therefore becomes

$$\tilde{\rho}^*(\tau + t_1) = \frac{1}{2} \begin{bmatrix} 1 & 0 \\ 0 & 1 \end{bmatrix} + \frac{1}{2} \begin{bmatrix} 0 & -i\Delta \exp\{i(\omega - \omega_0)t_1\} \\ i\Delta \exp\{-i(\omega - \omega_0)t_1\} & 0 \end{bmatrix}. \quad [1-44]$$

During the free precession period, the non-zero off-diagonal elements develop time dependence.

The NMR signals in the rotating frame, can now be computed using the expressions for expectation values of magnetization components to give

$$\begin{aligned}\langle M_x(t_1+\tau) \rangle &= -(\Delta/2) \sin\{(\omega-\omega_0)t_1\} , \\ \langle M_y(t_1+\tau) \rangle &= -(\Delta/2) \cos\{(\omega-\omega_0)t_1\} , \\ \langle M_z(t_1+\tau) \rangle &= 0.\end{aligned}\tag{1-45}$$

These calculations suggest that the magnetization lies in the transverse plane (xy plane) throughout the detection period t_1 . If the relaxation effects were included, we would have obtained

$$\begin{aligned}\langle M_x(t_1+\tau) \rangle &= -(\Delta/2) \sin\{(\omega-\omega_0)t_1\} \exp\{-t_1/T_2\} , \\ \langle M_y(t_1+\tau) \rangle &= -(\Delta/2) \cos\{(\omega-\omega_0)t_1\} \exp\{-t_1/T_2\} .\end{aligned}\tag{1-46}$$

Spin-spin relaxation damps the oscillatory functions, with the characteristic rate constant $(1/T_2)$. Equation [1-46] gives the time domain magnetization functions for this simple experiment. The conventional mode of presentation of the NMR spectrum is in the frequency domain. The frequency domain spectrum can be obtained by Fourier cosine transformation of $\langle M_x(\tau+t_1) \rangle$ or $\langle M_y(\tau+t_1) \rangle$ time

domain functions. Fourier transformation of the time domain functions in Equation [1-46] gives a Lorentzian line centered at frequency $\nu - \nu_0$ (in Hz), with full width at half-height of $1/(\pi T_2)$ (in Hz). It should be noted that $\omega = 2\pi \nu$, in Equations [1-45] and [1-46].

The example of the spin 1/2 system illustrates the way in which the density matrix theory is used to describe pulsed FT experiments. An analysis using the classical Bloch equations would have yielded identical results in this case. For larger systems with strong coupling or for sequences which involve the generation of multiple quantum coherences, the Bloch equation approach is inadequate. Even with larger spin systems, the basic guidelines in the application of density matrix theory remain the same, however the computational complexity can increase rapidly.

I.9 Summary

In this chapter a brief description of density matrix theory and its applications in the description of pulsed FT NMR experiments was presented. The equation of motion of the density matrix was set up and the application of the rotating frame transformation in the simplification of the equation of motion described. Modifications of the density matrix theory to take into account the relaxation

and chemical exchange processes, were briefly discussed. Finally, the application of the density matrix theory in the description of pulsed FT experiments was illustrated by considering a simple example of an ensemble of spin $1/2$ systems subjected to the most basic FT experiment, the 90° pulse-acquire sequence. The next chapter describes the implementation of a computer program to carry out density matrix computations on more general spin systems under a variety of multiple pulse and two dimensional FT experiments.

CHAPTER II

DESCRIPTION OF THE SIMULATION PROGRAM

II.1 Introduction

The implementation of a simulation program to analyze multiple pulse and two dimensional FT NMR experiments, based on density matrix theory, is discussed in this chapter. The objectives of the program are laid out, the structure of the program is illustrated with a block diagram and brief descriptions of the major subprograms are given. The data structure for the representation of the density matrix is described. The computation of the thermal equilibrium density matrix is illustrated with examples of the IS and IS₂ spin systems. The implementation of the density matrix transformation by a rf pulse and during free precession periods is discussed, with the transformations illustrated for the IS and IS₂ systems.

The effects of broadband decoupling are considered briefly. The equation of motion for the density matrix in the presence of a broadband decoupler irradiation, and its

solution are given. The simulation of the signal acquisition process is considered next. The algorithms used to compute and simplify the signal expressions are briefly described. The interpretation of the frequency terms in the computed signal is clarified by carrying out the analysis of a simple pulse sequence.

The implementation of various other features in the program, such as phase cycling of the rf pulses and the receiver, rf pulses of any given tip angle, are described. Finally, some of the limitations of the current version of the program are discussed along with suggestions for future extensions.

II.2 Objectives of the Simulation Program

The program has been intended to simulate the effects of multiple pulse sequences on a variety of spin systems. The development of the program has been motivated by the conspicuous absence of a device for analyzing the rapidly increasing number of two-dimensional NMR (2D NMR) and other multiple pulse experiments. The simulation method is based on the density matrix description of pulsed NMR discussed in the last chapter. Some work on the computer simulation of multiple pulse experiments has been reported using Bloch equations (32)

and density matrix theory (33-35). Recently another approach to simulation of multiple pulse and 2D NMR experiments has been devised, making use of the super-spin formalism (36-38). Simple rules for following the evolution of the density operator under rf pulses and during free precession periods have also been given (39-41), but the operator expressions tend to be prohibitively complex in a typical multiple pulse sequence. The computational complexity associated with the density matrix method grows rapidly with the size of the spin system. The need for automated density matrix calculation is therefore apparent, and the aim of this thesis has been to develop a rather general system to accommodate a large variety of pulse sequences and to simulate many of the features used in modern high resolution NMR spectroscopy.

The spin systems that can be analyzed by the program are homonuclear and heteronuclear $I_m S_n$ systems of weakly coupled spin 1/2 nuclei with $1 \leq m, n \leq 3$. The input format is similar to the pulse microprograms used with high resolution NMR spectrometers. The specification of the pulse sequence constitutes: the definition of the spin system; specification of the pulse angles; pulse phases and nuclei on which the pulses act; delay periods and signal acquisition periods with or without broadband decoupling; options to carry out phase cycling of pulses and detectors; and so on.

Pulses can be applied to either I or S nuclei (as in a heteronuclear system), or to both nuclei (as in a homonuclear system), and along the $+x$, $-x$, $+y$, $-y$ axes of the rotating frame. The program is also capable of simulating the effects of pulses of any given flip angle, besides the most common 90° and 180° pulses. Since our early experience showed that examination of the elements of density matrix at different stages in a pulse sequence enabled us to investigate the behaviour of magnetizations and multiple-quantum coherences, a facility to output the density matrix was incorporated into the simulation routine.

The computed signal can be simplified to some extent so as to make the output more comprehensible. Another important simplification feature has been incorporated to allow explicit substitution for the durations of precession periods in terms of $1/(nJ)$, where n is an integer and J is the scalar coupling constant between the I and S nuclei.

II.3 Implementation of the Simulation Program

In order to have a program with reasonable speed, efficiency, and portability, the FORTRAN language was chosen rather than an algebraic language like REDUCE2 (42)

for the implementation of the simulation scheme. The program is organized in a modular fashion, with a short main program and a number of subprograms, each with a distinct function. This feature simplifies the task of expanding the program, since modules to perform new functions can be added on with only relatively minor changes to the short main program. The main program calls on different subprograms to handle various steps specified in the input pulse sequence. Subprograms pass control back as soon as their function is performed and the main program chooses another subprogram depending on the next input specification. Communications between the main program and subprograms are made mostly through common blocks of memory.

The density matrix elements are the most important and complicated items to be represented in the simulation program. The elements of the density matrix are, in general, complex and depend explicitly on the durations of precession and decoupling periods. In order to strike a balance between the complexities of pulse sequences which could be handled and the storage requirements, the number of time variables is limited to four: T_1 , T_2 , D_1 , and D_2 . Each of these variables can be used to define the duration of a period of free precession or a decoupling period, and each variable may be used no more than twice

within a given sequence. Each density matrix element, at any particular point in the pulse sequence, will consist of a sum of terms of the form:

$$\text{TERM} = (A + iB) \exp[2\pi i(\nu_1 T_1 + \nu_2 T_2 + \nu_3 D_1 + \nu_4 D_2)] \quad [2-1]$$

where $A + iB$ is a complex number and $\nu_1, \nu_2, \nu_3, \nu_4$ denote frequencies which describe the evolution during time periods T_1, T_2, D_1, D_2 respectively. The frequencies $\nu_1, \nu_2, \nu_3, \nu_4$ are equal to frequencies for transitions between particular spin states so that the specification of each frequency variable requires the specification of a pair of indices (encoded into a single integer) which identify the states involved in the corresponding transitions. Each term can therefore be represented as a complex number and four encoded integers which specify the frequency variables in each of the time domains. A collection of these terms, each with distinct exponential factors, completely defines a particular element of the density matrix. In order to economize on computer memory requirements, the density matrix is represented as a collection of elements, each consisting of a number of terms, in single dimension arrays with appropriate arrays of index variables to specify the density matrix element to which the particular terms belong. The numbers of

terms associated with each of the density matrix elements are also stored in a single dimension array. This data structure for the representation of the density matrix will be referred to as "data array". For convenience in accessing and manipulating the density matrix, the index of the starting row and the total number of the rows of the "data array" occupied by the density matrix, at a particular stage in the simulation are stored in another array referred to as the "status array". Since the density matrix is Hermitian, only the elements in the upper triangle are stored. The data structure representing the density matrix resides in a common block and is thereby accessible to the subprograms which manipulate and update its elements.

A block diagram of the program is given in Figure 1. The functions of the main program are to read and echo the input pulse sequence, and to control the flow of execution by selecting the appropriate subprogram to handle the particular step in the input. The main program also carries out the task of initializing the values of certain variables, constants and arrays. The subprogram SPNSYS computes the initial thermal equilibrium density matrix appropriate for the spin system specified in the input data, PULSES transforms the density matrix by application of the pulse specified in the input, and the

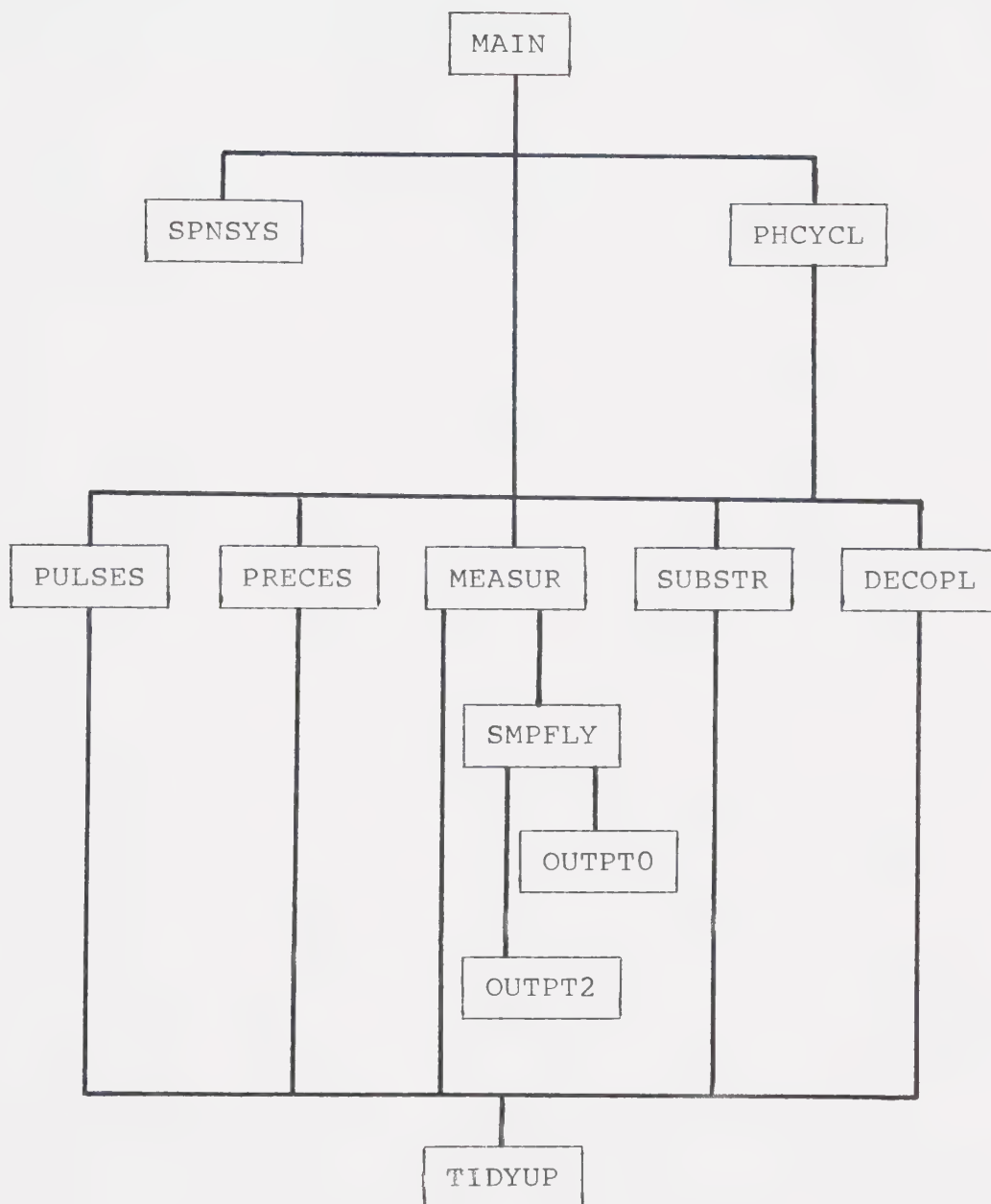


Figure 1. Block diagram of the simulation program.

transformation of the density matrix during the free precession periods is carried out by the subprogram PRECES. The magnetization components are computed by MEASUR and simplified to a certain extent by the subprogram SMPFLY, which recognizes the relationships between $\exp(i\phi) \pm \exp(-i\phi)$ and $\cos \phi$ and $\sin \phi$. The parities of the sine and cosine functions are also invoked in this simplification procedure. After simplification, the final output may have considerably many fewer terms than are present in the internal data structure. The printing of the signal expressions is carried out by the subprogram OUTPT2. The subprogram SUBSTR allows the simplification of the density matrix at intermediate stages by explicit substitution for the duration of one of the time periods T_1 , T_2 , D_1 , or D_2 by $1/(nJ)$, where J is the I-S spin-spin coupling constant and n is an integer. Such substitution often causes certain terms of the density matrix elements to vanish and produces significant simplification. The transformation of the density matrix during broadband decoupling is carried out by DECOPL, which computes the density matrix during the decoupling period using an averaging process discussed in detail in Chapter III. The phase cycling of pulses and the receiver is handled by the subprogram PHYCYCL, which to a certain extent duplicates some of the functions of the main

program by controlling the flow of execution inside the phase cycling loop. As indicated by the block diagram, it interacts with most of the other subprograms. It also keeps track of the signals generated during each of the individual phase cycles and passes on the accumulated signal for simplification. Besides the major subprograms mentioned above, there are a number of other subprograms which carry out various other functions. One of the most important among these is TIDYUP, which organizes the rows of the "data array", and carries out some simplification by collapsing mutually cancellable terms, simplifying terms which can be summed together, and deleting blank rows formed during the simplification procedure.

a. Description of Input Commands

A description of the input commands to the simulation program is given below. Most of the commands consist of two strings (each containing four characters), typed consecutively (without blanks or any other characters between them) on the same line. There must be only one such command in a single line of the input file. Command names which fall short of four characters are to be typed in left justified fashion. The input is read from FORTRAN unit 5.

<u>Command</u>	<u>Description</u>
1. SPINImSn	Sets up the thermal equilibrium density matrix for the $I_m S_n$ spin system with $1 \leq m, n \leq 3$.
2. HOMO	Defines the spin system to be homonuclear. HOMO command should be specified <u>before</u> the SPIN command.
3a. PULS abcc	Applies a pulse transformation to the density matrix. a specifies the pulsed nucleus and can be I or S. b specifies the pulse length and can be any of the following:
b. PULS abccabc'c' ...	<p>A : denotes a 90° pulse</p> <p>B : denotes a 180° pulse</p> <p>C-F: can be used to assign any desired pulse length (see SET command below).</p> <p>cc specifies the direction in the rotating frame along which the pulse is applied and can be any of: +x, -x, -y, and -y.</p> <p>The command (3b) shows how the</p>

PULS command is to be used in a phase cycle sequence. **c'c'** specifies the phase of the pulse in the second pass through the phase cycle (see PHASECYCLE command below).

4. PREC**tt**

Applies the free precession transformation to the density matrix during the time period **tt**, where **tt** can be any of T1, T2, D1 or D2. It is preferable to use T1 or T2 for signal acquisition periods since the program carries out more extensive simplification on terms containing T1 or T2. Each of the time periods can be used no more than twice in a pulse sequence.

5a. MEASaXYb

b. MEASac

c. MEASaXYbaXYb'...

d. MEASacac'...

Simulates the signal acquisition by measuring the magnetization components. Command (5a) measures the complex quadrature magnetization. **a** specifies the

nucleus (I or S). **b** specifies the particular quadrature combination as given below:

b = 0 : $X + iY$

b = 1 : $-Y + iX$

b = 2 : $-X - iY$

b = 3 : $Y - iX$

The output is onto FORTRAN unit

6. Command (5b) measures a single magnetization

component. **a** denotes the nucleus (I or S) and **c** denotes the magnetization component (X, Y or Z). 5c and 5b illustrate how the commands 5a and 5d are to be used inside a phase cycling loop. Here **b'** and **c'** specifies the component to be measured in the second pass through the phase cycle (see PHASECYCLE command below).

6. DCPL**abbbtt**

Applies the transformation appropriate for spin decoupling during a precession period. **a**

specifies the nucleus to be decoupled (I or S), **bbb** denotes 3 blanks, and **tt** specifies the time period during which decoupling is carried out (T1, T2, D1, or D2).

7. SUBS**tt=1/(nnJ)**

Allows the substitution of the specified time variable by a term proportional to the reciprocal of the coupling constant J. **tt** specifies the time variable (T1, T2, D1, or D2) and **nn** is a two digit integer (in I2 format).

8. PHASECYCLE**nn**

Allows phase cycling to be carried out. This command is used to set up a loop, terminated by another such phase cycle command. The loop encloses that part of the pulse sequence in which phase cycling is carried out. **nn** specifies the number of cycles and is such that $1 \leq \mathbf{nn} \leq 64$ (in I2

format). The pulse phases and receiver phases to be used for the different cycles are to be specified sequentially in all PULS and MEAS commands. If the number of cycles in the loop is larger than 16, then specifications for 16 cycles should appear on each line, the next 16 on the next line leaving the first four characters blank, and so on. The last command inside the phase cycle loop must be a MEAS and there can only be one MEAS command in the loop. There can only be one phase cycle loop in the pulse sequence.

9a. SETP**bbb**angle

Defines any desired pulse angle for the pulses C-F. **P** specifies one of the pulses (C, D, E, or F) and **angle** represents the flip angle (in degrees) to be assigned to **P**. The angle is to

be specified in F5.1 format.

bbb denotes 3 blank characters.

b. SET**spec****aa**

Allows the user to set states

(ON/OFF) of certain

specification switches. **aa** is

the switch setting and is either

ON or OFF. **spec** is one of the

following:

(a) MOVE: If it is desired to store the density matrices after each step, for print out or debugging purposes, the OFF setting can be used to prevent overwriting of previous density matrices within the data table. The default setting is ON.

(b) DEBUG: Intermediate output for debugging purposes can be produced with the ON setting. The default setting is OFF.

10. WRDM

Can be used to print out the density matrix after the

previous command in the pulse sequence. The output is onto FORTRAN unit 6.

11. DUMP

Can be used to print out the internal representation (data structure) of the density matrix after the previous command in the pulse sequence. The output is onto the FORTRAN unit 6.

12. COMM**string**

Echo prints **string** as a comment onto FORTRAN unit 6.

13. STOP

Stop calculation and terminate execution.

14. NEXT

Terminates the calculation on the current pulse sequence and starts calculation on the pulse sequence specified, starting from the next line of input.

15. STDm

Stores the internal representation of the density matrix onto FORTRAN unit 7. It can be read in later in another run to continue the calculation.

16. RDFL

Reads in an initial density matrix from FORTRAN unit 4. This feature can be used to carry out calculations starting with non equilibrium density matrices. The FORTRAN unit 4 should contain the SPIN command (HOMO and SET commands if applicable), the NEDM and CLFL commands as well as the density matrix elements.

NEDM (subcommand)

This subcommand follows the SPIN command mentioned above, and initiates reading in the density matrix. The density matrix element is represented as described in Section II.3. Only the non zero and upper triangular and diagonal elements should be specified. There should be one line for each "TERM" (Equation [2-1]) of every density matrix element. Density matrix elements are to be defined one after the other.

Each line should contain the data described in Table 1.

After all matrix elements have been specified, the input mode is terminated by inserting a zero in the field corresponding to NCOMP (Table 1).

CLFL (subcommand)	Instructs the program to terminate input from FORTRAN unit 4 and to continue to read input from the normal input device (FORTRAN unit 5).
-------------------	---

II.4 Choice of Basis Sets

The basis set for representation of $\hat{\rho}$ is the eigenbasis of \hat{H}_0 which, in the weak coupling limit, is taken to be the direct product of the irreducible basis of the I_m subgroup and the irreducible basis of the S_n subgroup. The construction of the irreducible basis in the simulation program uses a building up process which starts with the eigenfunctions of the single spin 1/2 system, forms uncoupled simple product basis, then transforms the simple product functions into the irreducible basis functions using appropriate

Table 1

Program Input Format for Density Matrix Elements

<u>Variable</u>	<u>Format</u>	<u>Description</u>
NCOMP	I6	Specifies the number of "TERMS" in the particular density matrix element
LDM	I6	The row and column numbers of the matrix element in the form: (i × 100) + j, where i is the row number and j is the column number
COEFF	2E14.7	A complex number specifying the magnitude of the density matrix element
TAG1	I6	The T1 time dependence encoded as (i × 100) + j, representing the $\exp\{2\pi i v_{ij} T1\}$ factor in Eq. II.1
TAG2	I6	Corresponding variable for T2
TAG3	I6	Corresponding variable for D1
TAG4	I6	Corresponding variable for D2
JCOEFF	I6	Encodes information regarding the spin coupling constant J during various precession periods. Should be specified as "111111"

transformation matrices. The eigenbasis of \hat{H}_0 is the set of eigenfunctions $|I, M_I\rangle |S, M_S\rangle$ of the operators \hat{I}^2 , \hat{I}_z , \hat{S}^2 , and \hat{S}_z with eigenvalues $I(I+1)$, M_I , $S(S+1)$ and M_S respectively. Here \hat{I} is the total spin angular momentum operator for the I_m spins and \hat{S} is the total spin angular momentum operator for the S_n spins. Since the basis functions are never explicitly generated by the program, but the representations of spin angular momentum operators are, the building up process will be illustrated in connection with the representation of the spin operators.

II.5 Construction of Spin Operator Representation Matrices

The generation of representation matrices for spin angular momentum operators is accomplished by starting with the matrix representation of the required operator for a single spin 1/2 nucleus, forming the representation of this operator in an uncoupled product basis and transforming this product representation into the representation in the irreducible basis by appropriate transformation matrices. This process is illustrated by considering the representation of \hat{I}_z and \hat{S}_z in I_1S_1 and I_1S_2 spin systems.

The matrix representation \tilde{z} of the z-component of the spin angular momentum operator for a single spin 1/2 system, in the $\{|1/2, 1/2\rangle, |1/2, -1/2\rangle\}$ basis, is (1)

$$\underset{\sim}{z} = (1/2) \begin{bmatrix} 1 & 0 \\ 0 & -1 \end{bmatrix}. \quad [2-2]$$

The representation of \hat{I}_z for the $I_1 S_1$ spin system is constructed by computing the direct product of $\underset{\sim}{z}$ with a 2×2 unit matrix $\underset{\sim}{U}_2$ corresponding to the S spin, giving

$$\underset{\sim}{I}_z = \underset{\sim}{z} \otimes \underset{\sim}{U}_2 = (1/2) \begin{bmatrix} 1 & 0 & 0 & 0 \\ 0 & -1 & 0 & 0 \\ 0 & 0 & 1 & 0 \\ 0 & 0 & 0 & -1 \end{bmatrix}. \quad [2-3]$$

The basis functions $|I, M_I\rangle |S, M_S\rangle$ are in the order $(M_I, M_S) = (1/2, 1/2), (-1/2, 1/2), (1/2, -1/2), (-1/2, -1/2)$. The representation of $\underset{\sim}{S}_z$ is constructed by reversing the order of direct products in Equation [2-3] and is given by

$$\underset{\sim}{S}_z = \underset{\sim}{U}_2 \otimes \underset{\sim}{z}. \quad [2-4]$$

A more interesting case, involves the representation of $\underset{\sim}{S}_z$ for the $I_1 S_2$ system. The representation $\underset{\sim}{z}_2$, of the z -component of the spin angular momentum for the S_2 spin subgroup in the uncoupled basis is generated by

$$\underset{\sim}{z}_2 = \underset{\sim}{z} \otimes \underset{\sim}{U}_2 + \underset{\sim}{U}_2 \otimes \underset{\sim}{z}, \quad [2-5]$$

Here the basis functions $|I, M_I\rangle |S, M_S\rangle$ are arranged in the order $(M_I, M_S) = (1/2, 1), (-1/2, 1), (1/2, 0), (-1/2, 0), (1/2, -1), (-1/2, -1), (1/2, 0), (-1/2, 0)$ with the first 6 functions associated with the triplet states of the S_2 subsystem, and the last 2 with the singlet state.

Similarly the representation of \hat{I}_z for the $I_1 S_2$ spin system can be constructed by taking the direct product of \tilde{z} with \tilde{U}_4 , a 4×4 unit matrix corresponding to S_2 subgroup:

$$\tilde{I}_z = \tilde{z} \otimes \tilde{U}_4 . \quad [2-8]$$

The matrix representations of other operators $\hat{I}_x, \hat{I}_y, \hat{S}_x$ and \hat{S}_y are likewise constructed, building up from their corresponding representations for the single spin $1/2$ system. The matrices \tilde{D} for the transformation of spin operators from uncoupled to coupled basis for 2 and 3 spin $1/2$ subsystems are stored in the program.

II.6 Computation of the Thermal Equilibrium Density Matrix

The first step in the simulation of any pulse sequence is the specification of the spin system $I_m S_n$ and the construction of the thermal equilibrium density matrix.

In the high temperature limit, the thermal equilibrium density operator given in Equation [1-33] reduces to

$$\hat{\rho}(0) = (\hat{1} - \hat{H}_0/kT)/N , \quad [2-9]$$

where $\hat{1}$ is the identity operator and N is the number of spin states (2^{n+m} for the $I_m S_n$ spin system). In the case of weak coupling between the I_m and S_n spin groups, the eigenbasis of \hat{H}_0 , constructed in Section II.3, is the set of eigenfunctions $\{|I, M_I\rangle |S, M_S\rangle\}$ of the operators \hat{I}^2 , \hat{I}_z , \hat{S}^2 and \hat{S}_z with eigenvalues $I(I+1)$, M_I , $S(S+1)$, and M_S respectively. Hence $\hat{\rho}(0)$ is diagonal in this basis and has elements

$$\rho_{jj}(0) = [1 - (\gamma_I h \nu_I M_{Ij} + \gamma_S h \nu_S M_{Sj})/kT]/N , \quad [2-10]$$

where the contributions from the much smaller spin-spin interaction terms have been neglected, and M_{Ij} and M_{Sj} are the eigenvalues of \hat{I}_z and \hat{S}_z for the j -th basis function. Since the term $\hat{1}/N$ is common to all of the elements of $\hat{\rho}(0)$, it is unaffected by rf pulses and decoupling fields, and it gives no contributions to measurable properties of the system, it can therefore be ignored. We take

$$\rho_{jj}(0) \cong -\Delta_I M_{Ij} - \Delta_S M_{Sj} , \quad [2-11]$$

where $\Delta_I = (\gamma_I h \nu_I / NkT)$ and $\Delta_S = (\gamma_S h \nu_S / NkT)$ are constants. Using the above considerations, it can be shown that the thermal equilibrium density matrix for the $I_1 S_1$ system can be written as

$$\tilde{\rho}(0) = (1/2) \begin{bmatrix} \Delta_I + \Delta_S & 0 & 0 & 0 \\ 0 & -\Delta_I + \Delta_S & 0 & 0 \\ 0 & 0 & \Delta_I - \Delta_S & 0 \\ 0 & 0 & 0 & -\Delta_I - \Delta_S \end{bmatrix} . \quad [2-12]$$

In the simulation program, $\Delta_I = \Delta_S = 100$ for homonuclear spin systems and, for heteronuclear spin systems, $\Delta_I = 5$ and $\Delta_S = 100$.

II.7 Transformation of the Density Matrix by rf Pulse Operators

During the presence of an rf pulse, the Hamiltonian operator is time dependent. This explicit time dependence of the Hamiltonian operator in the laboratory frame, is removed by a transformation into a coordinate system rotating at an appropriate frequency as shown in Section I.3, and the solution to the equation of motion is given

by Equation [1-18]. An analysis of the effects on an I_1S_1 spin system, on the application of a rf pulse of definite duration to the S nucleus, is illustrated below.

The Hamiltonian for the I_mS_n spin system, in a frame rotating at frequency ν about the z-axis, is

$$\begin{aligned} \hat{H}/h = & -(\nu_I - \nu)\hat{I}_Z - (\nu_S - \nu)\hat{S}_Z + J\hat{I}_Z\hat{S}_Z - \\ & (\gamma_I H_1/2\pi)\hat{I}_X - (\gamma_S H_1/2\pi)\hat{S}_X . \end{aligned} \quad [2-13]$$

The last two terms arise from the rf field which has frequency ν and strength $2H_1$. The spin-spin coupling term can be ignored since its magnitude is very small compared to the Zeeman interaction terms. When $|\nu_S - \nu|$ is small compared to $\gamma_S H_1/2\pi$, the rf field is on-resonance with the S spins, and is far from resonance for the I spins so that the frequency offset term for the S spins and the $(\gamma_I H_1/2\pi)\hat{I}_X$ term can be ignored. The effective Hamiltonian then reduces to

$$\frac{\hat{H}_{\text{eff}}}{h} = -(\nu_I - \nu)\hat{I}_Z - (\gamma_S H_1/2\pi)\hat{S}_X . \quad [2-14]$$

Since the first term in Equation [2-14] describes the free precession of any I spin transverse magnetization, which is not really of interest here and it can be treated

separately, we will ignore this term during the application of the rf pulse. The density matrix after the application of the pulse is therefore related to the initial density matrix by Equation [1-18]. Hence the transformation operator, $\hat{R}_k(\theta)$, which describes the rf pulse is

$$\hat{R}_k(\theta) = \exp(i\gamma_S H_1 t \hat{S}_k) = \exp(i\theta \hat{S}_k) , \quad [2-15]$$

where θ is the angle through which S magnetization is flipped by the pulse. In order to carry out the transformation in Equation [1-18] the matrix representation of the transformation operator $\exp(i\theta \hat{S}_k)$ in the $I_1 S_1$ basis set must be computed.

The transformation matrix is constructed by a building up process which is exactly analogous to the process described in Section II.5 for the construction of the spin operator representations. The transformation operator $\hat{R}_k(\theta)$ for a pulse along the k-axis of the rotating frame, for single spin 1/2 nucleus, is (1,43)

$$\hat{R}_k(\theta) = \exp(i\theta \hat{S}_k) = \hat{1} \cos(\theta/2) + 2i \hat{S}_k \sin(\theta/2). \quad [2-16]$$

The direction index k can take on values $\pm x$ and $\pm y$ corresponding to the four phases commonly available on

spectrometers. In general, the transformation matrix for the particular I_m or S_n subgroup is obtained by taking direct products of the single spin representations (Equation [2-16]) to produce a representation in the uncoupled simple product basis, then transforming this simple product representation to the irreducible basis using an appropriate transformation matrix. The matrix representation of the pulse for the full $I_m S_n$ system is obtained by taking the direct product of the transformation matrix for the I_m subgroup with a $2^n \times 2^n$ unit matrix (pulse on I nuclei only), the direct product of a $2^m \times 2^m$ unit matrix with the transformation matrix for the S_n subgroup (pulse on S nuclei only), or the direct product of the transformation matrix for the I_m subgroup with the transformation matrix for the S_n subgroup (pulses to both I and S nuclei in a homonuclear system).

The case of an $I_1 S_1$ system shall be considered. The pulse matrix $\tilde{R}_x(\theta)$ for a rf pulse applied along the x-axis of the rotating frame for a single spin 1/2 nucleus, in the $\{|1/2, 1/2\rangle, |1/2, -1/2\rangle\}$ basis, is

$$\tilde{R}_x(\theta) = \begin{bmatrix} C & iS \\ iS & C \end{bmatrix}, \quad [2-17]$$

where $C = \cos(\theta/2)$ and $S = \sin(\theta/2)$. By analogy with Equation [2-4], the direct product of \tilde{U}_2 with $\tilde{R}_X(\theta)$ yields the pulse transformation matrix $\tilde{R}_{SX}(\theta)$ for the full I_1S_1 system:

$$\tilde{R}_{SX}(\theta) = \tilde{U}_2 \otimes \tilde{R}_X(\theta) = \begin{bmatrix} C & 0 & iS & 0 \\ 0 & C & 0 & iS \\ iS & 0 & C & 0 \\ 0 & iS & 0 & C \end{bmatrix} . \quad [2-18]$$

For the rf pulse applied to the I spins, the corresponding transformation matrix $\tilde{R}_{IX}(\theta)$ is constructed by reversing the order of direct products:

$$\tilde{R}_{IX}(\theta) = \tilde{R}_X(\theta) \otimes \tilde{U}_2 . \quad [2-19]$$

If the rf pulse affects both nuclei (a homonuclear spin system), the corresponding transformation matrix is

$$\tilde{R}_{ISX}(\theta) = \tilde{R}_X(\theta) \otimes \tilde{R}_X(\theta) = \begin{bmatrix} C^2 & iCS & iCS & -S^2 \\ iCS & C^2 & -S^2 & iCS \\ iCS & -S^2 & C^2 & iCS \\ -S^2 & iCS & iCS & C^2 \end{bmatrix} \quad [2-20]$$

since both spins experience the effects of the pulse.

Pulse representation matrices for larger spin systems are also built up in a similar stepwise manner in exact analogy to the construction of spin operators described in Section II.6.

The subprogram PULSES, which handles the rf pulse transformations, analyzes the input command to identify the nuclei to which the rf pulse is to be applied, the duration of the rf pulse, and the direction in the rotating frame along which the rf pulse is to be applied (referred to as the phase of the rf pulse). The appropriate pulse transformation matrix is computed and the transformation indicated in Equation [1-18] is carried out, by retrieving the elements of the previous density matrix, one by one and carrying out the matrix multiplications of Equation [1-18]. After each element of the final density matrix has been computed, a preliminary simplification and organization of the terms of the density matrix element are carried out. At the end of the transformation procedure, bookkeeping information concerning the final density matrix, such as the start index and size in the "data array", is updated in the "status array".

II.8 Transformation of the Density Matrix During Free Precession Periods

During a free precession period, the spin Hamiltonian is time independent, and the density matrix in the rotating frame evolves according to Equation [1-11]. The spin Hamiltonian during a free precession period is given as

$$\frac{\hat{H}}{h} = -\nu_I \hat{I}_Z - \nu_S \hat{S}_Z + J \hat{I}_Z \hat{S}_Z . \quad [2-21]$$

Computation of the matrix representation of the exponential operator $\exp\{-i\hat{H}(t_2-t_1)/h\}$ is relatively straightforward, since the $\{|I, M_I\rangle |S, M_S\rangle\}$ basis set is an eigenbasis of \hat{H} . The representation matrix is diagonal, and has elements

$$\langle j | \exp[-i\hat{H}(t_2-t_1)/h] | j \rangle = \exp[-2\pi i E_j(t_2-t_1)] , \quad [2-22]$$

where E_j is the energy (in Hz) of the j th state. It can be shown that the effect of the transformation in Equation [1-11], is to change the density matrix elements as

$$\rho_{pq}(t_2) = \rho_{pq}(t_1) \exp[2\pi i \nu_{pq}(t_2-t_1)] , \quad [2-23]$$

where $\nu_{pq} = E_q - E_p$, is the frequency of the transition between the states p and q .

As pointed out in Section II.3, the time-dependence of the elements of the density matrix is represented by an encoded pair of indices which specify the states whose energy separation corresponds to the frequency of oscillation during a particular time interval. During a free precession period of duration T_1 (where $T_1 = t_2 - t_1$), for example, the terms in ρ_{pq} will all be multiplied by $\exp(2\pi i \nu_{pq} T_1)$ so that the encoded integer array associated with the T_1 time domain must be updated by incorporating the encoded integer pair p, q into each term in ρ_{pq} .

II.9 Transformation of Density Matrix During Broad-Band Decoupling

It will be shown in Chapter III that the behaviour of the density matrix, when a noise decoupling field is applied at the resonance frequency for the S nuclei, is described by

$$\rho_{pq}(t_2) = \exp[2\pi i \nu'_{pq}(t_2 - t_1)] \sum_{p'} \sum_{q'} \rho_{p'q'}(t_1) P_{p'q';pq} ,$$

[2-24]

where the $P_{p'q';pq}$ are numerical coefficients given in Section III.3 and ν_{pq}' is the "decoupled frequency" corresponding to ν_{pq} (i.e. the frequency of the transition from state p to state q in the absence of scalar spin-spin coupling between the nuclei I and S).

In the implementation of the decoupling subprogram, DECOPL, the coefficients $P_{p'q';pq}$ are grouped into a number of small matrices and stored in the subprogram. The manipulations of the density matrix data structure for a decoupling period are straightforward - one computes the appropriate linear combinations, then updates the encoded integer array associated with the decoupling time variable in the same way as for a free precession period. In addition, a flag is set to indicate to the output stages of the program that the spin-spin coupling constant J is to be set to zero in this time period, so that decoupled frequencies will be computed at that stage.

II.10 Computation and Simplification of Signal Expressions

The signal measured by the receiver in NMR experiments is proportional to the transverse components of the magnetization for a particular type of nuclei. The expression for the physical observable Q , is given by the Equation [1-6]. In NMR experiments, the physical

observables \hat{Q} are either the individual transverse components, for example in the case of I spins $\langle \hat{I}_x \rangle$ or $\langle \hat{I}_y \rangle$, or, in quadrature detection mode, the complex components formed from these transverse components. The various complex magnetizations that can be formed from these transverse components are $\langle \hat{I}_x + i\hat{I}_y \rangle$, $\langle \hat{I}_y + i\hat{I}_{-x} \rangle$, $\langle \hat{I}_{-x} + i\hat{I}_{-y} \rangle$ and $\langle \hat{I}_{-y} + i\hat{I}_x \rangle$.

The simulation of the receiver in NMR experiments is accomplished by constructing a matrix representation of the appropriate spin angular momentum operator \hat{I}_x , \hat{I}_y , $\hat{I}_x + i\hat{I}_y$, $\hat{I}_y + i\hat{I}_{-x}$, $\hat{I}_{-x} + i\hat{I}_{-y}$, $\hat{I}_{-y} + i\hat{I}_x$ (spin I magnetizations only), \hat{S}_x , \hat{S}_y , $\hat{S}_x + i\hat{S}_y$, $\hat{S}_y + i\hat{S}_{-x}$, $\hat{S}_{-x} + i\hat{S}_{-y}$, $\hat{S}_{-y} + i\hat{S}_x$ (spin S magnetizations only), or $\hat{I}_x + \hat{S}_x$, $\hat{I}_y + \hat{S}_y$, $(\hat{I}_x + \hat{S}_x) + i(\hat{I}_y + \hat{S}_y)$, $(\hat{I}_y + \hat{S}_y) + i(\hat{I}_{-x} + \hat{S}_{-x})$, $(\hat{I}_{-x} + \hat{S}_{-x}) + i(\hat{I}_{-y} + \hat{S}_{-y})$, $(\hat{I}_{-y} + \hat{S}_{-y}) + i(\hat{I}_x + \hat{S}_x)$ (both I and S magnetizations for homonuclear systems). The construction of the matrix representation of a spin angular momentum operator is discussed in Section II.5. In homonuclear systems, the sum of the representations for the spin operators for the I and S spins is constructed. The calculation of the magnetization is effected using Equation [1-6], with \hat{Q} replaced by the appropriate spin angular momentum as listed above. For completeness, the simulation program allows one to "measure" the z-component of the magnetizations although these cannot be measured directly with a spectrometer.

The subprogram MEASUR, which carries out the signal computation, first analyses the input command to determine the magnetization component which is to be extracted for the specified spins. It then constructs the matrix representations of the appropriate spin angular momentum operators. In the computation of the magnetization components, since only the trace of the product of ρ and the appropriate spin operator matrix is needed, the diagonal elements of the product matrix are computed and summed together. Simplification of these terms is carried out by recognizing the relationships between $\exp(i\phi) \pm \exp(-i\phi)$ and $\cos \phi$ and $\sin \phi$, where ϕ refers to the encoded integer arrays associated with the time variables T1, T2, D1 and D2. The subprogram SMPFLY scans through the rows of terms in the "data array" associated with each element of the density matrix and picks out pairs of rows which can be simplified and can be expressed in terms of sine or cosine functions. The information regarding the type of the function (i.e. "sine", "cosine" or "exp") is encoded in appropriate integer arrays for communication to the printing subprograms. Furthermore, the four integer arrays associated with the four time variables are decoded in the output stage and the frequencies ν_{pq} associated with each time domain are given as explicit linear combinations of ν_I , ν_S and J so that the time dependence

can be ascribed clearly to the chemical shift offsets and/or spin-spin coupling. This explicit dependence on ν_I , ν_S and J is also given when the density matrix is itself output. It should be pointed out that ν_I and ν_S in the output represent offsets from the corresponding transmitter frequencies. The justification for this interpretation of frequency terms is discussed in the next section.

II.11 Identification of ν_I and ν_S as Frequency Offsets from Transmitter

It was indicated above that the frequencies ν_I and ν_S in the output represent offsets from the corresponding transmitter frequencies. In this section, a detailed analysis of a simple example will be presented to illustrate that despite the numerous transformations between various frames of reference required in the density matrix treatment, the signal output by the simulation program is justified if the frequency terms in the output are considered as offsets from corresponding transmitter frequencies.

It is important to recognize that the density matrix and the Hamiltonian matrix which appear in Equation [1-17] must be in the same frame of reference. The

straightforward procedure for relating the density matrix in the laboratory frame before and after a pulse requires the transformations

$$\hat{\rho}^{(\text{lab})}(t_1) \rightarrow \hat{\rho}^{*(\text{rot})}(t_1) \xrightarrow{\text{Pulse Transformation}} \hat{\rho}^{*(\text{rot})}(t_1 + \tau) \rightarrow \hat{\rho}^{(\text{lab})}(t_1 + \tau) \quad [2-25]$$

As an illustration, the evolution of density matrix will be followed in detail, by carrying out the sequence of transformations in Equation [2-25] for each pulse in the sequence shown in Figure 2 applied to the I_1S_1 spin system. This pulse sequence is employed for the determination of pulse lengths on nuclei, when they are not under direct observation (44,45).

The elements of the density matrix in laboratory and rotating frames at time t are related by

$$\rho_{pq}^{(\text{rot})}(t) = \rho_{pq}^{(\text{lab})}(t) \exp[-2\pi i(M_p - M_q)\nu t] , \quad [2-26]$$

where M_p and M_q are the eigenvalues of the z -component of the total angular momentum operator $\hat{I}_z + \hat{S}_z$ in the p and q states. At $t = 0$, the laboratory and rotating frames coincide and the initial density matrix is

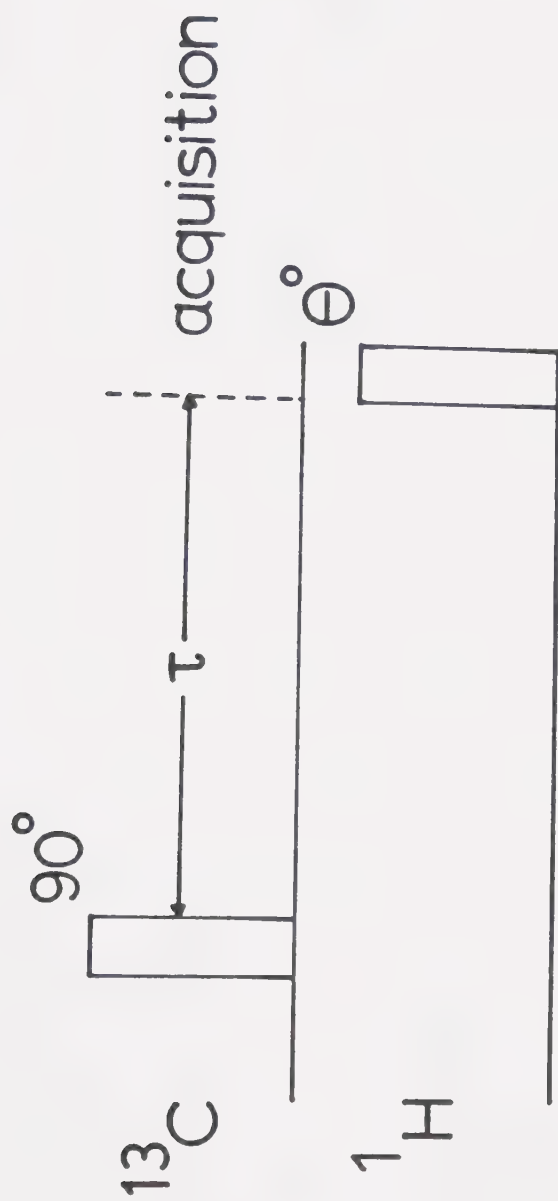


Figure 2. Pulse sequence for calibration of pulse width. The delay τ is to be set for $1/(2J_{\text{CH}})$. When $\theta = 90^\circ$ for the proton pulse, the carbon signals will have minimum intensity.

$$\rho_{\sim}^{(lab)}(0) = \rho_{\sim}^{(rot)}(0) = \begin{bmatrix} \Delta + \delta & 0 & 0 & 0 \\ 0 & \Delta - \delta & 0 & 0 \\ 0 & 0 & -\Delta + \delta & 0 \\ 0 & 0 & 0 & -\Delta - \delta \end{bmatrix} \quad [2-27]$$

where Δ and δ are the parameters defined above. A 90° pulse is applied, at time zero at the I resonance frequency ν_I° and the density matrix in the frame rotating at $\nu = \nu_I^\circ$, after the pulse is

$$\rho_{\sim}^{(rot)}(\tau_p) = \begin{bmatrix} \Delta & i\delta & 0 & 0 \\ -i\delta & \Delta & 0 & 0 \\ 0 & 0 & -\Delta & i\delta \\ 0 & 0 & -i\delta & -\Delta \end{bmatrix}, \quad [2-28]$$

where τ_p is the time required to effect the 90° pulse. Transforming to the laboratory frame, we obtain

$$\rho_{\sim}^{(lab)}(\tau_p) = \begin{bmatrix} \Delta & a & 0 & 0 \\ a^* & \Delta & 0 & 0 \\ 0 & 0 & -\Delta & a \\ 0 & 0 & a^* & -\Delta \end{bmatrix}, \quad [2-29]$$

where $a = i\delta \exp[2\pi i \nu_I^\circ \tau_p]$ and the asterisk denotes complex conjugation. According to Figure 2, the system is

allowed to precess freely for a period t_1 during which the density matrix evolves under the time independent Hamiltonian and becomes

$$\rho_{\sim}^{(lab)}(\tau_p + t_1) = \begin{bmatrix} \Delta & b & 0 & 0 \\ b^* & \Delta & 0 & 0 \\ 0 & 0 & -\Delta & c \\ 0 & 0 & c^* & -\Delta \end{bmatrix}, \quad [2-30]$$

where $b = i\delta \exp[2\pi i(\nu_I^\circ \tau_p + \nu_{12} t_1)]$,
 $c = i\delta \exp[2\pi i(\nu_I^\circ \tau_p + \nu_{34} t_1)]$, and ν_{ij} is the frequency of the transition between states i and j . At the end of the precession period, a 90° pulse is applied at the S resonance frequency. To handle this, the density matrix must be transformed into the frame rotating at the frequency ν_S° of the S transmitter to facilitate the transformation by the S pulse. The density matrix in the S rotating frame before the pulse is given by

$$\rho_{\sim}^{(rot)}(\tau_p + t_1) = \begin{bmatrix} \Delta & d & 0 & 0 \\ d^* & \Delta & 0 & 0 \\ 0 & 0 & -\Delta & e \\ 0 & 0 & e^* & -\Delta \end{bmatrix}, \quad [2-31]$$

where $d = i\delta \exp\{2\pi i[v_I^0\tau_p + v_{12}t_1 - v_S^0(\tau_p+t_1)]\}$,

$e = i\delta \exp\{2\pi i[v_I^0\tau_p + v_{34}t_1 - v_S^0(\tau_p+t_1)]\}$.

For the sake of simplicity, only the density matrix elements of interest ρ_{12} and ρ_{34} which are associated with transverse I magnetization will be considered further.

After the application of the 90°_x S pulse, the elements ρ_{12} and ρ_{34} in the S rotating frame are given by

$$\rho_{12}^{(\text{rot})}(\tau_p+t_1+\tau_{p'}) = \rho_{34}^{(\text{rot})}(\tau_p+t_1+\tau_{p'}) =$$

$$i\delta \exp\{2\pi i(v_I^0\tau_p + v_S^0(\tau_p+t_1))\} \{ \exp(2\pi i v_{12}t_1) + \exp(2\pi i v_{34}t_1) \}.$$

[2-32]

Transformation of these density matrix elements into the laboratory frame yields

$$\rho_{12}^{(\text{lab})}(\tau_p+t_1+\tau_{p'}) = \rho_{34}^{(\text{lab})}(\tau_p+t_1+\tau_{p'}) =$$

$$i\delta \exp\{2\pi i(v_I^0\tau_p + v_S^0\tau_{p'})\} \{ \exp(2\pi i v_{12}t_1) + \exp(2\pi i v_{34}t_1) \},$$

[2-33]

where $\tau_{p'}$ denotes the duration of the 90°_x S pulse. During the signal acquisition period t_2 , the density matrix elements develop further time dependence as

$$\rho_{12}^{(\text{lab})}(\tau_p + t_1 + \tau_{p'} + t_2) = i\delta \exp\{2\pi i(\nu_I^0 \tau_p + \nu_S^0 \tau_{p'})\} \times$$

$$\{\exp(2\pi i \nu_{12} t_1) + \exp(2\pi i \nu_{34} t_1)\} \exp(2\pi i \nu_{12} t_2) ,$$

[2-34]

$$\rho_{34}^{(\text{lab})}(\tau_p + t_1 + \tau_{p'} + t_2) = i\delta \exp\{2\pi i(\nu_I^0 \tau_p + \nu_S^0 \tau_{p'})\} \times$$

$$\{\exp(2\pi i \nu_{12} t_1) + \exp(2\pi i \nu_{34} t_1)\} \exp(2\pi i \nu_{34} t_2) .$$

Since the heterodyne receiver in an NMR spectrometer measures the I magnetization in the rotating frame, ρ_{12} and ρ_{34} in the I rotating frame are required:

$$\rho_{12}^{(\text{rot})}(\tau_p + t_1 + \tau_{p'} + t_2) = i\delta \exp\{2\pi i(\nu_S \tau_{p'} - \nu_I \tau_p)\} \times$$

$$\{\exp(2\pi i \Delta \nu_{12} t_1) + \exp(2\pi i \Delta \nu_{34} t_1)\} \times \exp(2\pi i \Delta \nu_{12} t_2) ,$$

[2-35]

$$\rho_{34}^{(\text{rot})}(\tau_p + t_1 + \tau_{p'} + t_2) = i\delta \exp\{2\pi i(\nu_S \tau_{p'} - \nu_I \tau_p)\} \times$$

$$\{\exp(2\pi i \Delta v_{12} t_1) + \exp(2\pi i \Delta v_{34} t_1)\} \times \exp(2\pi i \Delta v_{34} t_2) ,$$

where Δv_{ij} is the frequency offset of the transition frequency v_{ij} from the transmitter frequency v_I° ,

$$\Delta v_{ij} = v_{ij} - v_I^\circ .$$

The I spin signal $I_x + iI_y$ measured is given by

Signal $\propto i\delta\{\exp(2\pi i \Delta v_{12} t_1) + \exp(2\pi i \Delta v_{34} t_1)\} \times$

$$\exp\{2\pi i (v_S^\circ \tau_{p'} - v_I^\circ \tau_{p'})\} \times \quad [2-36]$$

$$\{\exp(2\pi i \Delta v_{12} t_2) + \exp(2\pi i \Delta v_{34} t_2)\} .$$

The factor involving τ_p and $\tau_{p'}$ is just a phase shift and this is compensated in real experiments by "phasing" the spectrum to get pure absorption mode presentation. Since this phase factor is the same for all signals, we can ignore it and write

$$\text{Signal} \propto i\delta\{\exp(2\pi i\Delta\nu_{12}t_1) + \exp(2\pi i\Delta\nu_{34}t_1)\} \times$$

$$[\text{2-37}]$$

$$\{\exp(2\pi i\Delta\nu_{12}t_2) + \exp(2\pi i\Delta\nu_{34}t_2)\} .$$

The signal expression in Equation [2-37] obtained from the above analysis, shows that the transition frequencies in the measured magnetizations appear as offsets from the respective transmitter frequencies. The signal output by the simulation program is exactly similar to Equation [2-37], but the program represents the difference $\nu_I - \nu_I^\circ$ as ν_I (similarly $\nu_S - \nu_S^\circ$ as ν_S). Hence ν_S and ν_I are to be interpreted as offsets from the corresponding transmitter frequencies. The transformations of the density matrix between various frames of reference, described above, are not really necessary since any phase shifts built up in the duration of the pulses are unimportant. These phase shifts do not arise if all pulses are taken to be infinitely short so that laboratory and rotating frames coincide for the duration of a pulse. In this view, all calculations are performed in the laboratory frame, but the frequencies which appear in the signals must be interpreted as offsets from the respective transmitter frequencies.

II.12 Other Features of the Simulation Program

A facility to carry out the phase cycling of pulses and receiver is implemented in the simulation program since phase cycling is a common feature in most modern pulse NMR experiments. Phase cycling is usually employed to suppress unwanted or spurious signals in the spectrum. For efficiency in the simulation program, the density matrix data structure at the point in the pulse sequence where phase cycling begins is retained so that it can be reused in each pass through the cycle. At the end of each pass through the cycle, the measured magnetizations are accumulated with some preliminary simplification.

Another feature of the simulation program allows explicit substitution for the duration of precession periods in terms of $1/(nJ)$, where n is an integer and J is the coupling constant between the I and S nuclei. The substitution feature is especially useful in pulse sequences having multiple refocussing periods, since it usually simplifies the density matrix considerably and keeps the number of terms in the density matrix elements within manageable limits.

The effect of rf pulses of any given intermediate durations can also be simulated by explicitly defining the

tip angles of certain pulses to desired values in the input. There are 6 pulse lengths A, B, C, D, E, and F, with $A = 90^\circ$, $B = 180^\circ$, while C, D, E, and F can be set to any desired value. This feature is useful in studying the effect of imperfect pulses, devising means to reduce the undesirable effects of imperfect pulses, and in analyzing experiments with composite pulses (46) or those experiments such as the DEPT pulse sequence (31), which involve pulses with intermediate flip angles.

II.13 Limitations of and Suggested Extensions to the Simulation Program

The model used for the simulation program excludes spin relaxation and chemical exchange processes. This limitation is reflected in the inability of the program to simulate experiments involving Nuclear Overhauser Enhancement effects or chemical exchange experiments such as 2D chemical exchange and saturation transfer experiments.

Another limitation of the program is in the type of spin systems which can be analyzed. Only $I_m S_n$ systems of spin $1/2$ nuclei can be handled. This domain excludes many interesting spin systems such as $A_m M_n X_k$ systems of spin $1/2$ nuclei and spin systems containing nuclei with spin greater than $1/2$.

An extension of the program, which has been considered and for which preliminary versions have been generated, is the expansion of the set of analyzable spin systems to include a third spin $1/2$ nucleus, so as to make $A_m X_n M_k$ systems within the scope of analysis using the simulation program. Extension to include nuclei with spin greater than $1/2$ has not been investigated, but should not present great difficulty.

Another modification would be the implementation of the feature of variable (user defined) phases of pulses and receiver, so as to provide phase values of $2\pi/k$ where k is an integer. Variable phases could then be described in the input pulse sequence by defining a reference phase and specifying phase increments. This feature would be useful in multiple-quantum experiments which identify particular spin systems by detecting the highest order coherence present in the system, after filtering out the lower order coherences. The shortage of memory space does become a limiting factor when simulating some long pulse sequences especially on large spin systems. It would be useful to introduce a facility to zero out certain density matrix elements which may not be of interest, when the arrays containing the density matrix get nearly full. With this feature it may become possible to simulate certain pulse sequences which are exceptionally long and cannot be handled with the present program.

II.14 Summary

In this chapter, the implementation of a simulation system for multiple pulse and 2DFT NMR experiments, on a digital computer has been described. The objectives of the program and details of the implementation were discussed. Brief descriptions of the basis sets used, the procedures for building up the representations of spin operators and pulse transformation operators were given. The important details of the procedures for computation of the thermal equilibrium density matrix, the transformation of the density matrix during free precession periods and during periods of broad-band spin decoupling, and the simulation of the signal acquisition process were described. The identification of the chemical shift frequency terms in the output as offsets from the corresponding transmitter frequencies were demonstrated in the context of a simple example. Some of the other features of the program which allow phase cycling, substitution for the durations of free precession periods and the facility to handle rf pulses of any user-defined tip angle, were described. Finally, some of the limitations of the current version of the program were exposed along with suggestions for further extensions.

The next chapter gives a detailed analysis of the effect of broad-band decoupling on the density matrix and the method of solution of the equation of motion for the density matrix in the presence of decoupler irradiation. Applications of the simulation program in the analysis of multiple pulse and 2DFT experiments are discussed in Chapter IV.

CHAPTER III

THEORY AND IMPLEMENTATION OF THE HETERONUCLEAR NOISE DECOUPLING SCHEME

III.1 Introduction

The description of the simulation program in Chapter II, mentioned the heteronuclear noise decoupling scheme briefly. This chapter discusses in detail the density matrix description of heteronuclear noise decoupling. Some of the earlier work on the theoretical analysis of the noise decoupling process is due to Ernst (47), who has given the equations of motion of the density matrix in the presence of decoupler irradiation, with implications for CW experiments. In order to improve the broad-band characteristics of the decoupler, several modulation techniques have been introduced (47-50). A multiple pulse decoupling cycle called MLEV, which greatly enhances the broad-band characteristics, has been devised (51). Pegg et al. (52) have presented a simple theory which describes the behaviour of ^{13}C magnetization components when subjected to ^1H decoupling. This theory assumes the

decoupling field to be spatially inhomogeneous and reduces the effect of the decoupler to a randomization of the direction of the proton spin vectors in a plane perpendicular to the axis of the decoupling field. Recently Levitt et al. (53) have demonstrated that unanticipated effects can be observed in certain experiments employing spin decoupling.

In the early parts of this chapter, the equations of motion of the density matrix in the presence of a noise modulated decoupler field are set up and the method of solution is illustrated in detail for the S spin decoupling in the IS_2 system and the final results are given for IS and IS_3 systems. Another type of decoupling, called the spherical randomization decoupling is also considered and the solutions for the density matrix elements are derived. Finally the implementation of the decoupling procedure in the simulation program is described.

III.2 Theoretical Treatment

The time independent Hamiltonian for the $I_m S_n$ system in a frame rotating at the frequency of the decoupler, ν_S , can be written as

$$\hat{H}_0 = -(\nu_I - \nu_S) \hat{I}_z + J_{II} \sum_{\mu > \nu} \hat{I}_\mu \cdot \hat{I}_\nu + J_{SS} \sum_{p > r} \hat{S}_p \cdot \hat{S}_r + J_{IS} \hat{I}_z \hat{S}_z , \quad [3-1]$$

where ν_I is the resonance frequency for the I nuclei, and ν_S , the resonance frequency for the S nuclei is taken to be identical to the decoupler transmitter frequency. J_{II} , J_{SS} and J_{IS} are the spin-spin couplings in Hz, \hat{I}_μ and \hat{S}_p are the dimensionless spin angular momentum operators for the μ th I nucleus and the p th S nucleus respectively, $\hat{I} = \sum_{\mu} \hat{I}_\mu$ and $\hat{S} = \sum_p \hat{S}_p$ are the total spin operators for the I nuclei and S nuclei respectively.

The equation of motion for the spin density operator, $\hat{\rho}$, in the presence of a noise modulated decoupling field applied along the x-axis of the rotating frame of the X nuclei, has been shown by Ernst (47), to follow,

$$\frac{d\hat{\rho}}{dt} = 2\pi i [\hat{\rho}, \hat{H}_0] - K [\hat{S}_x, [\hat{S}_x, \hat{\rho}]] , \quad [3-2]$$

where K is the spectral density of the decoupling field at frequency ν_S , and is proportional to the applied decoupler power. The operators are referred to the coordinate system rotating at frequency ν_S , about the laboratory z axis.

The equation of motion [3-2] can be represented in the basis of eigenfunctions of \hat{H}_0 , as

$$\frac{d\vec{\rho}}{dt} = - \vec{\rho} \tilde{V} , \quad [3-3]$$

where $\vec{\rho}$ is a row supervector containing the elements of the density matrix in an appropriate order, and \tilde{V} is a supermatrix whose real part is proportional to K and with an imaginary part which is diagonal and has elements which involve differences in the eigenvalues of \hat{H}_0 . Details of the solution of the equation of motion are now given for the IS_2 system.

a. IS_2 Spin System

The eigenfunctions of \hat{H}_0 , for the $I_m S_n$ spin system are simple products of the eigenfunctions $|I, M_I\rangle$ of \hat{I}^2 and \hat{I}_z and the eigenfunction $|S, M_S\rangle$ of \hat{S}^2 and \hat{S}_z . For the IS_2 system, the basis functions are:

$$\begin{aligned} |\phi_1\rangle &= |1/2, 1/2\rangle |1, 1\rangle , & |\phi_4\rangle &= |1/2, -1/2\rangle |1, 1\rangle , \\ |\phi_2\rangle &= |1/2, 1/2\rangle |1, 0\rangle , & |\phi_5\rangle &= |1/2, -1/2\rangle |1, 0\rangle , \\ |\phi_3\rangle &= |1/2, 1/2\rangle |1, -1\rangle , & |\phi_6\rangle &= |1/2, -1/2\rangle |1, -1\rangle , \\ |\phi_7\rangle &= |1/2, 1/2\rangle |0, 0\rangle , & |\phi_8\rangle &= |1/2, -1/2\rangle |0, 0\rangle . \end{aligned} \quad [3-4]$$

The eigenvalue of \hat{H}_0 (the Hamiltonian in the frame rotating at ν_S) associated with the function $|I, M_I\rangle |S, M_S\rangle$ is $-(\nu_I - \nu_S)M_I + J_{IS}M_I M_S + J_{SS}[2S(S+1)-3]/4$. The functions $|\phi_1\rangle$ to $|\phi_6\rangle$ belong to the S_2 total spin $S = 1$ (triplet) manifold, while $|\phi_7\rangle$ and $|\phi_8\rangle$ form the S_2 total spin $S=0$ (singlet) manifold. Since there is no mixing of the singlet and triplet S_2 spin states by any rf pulses or decoupling, the 8×8 IS_2 problem reduces to a 6×6 problem associated with the triplet manifold and a 2×2 problem associated with the singlet manifold. It should be noted that the order of eigenfunctions of \hat{H}_0 differs from the order used in the simulation scheme (Section II.4) since it is more convenient here to have the blocking with respect to total $S=1$ and $S=0$.

The equations of motion for the triplet manifold, can be written as

$$\begin{aligned} \frac{d}{dt}(\rho_{11}, \rho_{22}, \rho_{33}, \rho_{13}, \rho_{31}) &= (\rho_{11}, \rho_{22}, \rho_{33}, \rho_{13}, \rho_{31}) \tilde{KW}_1 \\ &+ 2\pi i J_{IS}(0, 0, 0, \rho_{13}, -\rho_{31}) , \end{aligned} \quad [3-5]$$

$$\begin{aligned} \frac{d}{dt}(\rho_{12}, \rho_{21}, \rho_{23}, \rho_{32}) &= (\rho_{12}, \rho_{21}, \rho_{23}, \rho_{32}) \tilde{KW}_2 \\ &+ 2\pi i J_{IS}(\rho_{12}, -\rho_{21}, \rho_{23}, -\rho_{32}) , \end{aligned} \quad [3-6]$$

$$\frac{d}{dt}(\rho_{14}, \rho_{25}, \rho_{36}, \rho_{16}, \rho_{34}) = (\rho_{14}, \rho_{25}, \rho_{36}, \rho_{16}, \rho_{34}) \times$$

$$[KW_1 - 2\pi i(\nu_I - \nu_S) \mathbf{1}] + 2\pi i J_{IS}(\rho_{14}, 0, -\rho_{36}, 0, 0) , \quad [3-7]$$

$$\frac{d}{dt}(\rho_{15}, \rho_{24}, \rho_{26}, \rho_{35}) = (\rho_{15}, \rho_{24}, \rho_{26}, \rho_{35}) \times$$

$$[KW_1 - i2\pi(\nu_I - \nu_S) \mathbf{1}] + 2\pi i J_{IS}(\rho_{15}, -\rho_{24}, -\rho_{26}, \rho_{35}) , \quad [3-8]$$

$$\frac{d}{dt}(\rho_{44}, \rho_{55}, \rho_{66}, \rho_{46}, \rho_{64}) = (\rho_{44}, \rho_{55}, \rho_{66}, \rho_{46}, \rho_{64}) KW_1$$

$$+ i2\pi J_{IS}(0, 0, 0, -\rho_{46}, \rho_{64}) \quad [3-9]$$

and

$$\frac{d}{dt}(\rho_{45}, \rho_{54}, \rho_{56}, \rho_{65}) = (\rho_{45}, \rho_{54}, \rho_{56}, \rho_{65}) KW_2$$

$$+ i2\pi J_{IS}(-\rho_{45}, \rho_{54}, -\rho_{56}, \rho_{65}) , \quad [3-10]$$

where $\mathbf{1}$ is a unit matrix of appropriate dimension,

$$\tilde{W}_1 = \begin{bmatrix} -1 & 1 & 0 & -1/2 & -1/2 \\ 1 & -2 & 1 & 1 & 1 \\ 0 & 1 & -1 & -1/2 & -1/2 \\ -1/2 & 1 & -1/2 & -1 & 0 \\ -1/2 & 1 & -1/2 & 0 & -1 \end{bmatrix}, \quad [3-11]$$

and

$$\tilde{W}_2 = \begin{bmatrix} -3/2 & 1 & 1 & -1/2 \\ 1 & -3/2 & -1/2 & 1 \\ 1 & -1/2 & -3/2 & 1 \\ -1/2 & 1 & 1 & -3/2 \end{bmatrix}. \quad [3-12]$$

The equation of motion for an element below the diagonal which is not coupled to elements above the diagonal (e.g. ρ_{41}) is just the complex conjugate of the equation of motion for the corresponding element above the diagonal (e.g. ρ_{14}).

We are interested only in the case of strong decoupling, so we shall assume that the decoupler power is sufficiently high that $K \gg J_{IS}$, so that the terms involving J_{IS} in Equations [3-5] - [3-10] can be neglected, and each of these equations reduces to the form

$$\frac{d\vec{\rho}}{dt} = \vec{\rho} [\tilde{K}W + i2\pi \Lambda \tilde{1}] , \quad [3-13]$$

where \tilde{W} is a real symmetric matrix of numbers and Λ is a frequency variable (which may be zero). The general solution to Equation [3-13] is

$$\rho_{ij}(t) = \sum_{k,l,\alpha} \tilde{U}_{ij;\alpha} \tilde{U}_{kl;\alpha} \rho_{kl}(0) \exp[(\lambda_{\alpha\alpha} K - i\Lambda)t], \quad [3-14]$$

where $\rho_{kl}(0)$ is the kl element of the density matrix at the beginning of the decoupling period. \tilde{U} and $\tilde{\lambda}$ are the eigenvectors and eigenvalues of the supermatrix \tilde{W} and satisfy the eigenvalue equation

$$\tilde{W} \tilde{U} = \tilde{U} \tilde{\lambda}, \quad [3-15]$$

with $\tilde{\lambda}$ a diagonal supermatrix. The index α in Equation [3-14] runs over all columns of \tilde{U} (i.e. all pairs of indices ij of ρ_{ij}). The matrices \tilde{W} will always have negative or zero eigenvalues. This means that the terms in Equation [3-14] for the negative eigenvalues will have exponentially damped oscillatory time-dependence, while those terms in Equation [3-14] associated with zero eigenvalues simply oscillate at frequency Λ with no damping. Thus, at long times, the transient effects which characterize the initial part of the decoupling period will have died away and the density matrix elements will have obtained "steady state" values given by

$$\vec{\rho}(t) = \vec{\rho}(0) \tilde{P} \exp(-2\pi i \Lambda t) , \quad [3-16]$$

where the elements of the supermatrix \tilde{P} are defined by

$$P_{ij;kl} = \sum_{\alpha} U_{ij;\alpha} U_{kl;\alpha} , \quad [3-17]$$

with the sum over α restricted to those columns of \tilde{U} associated with the zero eigenvalues of \tilde{W} . It is the density matrix given by Equation [3-16] which characterizes the spin system at the end of a period of decoupling. If the duration t of the decoupling period is too short, or the decoupler power is too low, this "steady state" of the spin system will not be attained during the decoupling period.

It should be noted that each block of density matrix elements which are connected by the decoupling interaction can be characterized by a constant value of $\Delta M_I = M_{Ii} - M_{Ij}$, where M_{Ii} is the eigenvalue of \hat{I}_z for the basis function $|\phi_i\rangle$ (see Equation [3-4]), for all members ρ_{ij} within a given block. Hence the frequency Λ in Equations [3-13], [3-14] and [3-16] associated with a particular block of interconnected elements is equal to $\Delta M_I(\nu_I - \nu_S)$.

For the triplet S_2 manifold of the IS_2 spin system, Equations [3-5], [3-7] and [3-9] reduce to [3-13] with $\tilde{W} =$

\tilde{W}_1 , and with $\Lambda = 0$, $(v_I - v_S)$, and 0 respectively. The steady state solutions for each of the blocks of 5 connected elements $\{p_{11}, p_{22}, p_{33}, p_{13}, p_{31}\}$, $\{p_{14}, p_{25}, p_{36}, p_{16}, p_{34}\}$ and $\{p_{44}, p_{55}, p_{66}, p_{46}, p_{64}\}$ are given by Equation [3-17] with $\tilde{P} = \tilde{P}_1$,

$$\tilde{P}_1 = \begin{bmatrix} 3/8 & 1/4 & 3/8 & -1/8 & -1/8 \\ 1/4 & 1/2 & 1/4 & 1/4 & 1/4 \\ 3/8 & 1/4 & 3/8 & -1/8 & -1/8 \\ -1/8 & 1/4 & -1/8 & 3/8 & 3/8 \\ -1/8 & 1/4 & -1/8 & 3/8 & 3/8 \end{bmatrix}, \quad [3-18]$$

and with $\Lambda = 0$, $(v_I - v_S)$ and 0 respectively. Equations [3-6], [3-8] and [3-10] reduce to Equation [3-13] when $K \gg J_{IS}$, with $\tilde{W} = \tilde{W}_2$, and with $\Lambda = 0$, $(v_I - v_S)$, 0 respectively. The steady state solutions for each of the blocks of 4 connected elements $\{p_{12}, p_{21}, p_{23}, p_{32}\}$, $\{p_{15}, p_{24}, p_{26}, p_{35}\}$ and $\{p_{45}, p_{54}, p_{56}, p_{65}\}$ are given by Equation [3-17] with $\tilde{P} = \tilde{P}_2$,

$$\tilde{P}_2 = (1/4) \begin{bmatrix} 1 & 1 & 1 & 1 \\ 1 & 1 & 1 & 1 \\ 1 & 1 & 1 & 1 \\ 1 & 1 & 1 & 1 \end{bmatrix}, \quad [3-19]$$

and with $\Lambda = 0$, $(\nu_I - \nu_S)$ and 0 respectively.

The equation of motion for the density matrix elements associated with the singlet S_2 spin states are

$$\frac{d\rho_{77}}{dt} = \frac{d\rho_{88}}{dt} = 0 ,$$

and

[3-20]

$$\frac{d\rho_{78}}{dt} = -i2\pi(\nu_I - \nu_S)\rho_{78}$$

with solutions (Equation [3-17] with $p = 1$)

$$\rho_{77}(t) = \rho_{77}(0) ,$$

$$\rho_{88}(t) = \rho_{88}(0)$$

[3-21]

and $\rho_{78}(t) = \rho_{78}(0) \exp[-i2\pi(\nu_I - \nu_S)t]$.

These elements are not influenced by the decoupler in that the singlet S_2 state is non-magnetic so that the singlet manifold of IS_2 behaves exactly like an I_1 spin system does under S decoupling.

Equations [3-17], [3-19] and [3-21] give the density matrix elements in the frame rotating at frequency ν_S about the laboratory z-axis. It is more convenient to have the density matrix elements in the laboratory frame since they display the full frequency dependence of the

system. The transformation from the ν_S rotating frame to the laboratory coordinates can be effected using the relationship in Equation [2-26]. Taking into account the frequency dependence of $\vec{\rho}^{\text{lab}}(t)$ in Equation [3-16], one obtains

$$\vec{\rho}^{\text{lab}}(t) = \vec{\rho}^{\text{lab}}(0) \underset{\sim}{P} \underset{\sim}{S}(t) , \quad [3-22]$$

where $\underset{\sim}{S}(t)$ is a diagonal supermatrix with elements

$$S_{ij;ij}(t) = \exp\{2\pi i[\nu_I(M_{Ij}-M_{Ii}) + \nu_S(M_{Sj}-M_{Si})]t\} . \quad [3-23]$$

In writing Equation [3-23], it has been assumed that the laboratory and rotating frames coincide at time zero. The frequencies in the exponential arguments in Equation [3-23] are the frequencies for the transition from state j to state i for the case $J_{IS} = 0$, i.e. they are the "decoupled" transition frequencies.

b. IS and IS₃ Spin Systems

For the IS spin system, with the eigenbasis labelled as,

$$\begin{aligned}
|\phi_1\rangle &= |1/2, 1/2\rangle |1/2, 1/2\rangle, & |\phi_3\rangle &= |1/2, -1/2\rangle |1/2, 1/2\rangle, \\
|\phi_2\rangle &= |1/2, 1/2\rangle |1/2, -1/2\rangle, & |\phi_4\rangle &= |1/2, -1/2\rangle |1/2, -1/2\rangle,
\end{aligned}$$

[3-24]

the equations of motion (Equation [3-3]) can be decomposed into sets of coupled differential equations with the coupled sets $\{\rho_{11}, \rho_{22}\}$, $\{\rho_{12}, \rho_{21}\}$, $\{\rho_{13}, \rho_{24}\}$, $\{\rho_{33}, \rho_{44}\}$ and $\{\rho_{34}, \rho_{43}\}$. In the limit of $K \gg J_{IS}$, each of these coupled sets of 8 equations reduces to Equation [3-13] with $\tilde{W} = \tilde{W}_3$, where

$$\tilde{W}_3 = (1/2) \begin{bmatrix} -1 & 1 \\ 1 & -1 \end{bmatrix} \quad [3-25]$$

and the frequency $\Lambda = \Delta M_I(\nu_I - \nu_S)$, with ΔM_I characteristic of the particular pair of coupled elements. The steady state values of the density matrix elements in the laboratory frame are given by Equation [3-23] with $\tilde{P} = \tilde{P}_3$ where

$$\tilde{P}_3 = (1/2) \begin{bmatrix} 1 & 1 \\ 1 & 1 \end{bmatrix}. \quad [3-26]$$

For the IS_3 system, the eigenfunctions of \hat{H}_0 can be grouped into irreducible sets belonging to total S spin 3/2, 1/2 and 1/2'. The basis functions used are then,

$$\begin{aligned}
|\phi_1\rangle &= |1/2, 1/2\rangle |3/2, 3/2\rangle, & |\phi_5\rangle &= |1/2, -1/2\rangle |3/2, 3/2\rangle, \\
|\phi_2\rangle &= |1/2, 1/2\rangle |3/2, 1/2\rangle, & |\phi_6\rangle &= |1/2, -1/2\rangle |3/2, 1/2\rangle, \\
|\phi_3\rangle &= |1/2, 1/2\rangle |3/2, -1/2\rangle, & |\phi_7\rangle &= |1/2, -1/2\rangle |3/2, -1/2\rangle, \\
|\phi_4\rangle &= |1/2, 1/2\rangle |3/2, -3/2\rangle, & |\phi_8\rangle &= |1/2, -1/2\rangle |3/2, -3/2\rangle,
\end{aligned}$$

[3-27]

$$\begin{aligned}
|\phi_9\rangle &= |1/2, 1/2\rangle |1/2, 1/2\rangle, & |\phi_{11}\rangle &= |1/2, -1/2\rangle |1/2, 1/2\rangle, \\
|\phi_{10}\rangle &= |1/2, 1/2\rangle |1/2, -1/2\rangle, & |\phi_{12}\rangle &= |1/2, -1/2\rangle |1/2, -1/2\rangle, \\
|\phi_{13}\rangle &= |1/2, 1/2\rangle |1/2', 1/2\rangle, & |\phi_{15}\rangle &= |1/2, -1/2\rangle |1/2', 1/2\rangle, \\
|\phi_{14}\rangle &= |1/2, 1/2\rangle |1/2', -1/2\rangle, & |\phi_{16}\rangle &= |1/2, -1/2\rangle |1/2', -1/2\rangle,
\end{aligned}$$

where the prime is used to distinguish the two irreducible sets of functions with total spin $1/2$. Since rf pulses and decoupling do not cause transitions between levels of different irreducible sets, the IS_3 problem can be broken down into one 8×8 and two 4×4 problems. Each of the 4×4 blocks of elements of the density matrix in IS_3 behave in exactly the same way as the elements of the IS density matrix given above, so they are not considered further. The 8×8 block of the IS_3 density matrix associated with the total spin $S = 3/2$ manifold has equations of motion which can be grouped into coupled sets for the ordered groups of elements:

$\{\rho_{11}, \rho_{22}, \rho_{33}, \rho_{44}, \rho_{13}, \rho_{31}, \rho_{24}, \rho_{42}\},$
 $\{\rho_{14}, \rho_{23}, \rho_{32}, \rho_{41}, \rho_{12}, \rho_{34}, \rho_{21}, \rho_{43}\},$
 $\{\rho_{15}, \rho_{26}, \rho_{37}, \rho_{48}, \rho_{17}, \rho_{35}, \rho_{28}, \rho_{46}\},$
 $\{\rho_{18}, \rho_{27}, \rho_{36}, \rho_{45}, \rho_{16}, \rho_{38}, \rho_{25}, \rho_{47}\},$
 $\{\rho_{55}, \rho_{66}, \rho_{77}, \rho_{88}, \rho_{57}, \rho_{75}, \rho_{68}, \rho_{88}\}$ and
 $\{\rho_{58}, \rho_{67}, \rho_{76}, \rho_{85}, \rho_{56}, \rho_{78}, \rho_{65}, \rho_{87}\}.$

In the limit of $K \gg J_{IS}$, each of these coupled sets of equations reduces to Equation [3-13] with $\tilde{W} = \tilde{W}_4$, where

$$\tilde{W}_4 = \begin{bmatrix} -3/2 & 3/2 & 0 & 0 & -\sqrt{3}/2 & -\sqrt{3}/2 & 0 & 0 \\ 3/2 & -7/2 & 2 & 0 & \sqrt{3} & \sqrt{3} & -\sqrt{3}/2 & -\sqrt{3}/2 \\ 0 & 2 & -7/2 & 3/2 & -\sqrt{3}/2 & -\sqrt{3}/2 & \sqrt{3} & \sqrt{3} \\ 0 & 0 & 3/2 & -3/2 & 0 & 0 & -\sqrt{3}/2 & -\sqrt{3}/2 \\ -\sqrt{3}/2 & \sqrt{3} & -\sqrt{3}/2 & 0 & -5/2 & 0 & 3/2 & 0 \\ -\sqrt{3}/2 & \sqrt{3} & -\sqrt{3}/2 & 0 & 0 & -5/2 & 0 & 3/2 \\ 0 & -\sqrt{3}/2 & \sqrt{3} & -\sqrt{3}/2 & 3/2 & 0 & -5/2 & 0 \\ 0 & -\sqrt{3}/2 & \sqrt{3} & -\sqrt{3}/2 & 0 & 3/2 & 0 & -5/2 \end{bmatrix}, \quad [3-28]$$

and the frequency $\Lambda = \Delta M_I(\nu_I - \nu_S)$, with M_I characteristic of the particular set of eight coupled elements. The steady state density matrix in the laboratory frame is given by Equation [3-23] with $\tilde{P} = \tilde{P}_4$, where

$$\tilde{P}_4 = \begin{bmatrix} 5/16 & 3/16 & 3/16 & 5/16 & -\sqrt{3}/16 & -\sqrt{3}/16 & -\sqrt{3}/16 & -\sqrt{3}/16 \\ 3/16 & 5/16 & 5/16 & 3/16 & \sqrt{3}/16 & \sqrt{3}/16 & \sqrt{3}/16 & \sqrt{3}/16 \\ 3/16 & 5/16 & 5/16 & 3/16 & \sqrt{3}/16 & \sqrt{3}/16 & \sqrt{3}/16 & \sqrt{3}/16 \\ 5/16 & 3/16 & 3/16 & 5/16 & -\sqrt{3}/16 & -\sqrt{3}/16 & -\sqrt{3}/16 & -\sqrt{3}/16 \\ -\sqrt{3}/16 & \sqrt{3}/16 & \sqrt{3}/16 & -\sqrt{3}/16 & 3/16 & 3/16 & 3/16 & 3/16 \\ -\sqrt{3}/16 & \sqrt{3}/16 & \sqrt{3}/16 & -\sqrt{3}/16 & 3/16 & 3/16 & 3/16 & 3/16 \\ -\sqrt{3}/16 & \sqrt{3}/16 & \sqrt{3}/16 & -\sqrt{3}/16 & 3/16 & 3/16 & 3/16 & 3/16 \\ -\sqrt{3}/16 & \sqrt{3}/16 & \sqrt{3}/16 & -\sqrt{3}/16 & 3/16 & 3/16 & 3/16 & 3/16 \end{bmatrix}.$$

[3-29]

c. Spherical Randomization Decoupling

Spherical randomization decoupling, introduced by Pegg et al. (52), differs from normal noise decoupling in that the phase of the decoupler is randomly switched among the 0° , 90° , 180° and 270° channels by the noise modulation rather than between the 0° and 180° phases normally used for decoupling. The equation of motion of the density operator during spherical randomization decoupling is

$$\frac{d\hat{\rho}}{dt} = i[\hat{\rho}, \hat{H}_0] - \kappa\{[\hat{S}_x, [\hat{S}_x, \hat{\rho}]] + [\hat{S}_y, [\hat{S}_y, \hat{\rho}]]\} \quad [3-30]$$

which differs from Equation [3-1] only by the presence of the double commutator involving \hat{S}_y . There are no cross

terms of the form $[\hat{S}_x, [\hat{S}_y, \hat{\rho}]]$ in Equation [3-30] because the cross correlation function for x- and y-components of the decoupling field vanishes. Equation [3-30] can be represented in the form of Equation [3-3] and in the limit of $K \gg J_{IS}$, it will break down into a number of collections of elements which satisfy Equation [3-13] and whose steady state values in the laboratory frame will be given by Equation [3-23].

For the IS system represented in the basis (Equation [3-24]) the sets $\{\rho_{11}, \rho_{22}\}$, $\{\rho_{13}, \rho_{14}\}$ and $\{\rho_{33}, \rho_{44}\}$ will have associated with them \tilde{W}_3 and \tilde{P}_3 just as they did for normal decoupling. The sets $\{\rho_{12}, \rho_{21}\}$ and $\{\rho_{14}, \rho_{23}\}$, however, are associated with

$$\tilde{W}_5 = \begin{bmatrix} -1 & 0 \\ 0 & -1 \end{bmatrix} . \quad [3-31]$$

Since \tilde{W}_5 has no zero eigenvalues, the corresponding \tilde{P} supermatrix is the null supermatrix, which implies that ρ_{12} , ρ_{21} , ρ_{14} and ρ_{23} vanish during the decoupling process. Thus the only off-diagonal elements of $\tilde{\rho}$ which remain finite during decoupling are ρ_{13} , ρ_{24} , ρ_{31} and ρ_{42} which correspond to the perpendicular I magnetization.

For the IS_2 system represented in the basis (Equation [3-4]) the sets of elements $\{\rho_{11}, \rho_{22}, \rho_{33}, \rho_{13}, \rho_{31}\}$,

$\{p_{14}, p_{25}, p_{36}, p_{16}, p_{34}\}$ and $\{p_{44}, p_{55}, p_{66}, p_{46}, p_{64}\}$ have associated with them a \tilde{W} supermatrix:

$$\tilde{W}_6 = \begin{bmatrix} -2 & 2 & 0 & 0 & 0 \\ 2 & -4 & 2 & 0 & 0 \\ 0 & 2 & -2 & 0 & 0 \\ 0 & 0 & 0 & -2 & 0 \\ 0 & 0 & 0 & 0 & -2 \end{bmatrix}, \quad [3-32]$$

which has the corresponding \tilde{P} supermatrix:

$$\tilde{P}_6 = (1/3) \begin{bmatrix} 1 & 1 & 1 & 0 & 0 \\ 1 & 1 & 1 & 0 & 0 \\ 1 & 1 & 1 & 0 & 0 \\ 0 & 0 & 0 & 0 & 0 \\ 0 & 0 & 0 & 0 & 0 \end{bmatrix}. \quad [3-33]$$

\tilde{P}_6 is quite different from the corresponding supermatrix \tilde{P}_1 for the normal decoupling case. The 4-member sets of elements for IS_2 : $\{p_{12}, p_{21}, p_{23}, p_{32}\}$, $\{p_{15}, p_{24}, p_{26}, p_{35}\}$, and $\{p_{45}, p_{54}, p_{56}, p_{65}\}$ satisfy Equation [3-13] with $\tilde{W} = \tilde{W}_7$, where

$$\tilde{W}_7 = \begin{bmatrix} -3 & 0 & 2 & 0 \\ 0 & -3 & 0 & 2 \\ 2 & 0 & -3 & 0 \\ 0 & 2 & 0 & -3 \end{bmatrix}, \quad [3-34]$$

which has no zero eigenvalues so that the corresponding \tilde{p} supermatrix is the null supermatrix and all of these elements are destroyed by spherical randomization decoupling. The elements ρ_{77} , ρ_{78} and ρ_{88} of the IS_2 density matrix are not affected by either type of S-decoupling.

For the spin $S = 3/2$ block of the IS_3 system represented in Equation [3-27], the sets of elements $\{\rho_{11}, \rho_{22}, \rho_{33}, \rho_{44}, \rho_{13}, \rho_{31}, \rho_{24}, \rho_{42}\}$, $\{\rho_{15}, \rho_{26}, \rho_{37}, \rho_{48}, \rho_{17}, \rho_{35}, \rho_{28}, \rho_{46}\}$ and $\{\rho_{55}, \rho_{66}, \rho_{77}, \rho_{88}, \rho_{57}, \rho_{75}, \rho_{68}, \rho_{86}\}$ have an associated \tilde{W} supermatrix:

$$\tilde{W}_8 = \begin{bmatrix} -3 & 3 & 0 & 0 & 0 & 0 & 0 & 0 \\ 3 & -7 & 4 & 0 & 0 & 0 & 0 & 0 \\ 0 & 4 & -7 & 3 & 0 & 0 & 0 & 0 \\ 0 & 0 & 3 & -3 & 0 & 0 & 0 & 0 \\ 0 & 0 & 0 & 0 & -7 & 0 & 3 & 0 \\ 0 & 0 & 0 & 0 & 0 & -7 & 0 & 3 \\ 0 & 0 & 0 & 0 & 3 & 0 & -7 & 0 \\ 0 & 0 & 0 & 0 & 0 & 3 & 0 & -7 \end{bmatrix}, \quad [3-35]$$

and a corresponding \tilde{P} supermatrix:

$$\tilde{P}_8 = (1/4) \begin{bmatrix} 1 & 1 & 1 & 1 & 0 & 0 & 0 & 0 \\ 1 & 1 & 1 & 1 & 0 & 0 & 0 & 0 \\ 1 & 1 & 1 & 1 & 0 & 0 & 0 & 0 \\ 1 & 1 & 1 & 1 & 0 & 0 & 0 & 0 \\ 0 & 0 & 0 & 0 & 0 & 0 & 0 & 0 \\ 0 & 0 & 0 & 0 & 0 & 0 & 0 & 0 \\ 0 & 0 & 0 & 0 & 0 & 0 & 0 & 0 \\ 0 & 0 & 0 & 0 & 0 & 0 & 0 & 0 \end{bmatrix} \quad [3-36]$$

The sets of elements $\{p_{14}, p_{23}, p_{32}, p_{41}, p_{12}, p_{34}, p_{21}, p_{43}\}$, $\{p_{18}, p_{27}, p_{36}, p_{45}, p_{16}, p_{38}, p_{25}, p_{47}\}$ and $\{p_{58}, p_{67}, p_{76}, p_{85}, p_{56}, p_{78}, p_{65}, p_{87}\}$, have an associated \tilde{W} supermatrix:

$$\tilde{W}_9 = \begin{bmatrix} -3 & 0 & 0 & 0 & 0 & 0 & 0 & 0 \\ 0 & -7 & 0 & 0 & 0 & 2\sqrt{3} & 2\sqrt{3} & 0 \\ 0 & 0 & -7 & 0 & 0 & 0 & 2\sqrt{3} & 2\sqrt{3} \\ 0 & 0 & 0 & -3 & 0 & 0 & 0 & 0 \\ 0 & 2\sqrt{3} & 0 & 0 & -5 & 0 & 0 & 0 \\ 0 & 2\sqrt{3} & 0 & 0 & 0 & -5 & 0 & 0 \\ 0 & 0 & 2\sqrt{3} & 0 & 0 & 0 & -5 & 0 \\ 0 & 0 & 2\sqrt{3} & 0 & 0 & 0 & 0 & -5 \end{bmatrix} \quad [3-37]$$

which has no zero eigenvalues so that the corresponding \tilde{P} supermatrix is the null supermatrix and all elements in these collections vanish with spherical randomization decoupling.

III.3 General Effects of Noise Decoupling on the Density Matrix

The results for normal decoupling show a number of interesting features:

- (a) the density matrix elements at steady state are linear combinations of appropriate collections of the elements of the density matrix at the beginning of the decoupling period, with "decoupled" frequency dependence (see Equations [3-22] and [3-23]);
- (b) the linear combinations of elements of $\tilde{\rho}(0)$ which make up a particular steady state element of $\tilde{\rho}(t)$ are not simple averages in most cases;
- (c) the decoupling mixes diagonal elements of $\tilde{\rho}(0)$, which have zero frequency dependence, with 2 quantum coherence elements, which oscillate at $\pm 2\nu_S$ in the laboratory frame; and
- (d) it mixes elements of $\tilde{\rho}(0)$ associated with transitions of the nuclei (frequency $\pm\nu_I$) with multiple quantum coherences (frequencies $\pm(\nu_I + 2\nu_S)$ and $\pm(\nu_I - 2\nu_S)$).

These features are in marked contrast to the results for spherical randomization mode decoupling where the elements of $\rho(t)$ are just simple averages of elements of $\rho(0)$; there is no mixing of diagonal elements with 2 quantum coherences nor is there mixing of the elements associated with I nucleus transitions with any multiple quantum coherences. Those elements of $\rho(t)$ which correspond to S nucleus transitions and to multiple quantum coherences are driven to zero by the spherical randomization decoupling field. The decoupling field in the usual noise decoupling experiment jumps randomly from the +x to the -x direction in the ν_S rotating frame so that the x-components of the S-magnetization and the real parts of $\rho(0)$ associated with multiple quantum coherences are unaffected by the decoupling field. In the spherical randomization mode, both real and imaginary parts of the off-diagonal elements of ρ are modulated by the decoupling field and those off-diagonal elements for which $\Delta M_S \neq 0$ are destroyed during the decoupling period.

It should be noted that the analysis in Section III.2 does not assume spatial inhomogeneity in the decoupling rf field, which is a requirement in the theory proposed by Pegg et al. (52). It is important that a theoretical description of decoupling be applicable in cases of low inhomogeneity as well as large inhomogeneity in the

decoupling rf field, since in modern spectrometers the transmitter coils are so designed to minimize spatial inhomogeneity of the pulse.

III.4 Implementation of the Decoupling Scheme.

The ordinary noise decoupling scheme discussed in Section III.2 is implemented as the subprogram DECOPL in the simulation program described in Chapter II. One of the major considerations in the implementation of the decoupling scheme is the identification of the collections of density matrix elements which are coupled by the equation of motion (Equation [3-2]). The double commutator in Equation [3-2] causes the coupling of the density matrix elements. The i,j matrix element of the double commutator is

$$[[\hat{\rho}, \hat{S}_x], \hat{S}_x]_{ij} = \sum_k (S_x^2)_{ik} \rho_{kj} - 2 \sum_{k,l} (S_x)_{ik} \rho_{kl} (S_x)_{lj} - \sum_k \rho_{ik} (S_x^2)_{kj} \quad [3-38]$$

and shows that the element ρ_{ij} is connected via the decoupling perturbation to those elements ρ_{kj} for which $(S_x^2)_{ik} \neq 0$, to ρ_{ik} for which $(S_x^2)_{kj} \neq 0$ and to those elements ρ_{kl} for which $(S_x)_{ik}(S_x)_{lj} \neq 0$. In order to

generate the lists of connected elements, the matrix representations \tilde{S}_x and \tilde{S}_x^2 are first generated. The set of elements coupled to a particular density matrix element ρ_{ij} , are found by scanning the density matrix for elements ρ_{kj} , ρ_{kl} and ρ_{ik} for the sets of indices k, l which give non-zero contributions to the right hand side of Equation [3-38]. The lists of coupled elements so generated are arranged in an array with appropriate labels, so that the number of elements in each coupled group can be easily ascertained. The group of connected density matrix elements, which occur in the $I_m S_n$ systems with $1 \leq m, n \leq 3$, can be classified according to the number of elements in the list: 1-element, 2-element, 4-element, 5-element and 8-element lists. During a period of spin decoupling, the density matrix elements in each set transform among themselves (Equation [3-16]), the transformation coefficients being given by the \tilde{P} matrices in Section III.2. The \tilde{P} matrices corresponding to the different lists are stored in the program so that the appropriate linear combinations can be computed. When the lists of coupled elements of the density matrix have been generated, the subprogram scans each list and determines the appropriate \tilde{P} matrix to be used in the transformation of elements of the particular list. To carry out the transformation, the coupled density matrix elements

multiplied by appropriate elements of the \tilde{P} supermatrices, are copied into a work area in the "data array". Bookkeeping information concerning the density matrix elements thus computed is then updated.

In the laboratory coordinate system, the off-diagonal elements exhibit "decoupled" frequency dependence, i.e. just the Zeeman frequencies of both nuclei. The "decoupled" frequency is represented in the simulation program by specifying the frequency dependence in a manner analogous to that for a free precession period (Chapter II) with an additional variable set to indicate that the spin-spin coupling constant J_{IS} is to be set to zero in all frequency variables for this decoupling interval.

III.5 Summary

A density matrix description of heteronuclear noise decoupling has been presented in this chapter. The equations of motion of the density matrix were set up and the method of solution described for the case of strong decoupler power. Two types of noise decoupling procedures were considered: (i) normal noise decoupling or planar randomization decoupling and (ii) spherical randomization decoupling. The implementation of the decoupling scheme in the simulation program was discussed. The next chapter

illustrates the application of the simulation program by analyzing various pulse sequences on representative spin systems. Included in the applications is an analysis of the decoupling experiments in which unexpected features are observed.

CHAPTER IV

APPLICATIONS

IV.1 Introduction

In this chapter, the capabilities of the simulation program are explored by including the results for simulations of several pulse sequences applied to a variety of spin systems. The examples have been chosen so as to illustrate various features of the program. The experiments simulated here include the Distortionless Enhancement by Polarization Transfer (DEPT) (31), a two-dimensional version of the DEPT experiment for selective observation of individual CH_n systems (54-57), the multiple-quantum coherence experiment INADEQUATE (58,59) and versions of the 2D gated J- δ correlation experiment which illustrate certain unexpected effects of spin decoupling (53). Many of the experiments mentioned above are not easily understood in terms of the motion of the magnetization vectors, since they involve pulses of intermediate flip angles, excitation and evolution of multiple-quantum coherences and so on. Throughout this

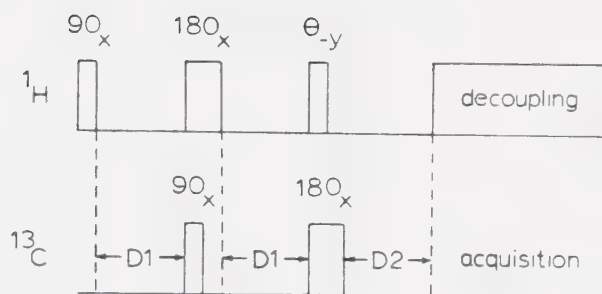
chapter, the notations used for certain terms have been modified so as to correspond with the convention used in program output. The v_I and v_S terms shall be denoted by VI and VS respectively and the spin system $I_m S_n$ shall be denoted by ImSn.

IV.2 Simulation of Experiments

a. DEPT Experiment

The DEPT sequence, shown in Figure 3, is an ingenious method for transferring polarization from one spin system to a heteronuclear spin system without phase or intensity distortions (31). Doddrell et al. (31) have described the behaviour of ^{13}CH , $^{13}\text{CH}_2$ and $^{13}\text{CH}_3$ fragments, when DEPT is applied, using Heisenberg vector diagrams, and have demonstrated some of the spectral editing capabilities of this sequence.

The most popular application of the DEPT sequence is to CH_n systems. The decoupling during the acquisition stage of the DEPT sequence (Figure 3) is optional. The relative intensities of coupled carbon signals from DEPT sequence for CH, CH_2 and CH_3 groups, are the normal characteristic ratios 1:1, 1:2:1 and 1:3:3:1 respectively. In contrast, the relative intensities from a refocussed-INEPT experiment (60,61) are distorted and



DEPT PULSE SEQUENCE FOR C-H SYSTEM

```

COMM ** DEPT SIMULATION FOR CH SYSTEM **
COMM      ** THETA PULSE=45 **
SPIN11S1
SET PULSC 45.0
WRDM
PULSSA+X
WRDM
PRECD1
SUBSD1=1/( 2J)
WRDM
PULSSB+X
PULSIA+X
WRDM
PRECD1
SUBSD1=1/( 2J)
WRDM
PULSSC-Y
PULSIB+X
WRDM
PRECD2
SUBSD2=1/( 2J)
WRDM
DCPLS T2
WRDM
MEASIXY0
STOP

```

Figure 3. Pulse sequence and input data for simulation of the CH DEPT experiment.

are respectively 1:1, 1:0:1, 1:1:1:1. The intensities of the signals detected after the DEPT sequence depend on the flip angle of the proton $\theta(-Y)$ pulse. For CH carbon signals, the maximum enhancement occurs at $\theta = \pi/2$, CH₂ carbon signals are largest at $\theta = \pi/4$ and CH₃ carbon signals have the maximum enhancement at $\theta = 0.196\pi$. The dependence of the signal intensities on the angle θ for CH, CH₂ and CH₃ systems are (31): $\sin \theta$, $\sin 2\theta$ and $(\sin \theta + \sin 3\theta)$ respectively. Spectral editing is accomplished by generating individual CH, CH₂ and CH₃ subspectra from appropriate combinations of spectra recorded at $\theta = \pi/4$, $\pi/2$ and $3\pi/4$. Spectral editing using the DEPT sequence is more exact than that using the refocussed INEPT sequence, since, in DEPT, the signal intensity depends mainly on the pulse angle and the J dependence of the signal intensity is a second order effect much smaller than that for INEPT. DEPT has another advantage over INEPT, in that it employs fewer pulses, so that DEPT is less vulnerable to intensity variations arising from inhomogeneous or imperfect rf pulses.

The input to the simulation program to perform the DEPT sequence with $\theta = 45^\circ$ on the ILS1 (¹³CH) system is shown in Figure 3 and the output in Figure 4. The diagonal elements of the density matrix are populations of the spin levels: ρ_{12} and ρ_{34} are proportional to the

DEPT CALCULATION FOR CH SYSTEM ; THETA PULSE=45

Initial Density Matrix

```
DM ( 1, 1) = +( 52.500, 0.0 )
DM ( 2, 2) = +( 47.500, 0.0 )
DM ( 3, 3) = +( -47.500, 0.0 )
DM ( 4, 4) = + (-52.500, 0.0 )
```

Density Matrix After 90(Proton) Pulse

```
DM ( 1, 1) = +( 2.500, 0.0 )
DM ( 1, 3) = +( 0.0, 50.000)
DM ( 2, 2) = +( -2.500, 0.0 )
DM ( 2, 4) = +( 0.0, 50.000)
DM ( 3, 3) = +( 2.500, 0.0 )
DM ( 4, 4) = +( -2.500, 0.0 )
```

Density Matrix After First Precession Period (D1=1/(2*J))

```
DM ( 1, 1) = +( 2.500, 0.0 )
DM ( 1, 3) = +( -50.000, 0.000)*EXP(2*PI*( 1.00 VS )=D1)
DM ( 2, 2) = +( -2.500, 0.0 )
DM ( 2, 4) = +( 50.000, 0.000)*EXP(2*PI*( 1.00 VS )=D1)
DM ( 3, 3) = +( 2.500, 0.0 )
DM ( 4, 4) = +( -2.500, 0.0 )
```

Density Matrix After 180(Proton)-90(Carbon) Pulses

```
DM ( 1, 2) = +( 0.0, 2.500)
DM ( 1, 4) = +( 0.0, -50.000)*EXP(2*PI*(-1.00 VS )=D1)
DM ( 2, 3) = +( 0.0, 50.000)*EXP(2*PI*(-1.00 VS )=D1)
DM ( 3, 4) = +( 0.0, 2.500)
```

Density Matrix After Second Precession Period (D1=1/(2*J))

```
DM ( 1, 2) = +( -2.500, 0.000)*EXP(2*PI*( 1.00 V1 )=D1)
DM ( 1, 4) = +( 0.0, -50.000)*EXP(2*PI*( 1.00 V1 )=D1)
DM ( 2, 3) = +( 0.0, 50.000)*EXP(2*PI*( -1.00 V1 )=D1)
DM ( 3, 4) = +( 2.500, 0.000)*EXP(2*PI*( 1.00 V1 )=D1)
```

Density Matrix After Theta(Proton)-180(Carbon) Pulses

```
DM ( 1, 2) = +( -1.768, -35.355)*EXP(2*PI*( -1.00 V1 )=D1)
DM ( 1, 4) = +( -1.768, 35.355)*EXP(2*PI*( -1.00 V1 )=D1)
DM ( 2, 3) = +( -1.768, -35.355)*EXP(2*PI*( 1.00 V1 )=D1)
DM ( 3, 4) = +( 1.768, 35.355)*EXP(2*PI*( -1.00 V1 )=D1)
```

Density Matrix After Third Precession Period (D2=1/(2*J))

```
DM ( 1, 2) = +( 35.355, -1.768)*EXP(2*PI*( -1.00 V1 )=D1)
DM ( 1, 4) = +( -1.768, 35.355)*EXP(2*PI*( 1.00 V1 )=D2)
DM ( 2, 3) = +( -1.768, -35.355)*EXP(2*PI*( 1.00 VS )=D1)
DM ( 3, 4) = +( 35.355, -1.768)*EXP(2*PI*( 1.00 VS )=D2)
```

Density Matrix During Decoupled Acquisition

```
DM ( 1, 2) = +( 35.355, -1.768)*EXP(2*PI*( 1.00 V1 )=T2)
DM ( 1, 4) = +( -0.884, 17.678)*EXP(2*PI*( 1.00 VS )=D1)
DM ( 2, 3) = +( -0.884, -17.678)*EXP(2*PI*( 1.00 VS )=D2)
DM ( 3, 4) = +( 35.355, -1.768)*EXP(2*PI*( 1.00 VS )=D1)
```

Carbon-13 Signals During Acquisition

```
SIGNAL = +( 70.710, -3.536)*EXP(2*PI*( 1.00 V1 )=T2)
SIGNAL = +( 70.710, -3.536)*EXP(2*PI*( -1.00 V1 )=D1)
SIGNAL = +( 70.710, -3.536)*EXP(2*PI*( 1.00 V1 )=D2)
```

Figure 4. Output of the DEPT simulation for CH system.

complex magnetizations ($M_x + iM_y$) associated with the I resonances at $\nu_I + J/2$ and $\nu_I - J/2$; ρ_{13} and ρ_{24} are proportional to the complex magnetizations associated with the S resonances at $\nu_S + J/2$ and $\nu_S - J/2$; ρ_{14} represents a two quantum coherence at frequency $\nu_I + \nu_S$; and ρ_{23} represents a zero quantum coherence at frequency $\nu_I - \nu_S$. As shown below, the density matrix information output by the program can be translated into a collection of magnetization vector diagrams for visualization of the magnetization transfer process. The magnetization diagrams for the DEPT experiment on the ^{13}CH system are given in Figure 5. In this figure, the axes of the double-quantum and zero-quantum rotating frames represent the real (X) and imaginary (Y) parts of the corresponding density matrix elements.

The step-by-step time evolution of the density matrix can be followed by translating the output in Figure 4 to conventional representation. The initial thermal equilibrium density matrix in the simple product basis $\{ |1/2, 1/2\rangle |1/2, 1/2\rangle, |1/2, 1/2\rangle |1/2, -1/2\rangle, |1/2, -1/2\rangle |1/2, 1/2\rangle \text{ and } |1/2, -1/2\rangle |1/2, -1/2\rangle \}$, given in Figure 4, can be represented as

CH

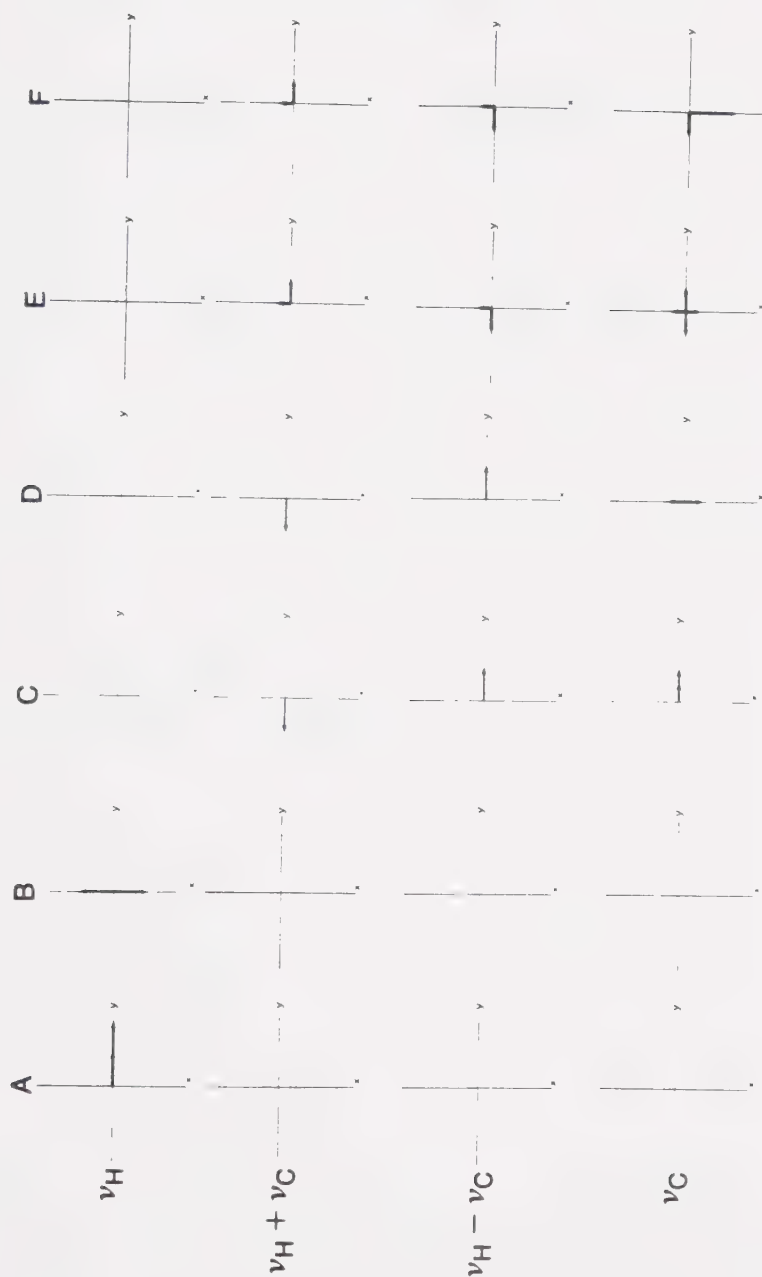


Figure 5. Magnetization diagrams for CH DEPT experiment. The labels ν_H , $\nu_H + \nu_C$, $\nu_H - \nu_C$, and ν_C indicate proton magnetization components, double-quantum coherence components, and carbon magnetization components, respectively. The labels x and y indicate real and imaginary parts of the density matrix elements. The positions of the magnetization and multiple quantum coherence components are shown: (A) after the initial 90°_x proton pulse; (B) after the D1 delay; (C) after the 90°_x carbon and 180°_x proton pulses, (D) after the second D1 delay; (E) after the θ_{-y} proton and 180°_x carbon pulses; and (F) after the last D2 delay.

$$\tilde{\rho}(0) = (1/2) \begin{bmatrix} \delta+\Delta & 0 & 0 & 0 \\ 0 & -\delta+\Delta & 0 & 0 \\ 0 & 0 & \delta-\Delta & 0 \\ 0 & 0 & 0 & -\delta-\Delta \end{bmatrix}, \quad [4-1]$$

where $\Delta = \gamma_H h H_0 / 8kT$, $\delta = \gamma_C h H_0 / 8kT$ and γ_H , γ_C , h , H_0 , k and T have their usual meanings. Δ and δ have been assigned numerical values 100 and 5 respectively in the simulation program. The proton magnetizations are put into the x-y plane by the proton 90° pulse (Figure 5A), and they precess at frequencies $VS \pm J/2$ in the frame rotating at the proton transmitter frequency. At time $D1 = 1/(2J_{CH})$, the phase difference between the two components is 180° (Figure 5B). At this point, the density matrix is given by

$$\tilde{\rho}(D1) = (1/2) \begin{bmatrix} \delta & 0 & a & 0 \\ 0 & -\delta & 0 & -a \\ a^* & 0 & \delta & 0 \\ 0 & -a^* & 0 & -\delta \end{bmatrix}, \quad [4-2]$$

where $a = -\Delta \exp\{2\pi i VS D1\}$. The carbon 90° pulse transfers the proton magnetization into the zero-quantum and double-quantum coherences, and puts the carbon thermal equilibrium z-magnetizations into the perpendicular plane

where they rotate at frequencies $\nu_I \pm J/2$ in the frame rotating at the carbon transmitter frequency (Figure 5C). During the second precession period, $D_1 = 1/(2J_{CH})$, the carbon magnetizations acquire a phase difference of 180° . In this period, the double-quantum coherence has acquired a further phase angle $2\pi(\nu_I + \nu_S)D_1$ in the frame rotating at the sum of the frequencies of the proton and carbon transmitters (Figure 5D). During this period, the zero-quantum coherence acquires an additional phase angle of $2\pi(\nu_I - \nu_S)D_1$ in the frame rotating at the frequency difference between the proton and carbon transmitters. It should be noted in the density matrix, that the purpose of the proton 180° pulse is to have the $2\pi \nu_S D_1$ phase angles in the proton magnetizations refocussed in the zero- and double-quantum coherences in the second precession period. The density matrix at the end of the second D_1 period is given by

$$\tilde{\rho}(2D_1) = \begin{bmatrix} 0 & c & 0 & b \\ c^* & 0 & -b^* & 0 \\ 0 & -b & 0 & -c \\ b^* & 0 & -c^* & 0 \end{bmatrix}, \quad [4-3]$$

where $b = -i\Delta \exp\{2\pi i \nu_I D_1\}$ and $c = -\delta \exp\{2\pi i \nu_I D_1\}$.

The proton 45° pulse transfers some of the zero-quantum and double-quantum coherences into carbon magnetization components (ρ_{12} and ρ_{34}) which have a phase difference of 180° (Figure 5E). These pulses also transfer some of the transverse carbon magnetization components into the zero- and double-quantum coherences (ρ_{23} and ρ_{14}) where they remain during the detection period. The purpose of the 180° carbon pulse applied along with the proton θ pulse is to effect the refocussing of the carbon resonance offsets. During the third $D2 = 1/(2J_{CH})$ precession period, the transferred carbon magnetization components are completely refocussed (Figure 5F). The phase angles of $\pm 2\pi$ VS D1 built up on the zero- and double-quantum coherences during the second precession period, and converted into phase angles of -2π VS D1 for each of the carbon magnetization components are exactly cancelled by the 2π VS D2 phase angle acquired during the third precession period. The density matrix just before the signal acquisition stage is given by

$$\tilde{\rho}(2D1 + D2) = \begin{bmatrix} 0 & d & 0 & e \\ d^* & 0 & e & 0 \\ 0 & e^* & 0 & d \\ e^* & 0 & d^* & 0 \end{bmatrix}, \quad [4-4]$$

where $d = (1/\sqrt{2})(\Delta - i\delta)$ and $e = (1/\sqrt{2})(-\delta + i\Delta)$
 $\exp\{2\pi i \text{ VS } D2\}$, since the time period $D1$ is identical to
 $D2$. The output in Figure 4 does not show the complete
distortionless magnetization transfer as clearly as one
might expect because of the program limitation which
restricts the appearance of any time variable more than
twice in a pulse sequence.

When the decoupler is turned on during the
acquisition period, both ρ_{12} and ρ_{34} precess at the
decoupled frequency ν_I and the signal measured with a
quadrature detector corresponds to a single resonance at
frequency offset ν_I from the carbon transmitter with an
intensity which corresponds to a mixture of transferred
proton magnetization and the normal Boltzmann carbon
magnetization. The signal expression output by the
program can be written as

$$\begin{aligned} \text{Signal} &= (1/\sqrt{2})(\Delta - i\delta) \exp\{2\pi i \nu_I (D1 - D2)\} \exp\{2\pi i \nu_I T2\} \\ &= (1/\sqrt{2})(\Delta - i\delta) \exp\{2\pi i \nu_I T2\} \end{aligned} \quad [4-5]$$

since $D1 = D2$. The Boltzmann carbon magnetization, which
correspond to the δ term in the output can be removed by
application of a carbon 90° pulse at the beginning of the
DEPT sequence or by alternating the phase of the proton θ

pulse by 180° on successive acquisitions. The signals are independent of the proton and carbon transmitter offsets during the free precession periods D1 and D2. This offset independence feature gives rise to distortionless polarization transfer, since the chemical shifts are all refocussed, regardless of their offset from the transmitter frequencies.

The coupled spectrum using the DEPT sequence has the carbon signal given by (Figure 6)

$$\text{Signal} = (1/2\sqrt{2})(\Delta - i\delta) [\exp\{2\pi i(VI + J/2)T_2\} + \exp\{2\pi i(VI - J/2)T_2\}] , \quad [4-6]$$

which corresponds to two lines at frequencies $VI + J/2$ and $VI - J/2$, with 1:1 relative intensity.

The dependence of the signal intensity on the pulse angle θ has been studied by carrying out the density matrix calculations with various values for the θ pulse. The simulation output is given in Figure 7. For transferred polarization from protons, the signal intensity dependence on the θ value corresponds to the general expression

$$\text{Signal} = \Delta \sin\theta \exp\{2\pi i VI T_2\} \quad [4-7]$$

INPUT FOR COUPLED DEPT EXPT ON CH SYSTEM

```

COMM  COUPLED DEPT SIMULATION FOR C-H SYSTEM
COMM      THETA PULSE=45
SPIN11S1
SET PULSC      45.0
PULSSA+X
PRECD1
SUBSD1=1/( 2J)
PULSSB+X
PULSIA+X
PRECD1
SUBSD1=1/( 2J)
PULSSC-Y
PULSIB+X
PRECD2
SUBSD2=1/( 2J)
PRECT2
MEASIXY0
STOP

```

OUTPUT FOR COUPLED DEPT EXPT ON CH SYSTEMCarbon-13 Signals During Coupled Acquisition

```

SIGNAL =      +( 35.355, -1.768)*EXPI(2*PI*(          1.00 VI    0.50 J  )*T2 )
               *EXPI(2*PI*(          -1.00 VI          )*D1 )
               *EXPI(2*PI*(          1.00 VI          )*D2 )

               +( 35.355, -1.768)*EXPI(2*PI*(          1.00 VI   -0.50 J  )*T2 )
               *EXPI(2*PI*(          -1.00 VI          )*D1 )
               *EXPI(2*PI*(          1.00 VI          )*D2 )

```

Figure 6. Input data and output from the simulation of CH coupled DEPT experiment.

SAMPLE INPUT FOR DEPT EXPT ON CH SYSTEM

```

COMM  DEPT SEQUENCE FOR C-H ; THETA PULSE ANGLE = 45
SPIN11S1
SET PULSC      45.0
PULSSA+X
PRECT1
PULSSB-X
PULSIA+X
PRECT1
SUBST1=1/( 2J)
PULSSC-Y
PULSIB-X
PRECD1
SUBSD1=1/( 2J)
MEASIXY0
STOP

```

OUTPUT FOR DEPT EXPT ON CH SYSTEM FOR VARIOUS THETA VALUES

Carbon-13 Signals During Decoupled Acquisition

```

Theta Pulse = 45 Degrees
SIGNAL =      + ( 70.711,  -3.536)*EXPI(2*PI*(          -1.00 VI          )*T1 )
          *EXPI(2*PI*(          1.00 VI          )*D1 )

```

```

Theta Pulse = 90 Degrees
SIGNAL =      +( 100.000,  -0.000)*EXPI(2*PI*(          -1.00 VI          )*T1 )
              *EXPI(2*PI*(          1.00 VI          )*D1 )

```

$$\text{SIGNAL} = \frac{\text{Theta Pulse} = 135 \text{ Degrees}}{+(-70.711, \quad 3.536) * \text{EXP}(2 * \text{PI} * \quad -1.00 \text{ VI} \quad) * \text{T1})}$$

Theta Pulse = 180 Degrees
 SIGNAL = + (0.0 , 5.000) * EXP I (2 * PI * -1.00 VI) * T1)
 * EXP I (2 * PI * 1.00 VI) * D1)

Figure 7. Simulation of the θ -pulse angle dependence in CH DEPT experiment. Carbon-13 signals corresponding to $\theta = 45^\circ, 90^\circ, 135^\circ$ and 180° are given.

as reported by Doddrell et al. (31).

Simulations of the behaviour of the $^{13}\text{CH}_2$ and $^{13}\text{CH}_3$ fragments with the DEPT sequence have been performed, and the output is given in Figure 8 and Figure 9 respectively. The results are shown in pictorial form in Figures 10 and 11 where the transfer of proton magnetization to the multiple quantum coherences and on to carbon magnetization is shown for CH_2 and CH_3 systems using the same scheme used in Figure 5 for the CH system. For clarity, the Boltzmann carbon magnetization components are not shown in Figures 10 and 11, since these may be removed by an initial carbon 90° pulse. The polarization transfer in all CH_n cases follows the same route: (i) the proton magnetization is transferred to zero- and double-quantum coherences by application of a carbon 90° pulse when the two components of the proton magnetization are 180° out of phase (Figures 10B-C and 11B-C); (ii) some of the zero- and double-quantum coherence is transferred to carbon magnetization by the proton $\theta(-y)$ pulse (Figures 10D-E and 11D-E); and (iii) the components of the transferred magnetization are allowed to precess until they are in phase and a net polarization transfer from the proton to carbon spin systems has taken place. In the CH_2 and CH_3 cases, there

DEPT CALCULATION ON C-H2 SYSTEM ; THETA PULSE = 45

Initial Density Matrix

```
DM ( 1, 1) = +( 102.500, 0.0 )
DM ( 2, 2) = +( 97.500, 0.0 )
DM ( 3, 3) = +( 2.500, 0.0 )
DM ( 4, 4) = +( -2.500, 0.0 )
DM ( 5, 5) = +( -97.500, 0.0 )
DM ( 6, 6) = +( -102.500, 0.0 )
DM ( 7, 7) = +( 2.500, 0.0 )
DM ( 8, 8) = +( -2.500, 0.0 )
```

Density Matrix After 90(Proton) Pulse

```
DM ( 1, 1) = +( 2.500, 0.0 )
DM ( 1, 3) = +( 0.0, 70.711)
DM ( 2, 2) = +( -2.500, 0.0 )
DM ( 2, 4) = +( 0.0, 70.711)
DM ( 3, 3) = +( 2.500, 0.0 )
DM ( 3, 5) = +( 0.0, 70.711)
DM ( 4, 4) = +( -2.500, 0.0 )
DM ( 4, 6) = +( 0.0, 70.711)
DM ( 5, 5) = +( 2.500, 0.0 )
DM ( 6, 6) = +( -2.500, 0.0 )
DM ( 7, 7) = +( 2.500, 0.0 )
DM ( 8, 8) = +( -2.500, 0.0 )
```

Density Matrix After 180(Proton)-90(Carbon) Pulses

```
DM ( 1, 2) = +( 0.0, 2.500)
DM ( 1, 4) = +( 0.0, -70.711)*EXPI(2*PI*( -1.00 VS )*D1 )
DM ( 2, 3) = +( 0.0, 70.711)*EXPI(2*PI*( -1.00 VS )*D1 )
DM ( 3, 4) = +( 0.0, 2.500)
DM ( 3, 6) = +( 0.0, -70.711)*EXPI(2*PI*( -1.00 VS )*D1 )
DM ( 4, 5) = +( 0.0, 70.711)*EXPI(2*PI*( -1.00 VS )*D1 )
DM ( 5, 6) = +( 0.0, 2.500)
DM ( 7, 8) = +( 0.0, 2.500)
```

Density Matrix After Theta(Proton)-180(Carbon) Pulses

```
DM ( 1, 2) = +( -50.000, 1.250)*EXPI(2*PI*( -1.00 VI )*D1 )
DM ( 1, 4) = +( 0.000, 1.768)*EXPI(2*PI*( -1.00 VI )*D1 )
DM ( 1, 6) = +( 50.000, 1.250)*EXPI(2*PI*( -1.00 VI )*D1 )
DM ( 2, 3) = +( 0.000, -1.768)*EXPI(2*PI*( 1.00 VI )*D1 )
DM ( 2, 5) = +( 50.000, -1.250)*EXPI(2*PI*( 1.00 VI )*D1 )
DM ( 3, 4) = +( 100.000, -0.000)*EXPI(2*PI*( -1.00 VI )*D1 )
DM ( 3, 6) = +( -0.000, -1.768)*EXPI(2*PI*( -1.00 VI )*D1 )
DM ( 4, 5) = +( -0.000, 1.768)*EXPI(2*PI*( 1.00 VI )*D1 )
DM ( 5, 6) = +( -50.000, 1.250)*EXPI(2*PI*( -1.00 VI )*D1 )
DM ( 7, 8) = +( 0.0, -2.500)*EXPI(2*PI*( -1.00 VI )*D1 )
```

Carbon-13 Signals During Decoupled Acquisition

```
SIGNAL = +( 199.999, -5.000)*EXPI(2*PI*( 1.00 VI )*T2 )
          *EXPI(2*PI*( -1.00 VI )*D1 )
          *EXPI(2*PI*( 1.00 VI )*D2 )
```

Figure 8. Density matrix and output from the simulation of CH₂ DEPT experiment.

DEPT CALCULATION ON C-H3 SYSTEM ; THETA PULSE = 45

Initial Density Matrix

```
DM ( 1, 1) = + ( 152.500, 0.0 )
DM ( 2, 2) = + ( 147.500, 0.0 )
DM ( 3, 3) = + ( 52.500, 0.0 )
DM ( 4, 4) = + ( 47.500, 0.0 )
DM ( 5, 5) = + ( -47.500, 0.0 )
DM ( 6, 6) = + ( -52.500, 0.0 )
DM ( 7, 7) = + ( -147.500, 0.0 )
DM ( 8, 8) = + ( -152.500, 0.0 )
DM ( 9, 9) = + ( 52.500, 0.0 )
DM (10,10) = + ( 47.500, 0.0 )
DM (11,11) = + ( -47.500, 0.0 )
DM (12,12) = + ( -52.500, 0.0 )
DM (13,13) = + ( 52.500, 0.0 )
DM (14,14) = + ( 47.500, 0.0 )
DM (15,15) = + ( -47.500, 0.0 )
DM (16,16) = + ( -52.500, 0.0 )
```

Density Matrix After 90(Proton) Pulse

```
DM ( 1, 1) = + ( 2.500, 0.0 )
DM ( 1, 3) = + ( 0.0, 86.602 )
DM ( 2, 2) = + ( -2.500, 0.0 )
DM ( 2, 4) = + ( 0.0, 86.602 )
DM ( 3, 3) = + ( 2.500, 0.0 )
DM ( 3, 5) = + ( 0.0, 100.000 )
DM ( 4, 4) = + ( -2.500, 0.0 )
DM ( 4, 6) = + ( 0.0, 100.000 )
DM ( 5, 5) = + ( 2.500, 0.0 )
DM ( 5, 7) = + ( 0.0, 86.602 )
DM ( 6, 6) = + ( -2.500, 0.0 )
DM ( 6, 8) = + ( 0.0, 86.602 )
DM ( 7, 7) = + ( 2.500, 0.0 )
DM ( 7, 9) = + ( -2.500, 0.0 )
DM ( 8, 8) = + ( -2.500, 0.0 )
DM ( 8, 10) = + ( 2.500, 0.0 )
DM ( 9, 9) = + ( 2.500, 0.0 )
DM ( 9, 11) = + ( 0.0, -50.000 )
DM (10,10) = + ( -2.500, 0.0 )
DM (10,12) = + ( 0.0, -50.000 )
DM (11,11) = + ( 2.500, 0.0 )
DM (12,12) = + ( -2.500, 0.0 )
DM (13,13) = + ( 2.500, 0.0 )
DM (13,15) = + ( 0.0, 50.000 )
DM (14,14) = + ( -2.500, 0.0 )
DM (14,16) = + ( 0.0, 50.000 )
DM (15,15) = + ( 2.500, 0.0 )
DM (16,16) = + ( -2.500, 0.0 )
```

Density Matrix After Theta(Proton)-180(Carbon) Pulses

```
DM ( 1, 2) = + ( 0.884, 53.033)*EXP1(2*P1)= (-1.00 V1) )=D1 )
DM ( 1, 4) = + ( 1.531, 30.618)*EXP1(2*P1)= (-1.00 V1) )=C1 )
DM ( 1, 6) = + ( 1.531, -30.619)*EXP1(2*P1)= (-1.00 V1) )=D1 )
DM ( 1, 8) = + ( 0.884, -53.033)*EXP1(2*P1)= (-1.00 V1) )=C1 )
DM ( 2, 3) = + ( 1.531, -30.618)*EXP1(2*P1)= (1.00 V1) )=D1 )
DM ( 2, 5) = + ( 1.531, 30.619)*EXP1(2*P1)= (1.00 V1) )=D1 )
DM ( 2, 7) = + ( 0.884, 53.033)*EXP1(2*P1)= (1.00 V1) )=D1 )
DM ( 3, 4) = + ( 0.884, -88.388)*EXP1(2*P1)= (-1.00 V1) )=D1 )
DM ( 3, 6) = + ( -0.884, -88.388)*EXP1(2*P1)= (-1.00 V1) )=D1 )
DM ( 3, 8) = + ( -1.531, 30.619)*EXP1(2*P1)= (-1.00 V1) )=D1 )
DM ( 4, 5) = + ( -0.884, 88.388)*EXP1(2*P1)= (1.00 V1) )=D1 )
DM ( 4, 7) = + ( -1.531, -30.619)*EXP1(2*P1)= (1.00 V1) )=D1 )
DM ( 5, 6) = + ( -0.884, 88.388)*EXP1(2*P1)= (-1.00 V1) )=D1 )
DM ( 5, 8) = + ( 1.531, 30.618)*EXP1(2*P1)= (-1.00 V1) )=D1 )
DM ( 6, 7) = + ( 1.531, -30.618)*EXP1(2*P1)= (1.00 V1) )=D1 )
DM ( 7, 8) = + ( -0.884, -53.033)*EXP1(2*P1)= (-1.00 V1) )=D1 )
DM ( 9,10) = + ( -1.768, -35.355)*EXP1(2*P1)= (-1.00 V1) )=D1 )
DM ( 9,12) = + ( 1.768, -35.355)*EXP1(2*P1)= (-1.00 V1) )=D1 )
DM (10,11) = + ( 1.768, 35.355)*EXP1(2*P1)= (1.00 V1) )=D1 )
DM (11,12) = + ( 1.768, 35.355)*EXP1(2*P1)= (-1.00 V1) )=D1 )
DM (13,14) = + ( -1.768, -35.355)*EXP1(2*P1)= (-1.00 V1) )=D1 )
DM (13,16) = + ( -1.768, 35.355)*EXP1(2*P1)= (-1.00 V1) )=D1 )
DM (14,15) = + ( -1.768, -35.355)*EXP1(2*P1)= (1.00 V1) )=D1 )
DM (15,16) = + ( 1.768, 35.355)*EXP1(2*P1)= (-1.00 V1) )=D1 )
```

Carbon-13 Signals During Decoupled Acquisition

```
SIGNAL = + ( 424.252, -7.071)*EXP1(2*P1)= (1.00 V1) )=T2 )
=EXP1(2*P1)= (-1.00 V1) )=D1 )
=EXP1(2*P1)= (1.00 V1) )=D2 )
```

Figure 9. Density matrix and output from the simulation of CH₃ DEPT experiment.



Figure 10. Magnetization diagrams for CH_2 DEPT experiment. The labels ν_H , $\nu_H + \nu_C$, $\nu_H - \nu_C$, and ν_C indicate proton magnetization components, double-quantum coherence components, and carbon magnetization components, respectively. The labels x and y indicate real and imaginary parts of the density matrix elements. The positions of the magnetization and multiple quantum coherence components are shown: (A) after the initial 90°_x proton pulse; (B) after the D1 delay; (C) after the 90°_x carbon and 180°_x proton pulses, (D) after the second D1 delay; (E) after the θ_{-y} proton and 180°_x carbon pulses; and (F) after the last D2 delay.



Figure 11. Magnetization diagrams for CH_3 DEPT experiment. The labels ν_H , $\nu_H + \nu_C$, $\nu_H - \nu_C$, and ν_C indicate proton magnetization components, double-quantum coherence components, and carbon magnetization components, respectively. The labels x and y indicate real and imaginary parts of the density matrix elements. The positions of the magnetization and multiple quantum coherence components are shown: (A) after the initial 90_x proton pulse; (B) after the D1 delay; (C) after the 90_x carbon and 180_x proton pulses, (D) after the second D1 delay; (E) after the θ_{-y} proton and 180_x carbon pulses; and (F) after the last D2 delay.

are several zero-quantum and double-quantum coherence components, and parts of these coherences are converted by the θ proton pulse into multiple-quantum coherences at frequencies $2\nu_S \pm \nu_I$ (for both CH_2 and CH_3), and at $3\nu_S \pm \nu_I$ (for CH_3). These multiple-quantum coherences are not shown in Figures 10 and 11 since they are not detected in the DEPT experiment.

For the CH_2 system, the computed signal intensity (Figure 8) can be written as

$$\text{Signal} = (\Delta - i\delta) \exp\{2\pi i \nu_I T_2\} , \quad [4-8]$$

in the case of decoupled acquisition. When the carbon spectrum is obtained in the absence of the proton decoupler, the signal intensities are given by (Figure 12)

$$\begin{aligned} \text{Signal} = & (\Delta/2 - i\delta/4) \exp\{2\pi i (\nu_I + J)T_2\} + \\ & (\Delta - i\delta/2) \exp\{2\pi i \nu_I T_2\} + \\ & (\Delta/2 - i\delta/4) \exp\{2\pi i (\nu_I - J)T_2\} , \end{aligned} \quad [4-9]$$

which corresponds to the characteristic 1:2:1 triplet. The dependence of the transferred polarization signal on the duration of the θ pulse has been studied (Figure 13). The transferred polarization follows the general expression

INPUT FOR COUPLED DEPT EXPT ON C-H2 SYSTEM

```

COMM  COUPLED DEPT EXPT FOR C-H2 SYSTEM ; THETA = 45
SPIN11S2
SET PULSC      45.0
PULSSA+X
PRECD1
SUBSD1=1/( 2J)
PULSSB+X
PULS1A+X
PRECD1
SUBSD1=1/( 2J)
PULSSC-Y
PULS1B+X
PRECD2
SUBSD2=1/( 2J)
PRECT2
MEAS1XY0
STOP

```

OUTPUT FOR COUPLED DEPT EXPT ON C-H2 SYSTEM

Carbon-13 Signals During Coupled Acquisition

SIGNAL =	+(50.000, -1.250)*EXPI(2*PI*(1.00 VI	1.00 J)*T2)
	*EXPI(2*PI*(-1.00 VI)*D1)
	*EXPI(2*PI*(1.00 VI)*D2)
	+(100.000, -2.500)*EXPI(2*PI*(1.00 VI)*T2)
	*EXPI(2*PI*(-1.00 VI)*D1)
	*EXPI(2*PI*(1.00 VI)*D2)
	+(50.000, -1.250)*EXPI(2*PI*(1.00 VI	-1.00 J)*T2)
	*EXPI(2*PI*(-1.00 VI)*D1)
	*EXPI(2*PI*(1.00 VI)*D2)

Figure 12. Output from the simulation of CH₂ coupled DEPT experiment.

OUTPUT FOR DEPT EXPT ON C-H₂ SYSTEM FOR VARIOUS THETA VALUES

Carbon-13 Signals During Decoupled Acquisition

Theta Pulse = 45 Degrees

```
SIGNAL =      +( 200.000,  -5.000)*EXPI(2*PI*(          -1.00 VI          )*T1 )
                  *EXPI(2*PI*(          1.00 VI          )*D1 )
```

Theta Pulse = 90 Degrees

```
SIGNAL =      +(   0.000,  -0.000)*EXPI(2*PI*(          -1.00 VI          )*T1 )
                  *EXPI(2*PI*(          1.00 VI          )*D1 )
```

Theta Pulse = 135 Degrees

```
SIGNAL =      +(-200.000,  -5.000)*EXPI(2*PI*(          -1.00 VI          )*T1 )
                  *EXPI(2*PI*(          1.00 VI          )*D1 )
```

Theta Pulse = 180 Degrees

```
SIGNAL =      +(   0.0   , -10.000)*EXPI(2*PI*(          -1.00 VI          )*T1 )
                  *EXPI(2*PI*(          1.00 VI          )*D1 )
```

Figure 13. Simulation of θ -pulse angle dependence in CH₂ DEPT experiment.

$$\text{Signal} = 2\Delta \sin(2\theta) \exp\{2\pi i \text{VI T2}\} , \quad [4-10]$$

which agrees with the results of Doddrell et al. (31).

Results for the CH_3 system are shown in Figure 9. The simulations of the DEPT experiment on the CH_3 system, with carbon signal acquisition in the absence of the proton decoupling shows the characteristic 1:3:3:1 quartet pattern. This result is shown in Figure 14. The simulations (Figure 15) for investigation of the θ -dependence of the CH_3 signal intensities agree with the $(\sin \theta + \sin 3\theta)$ dependence given by Doddrell et al. (31).

b. Selective 2D Heteronuclear Shift Correlation

Experiment

The spectrum editing capabilities of the DEPT sequence have been utilized by Levitt et al. (54), and Bendall et al. (55), to produce selective two dimensional heteronuclear shift correlation maps. A selective shift correlation map displays peaks arising from the shift correlation of only a particular type of CH_n group, thus making it possible to differentiate between signals from CH , CH_2 and CH_3 fragments. The pulse sequences used in both investigations (54,55) yield similar correlation maps, and the pulse sequence proposed by Levitt et al. (54) will be analyzed using the simulation program.

INPUT FOR COUPLED DEPT EXPT ON C-H3 SYSTEM

```

COMM DEPT SIMULATION FOR C-H3 SYSTEM ; THETA PULSE=45
SPIN11S3
SET PULSC 45.0
PULSSA+X
PRECD1
SUBSD1=1/( 2J)
PULSSB+X
PULSIA+X
PRECD1
SUBSD1=1/( 2J)
PULSSC-Y
PULSIB+X
PRECD2
SUBSD2=1/( 2J)
PRECT2
MEASIXY0
STOP

```

OUTPUT FOR COUPLED DEPT EXPT ON C-H3 SYSTEMCarbon-13 Signals During Coupled Acquisition

SIGNAL =	+(53.033, -0.884)*EXPI(2*PI*(1.00 VI	1.50 J)*T2)
	*EXPI(2*PI*(-1.00 VI)*D1)
	*EXPI(2*PI*(1.00 VI)*D2)
	+(159.099, -2.652)*EXPI(2*PI*(1.00 VI	0.50 J)*T2)
	*EXPI(2*PI*(-1.00 VI)*D1)
	*EXPI(2*PI*(1.00 VI)*D2)
	+(159.099, -2.652)*EXPI(2*PI*(1.00 VI	-0.50 J)*T2)
	*EXPI(2*PI*(-1.00 VI)*D1)
	*EXPI(2*PI*(1.00 VI)*D2)
	+(53.033, -0.884)*EXPI(2*PI*(1.00 VI	-1.50 J)*T2)
	*EXPI(2*PI*(-1.00 VI)*D1)
	*EXPI(2*PI*(1.00 VI)*D2)

Figure 14. Output from the simulation of CH₃ coupled DEPT experiment.

OUTPUT FOR DEPT EXPT ON C-H3 SYSTEM FOR VARIOUS THETA VALUES

Carbon-13 Signals During Decoupled Acquisition

Theta Pulse = 45 Degrees

```
SIGNAL =      +( 424.260, -7.071)*EXPI(2*PI*(          -1.00 V1          )*T1 )
               *EXPI(2*PI*(          1.00 V1          )*D1 )
```

Theta Pulse = 90 Dgrees

```
SIGNAL =      +( 0.000, -0.000)*EXP(2*PI*(          -1.00 VI          )*T1 )
               *EXP(2*PI*(          1.00 VI          )*D1 )
```

Theta pulse = 135 Degrees

```
SIGNAL =      +( 424.257,  7.071)*EXPI(2*PI*(          -1.00 VI          )*T1 )
              *EXPI(2*PI*(          1.00 VI          )*D1 )
```

Theta Pulse = 180 Degrees

```
SIGNAL = +( 0.000, 20.000)*EXPI(2*PI*(          -1.00 VI          )*T1 )
          *EXPI(2*PI*(          1.00 VI          )*D1 )
```

Figure 15. Simulation of θ -pulse angle dependence in CH_3 DEPT experiment.

The selective 2D shift correlation pulse sequence is shown in Figure 16. The original DEPT sequence (31) was modified to include a variable time period T_1 , during which the proton magnetizations are frequency labelled. Thus the proton magnetization at the end of the T_1 time period is modulated by proton resonance frequencies. After the introduction of this modulation, the DEPT sequence was used to transfer the modulated proton magnetization into carbon magnetization. The carbon signals acquired in the presence of proton decoupling is then a function of two time variables T_1 and T_2 . A two dimensional data set is acquired by collecting the FIDs (functions of T_2) for a series of values of T_1 . The two dimensional data is then Fourier transformed twice, with respect to the time variables T_2 and T_1 , to produce the shift correlation spectrum. The 2D spectrum has proton frequencies along the ν_1 dimension (Fourier conjugate of time T_1) and the carbon frequencies appear along the ν_2 dimension (Fourier conjugate of time T_2).

As mentioned in Section IV.2.a, the signals acquired after the DEPT pulse sequence depend on the θ -pulse duration, with the intensities proportional to $\sin \theta$, $\sin 2\theta$ and $(\sin \theta + \sin 3\theta)$ for CH , CH_2 and CH_3 systems respectively. The linear combinations of FID data at three different θ values have been used to generate the

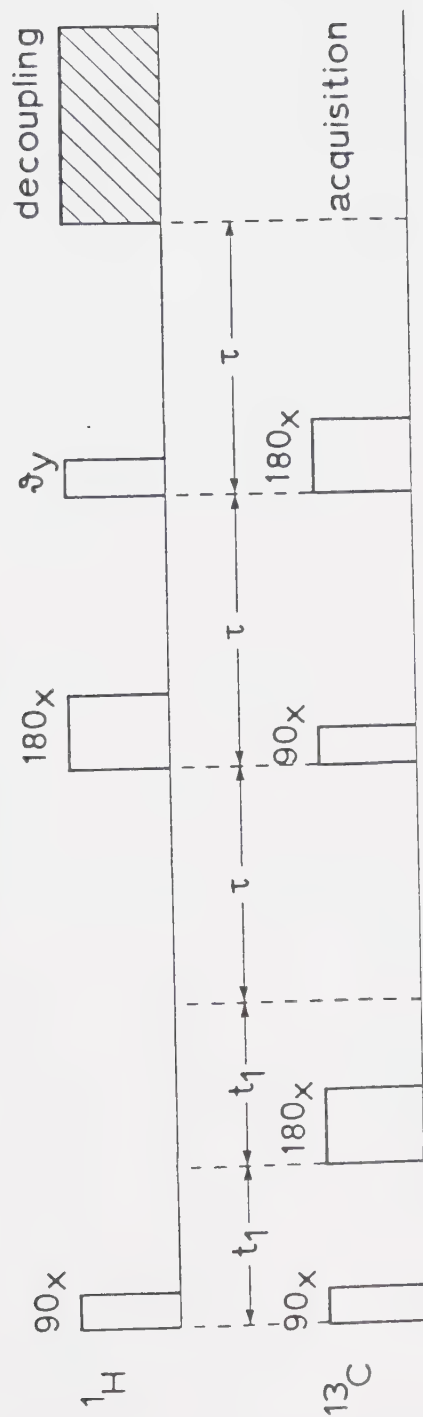


Figure 16. The selective 2D heteronuclear chemical shift correlation pulse sequence. t_1 is incremented in the normal fashion, and τ is set to $1/(2J_{\text{CH}})$. Selectivity is accomplished by choosing different θ values.

individual subspectra of the CH_n systems. The θ values used in the 2D DEPT work (55,56) were 45° , 90° and 135° . Another set of θ values 30° , 90° and 150° facilitates easier manipulation of the 2D data (57).

In order to illustrate the application of the simulation system to the analysis of a selective 2D shift correlation experiment, computations were carried out for CH , CH_2 and CH_3 systems. The input pulse sequences and outputs are given in Figures 17-19. The CH case will be used to illustrate the mechanism of shift correlation.

The calculations have been carried out for $\theta = 45^\circ$. The density operator for the CH system is represented in the simple product basis, as in Equation [4-1]. The initial proton 90° pulse creates transverse proton magnetizations which precess during the evolution period T_1 . This introduces a frequency labelling of the proton magnetization. The carbon 180° pulse at the midpoint of the T_1 period serves to eliminate the effects of carbon-proton coupling on the proton magnetizations. The density matrix at the end of the T_1 period is given by (Figure 17)

INPUT FOR 2D SELECTIVE DEPT EXPT ON C-H SYSTEM

```

COMM 2D SELECTIVE DEPT EXPERIMENT ON C-H SYSTEM
SPIN11S1
SET PULSC 45.0
PULSSA+X
PRECT1
PULSIB+X
PRECT1
WRDM
PRECD1
SUBSD1=1/( 2J)
PULSSB+X
PULSIA+X
PRECD1
SUBSD1=1/( 2J)
PULSSC+Y
PULSIB+X
PRECD2
SUBSD2=1/( 2J)
DCPLS T2
MEASIXY0
STOP

```

OUTPUT FOR 2D SELECTIVE DEPT EXPT ON C-H SYSTEMDensity Matrix After T1 Evolution Period

```

DM ( 1, 1) = +( -2.500, 0.0 )
DM ( 1, 3) = +( 0.0 , 50.000)*EXPI(2*PI*( 2.00 VS ) *T1 )
DM ( 2, 2) = +( 2.500, 0.0 )
DM ( 2, 4) = +( 0.0 , 50.000)*EXPI(2*PI*( 2.00 VS ) *T1 )
DM ( 3, 3) = +( -2.500, 0.0 )
DM ( 4, 4) = +( 2.500, 0.0 )

```

Carbon-13 Signals During Decoupled Acquisition

```

SIGNAL = +( 0.000, 3.536)*EXPI(2*PI*( 1.00 VI ) *T2 )
              *EXPI(2*PI*( -1.00 VI ) *D1 )
              *EXPI(2*PI*( 1.00 VI ) *D2 )

          +( -35.355, -0.000)*EXPI(2*PI*( 2.00 VS ) *T1 )
              *EXPI(2*PI*( 1.00 VI ) *T2 )
              *EXPI(2*PI*( -1.00 VI ) *D1 )
              *EXPI(2*PI*( 1.00 VI ) *D2 )

          +( -35.355, -0.000)*EXPI(2*PI*( -2.00 VS ) *T1 )
              *EXPI(2*PI*( 1.00 VI ) *T2 )
              *EXPI(2*PI*( -1.00 VI ) *D1 )
              *EXPI(2*PI*( 1.00 VI ) *D2 )

```

Figure 17. Input data and output from the simulation of CH selective shift correlation experiment. The θ pulse (pulse C) has been set to 45° .

INPUT FOR 2D SELECTIVE DEPT EXPT ON C-H2 SYSTEM

```

COMM 2D SELECTIVE DEPT EXPERIMENT ON C-H2 SYSTEM
SPIN11S2
SET PULSC 45.0
PULSSA+X
PRECT1
PULSIB+X
PRECT1
WRDM
PRECD1
SUBSD1=1/( 2J)
PULSSB+X
PULSIA+X
PRECD1
SUBSD1=1/( 2J)
PULSSC+Y
PULSIB+X
PRECD2
SUBSD2=1/( 2J)
DCPLS T2
MEASIXY0
STOP

```

OUTPUT FOR 2D SELECTIVE DEPT EXPT ON C-H2 SYSTEMDensity Matrix After T1 Evolution Period

```

DM ( 1, 1) = +( -2.500, 0.0 )
DM ( 1, 3) = +( 0.0 , 70.711)*EXPI(2*PI*( 2.00 VS )=T1
DM ( 2, 2) = +( 2.500, 0.0 )
DM ( 2, 4) = +( 0.0 , 70.711)*EXPI(2*PI*( 2.00 VS )=T1
DM ( 3, 3) = +( -2.500, 0.0 )
DM ( 3, 5) = +( 0.0 , 70.711)*EXPI(2*PI*( 2.00 VS )=T1
DM ( 4, 4) = +( 2.500, 0.0 )
DM ( 4, 6) = +( 0.0 , 70.711)*EXPI(2*PI*( 2.00 VS )=T1
DM ( 5, 5) = +( -2.500, 0.0 )
DM ( 6, 6) = +( 2.500, 0.0 )
DM ( 7, 7) = +( -2.500, 0.0 )
DM ( 8, 8) = +( 2.500, 0.0 )

```

Carbon-13 Signals During Decoupled Acquisition

```

SIGNAL = +( 0.000, 5.000)*EXPI(2*PI*( 1.00 v; )=T2
          *EXPI(2*PI*( -1.00 vI )=D1
          *EXPI(2*PI*( 1.00 vI )=D2
          +(-100.000, -0.000)*EXPI(2*PI*( 2.00 VS )=T1
          *EXPI(2*PI*( 1.00 vI )=T2
          *EXPI(2*PI*( -1.00 vI )=D1
          *EXPI(2*PI*( 1.00 vI )=D2
          +(-100.000, -0.000)*EXPI(2*PI*( -2.00 VS )=T1
          *EXPI(2*PI*( 1.00 vI )=T2
          *EXPI(2*PI*( -1.00 vI )=D1
          *EXPI(2*PI*( 1.00 vI )=D2

```

Figure 18. Input data and output from the simulation of CH_2 selective shift correlation experiment. The θ pulse (pulse C) has been set to 45° .

INPUT FOR 2D SELECTIVE DEPT EXPT ON C-H3 SYSTEM

```

COMM 2D SELECTIVE DEPT EXPERIMENT ON C-H3 SYSTEM
SPIN1153
SET PULSC 45.0
PULSSA+X
PRECT1
PULS1B+X
PRECT1
WRDM
PRECD1
SUBSD1=1/( 2J)
PULSSB+X
PULS1A+X
PRECD1
SUBSD1=1/( 2J)
PULSSC+Y
PULS1B+X
PRECD2
SUBSD2=1/( 2J)
DCPLS T2
ME&SIXYO
STOP

```

OUTPUT FOR 2D SELECTIVE EXPT ON C-H3 SYSTEM

Density Matrix After T1 Evolution Period

```

DM ( 1, 1) = +(-2.500, 0.0 )
DM ( 1, 3) = + ( 0.0 , 86.602)=EXP1(2=P1=( 2.00 VS )=T1 )
DM ( 2, 2) = + ( 2.500, 0.0 )
DM ( 2, 4) = + ( 0.0 , 86.602)=EXP1(2=P1=( 2.00 VS )=T1 )
DM ( 3, 3) = +(-2.500, 0.0 )
DM ( 3, 5) = + ( 0.0 , 100.000)=EXP1(2=P1=( 2.00 VS )=T1 )
DM ( 4, 4) = + ( 2.500, 0.0 )
DM ( 4, 6) = + ( 0.0 , 100.000)=EXP1(2=P1=( 2.00 VS )=T1 )
DM ( 5, 5) = +(-2.500, 0.0 )
DM ( 5, 7) = + ( 0.0 , 86.602)=EXP1(2=P1=( 2.00 VS )=T1 )
DM ( 6, 6) = + ( 2.500, 0.0 )
DM ( 6, 8) = + ( 0.0 , 86.602)=EXP1(2=P1=( 2.00 VS )=T1 )
DM ( 7, 7) = +(-2.500, 0.0 )
DM ( 8, 8) = + ( 2.500, 0.0 )
DM ( 9, 9) = +(-2.500, 0.0 )
DM ( 9, 11) = + ( 0.0 , -50.000)=EXP1(2=P1=( 2.00 VS )=T1 )
DM ( 10, 10) = + ( 2.500, 0.0 )
DM ( 10, 12) = + ( 0.0 , -50.000)=EXP1(2=P1=( 2.00 VS )=T1 )
DM ( 11, 11) = +(-2.500, 0.0 )
DM ( 12, 12) = + ( 2.500, 0.0 )
DM ( 13, 13) = +(-2.500, 0.0 )
DM ( 13, 15) = + ( 0.0 , 50.000)=EXP1(2=P1=( 2.00 VS )=T1 )
DM ( 14, 14) = + ( 2.500, 0.0 )
DM ( 14, 16) = + ( 0.0 , 50.000)=EXP1(2=P1=( 2.00 VS )=T1 )
DM ( 15, 15) = +(-2.500, 0.0 )
DM ( 16, 16) = + ( 2.500, 0.0 )

```

Carbon-13 Signals During Decoupled Acquisition

```

SIGNAL = +(-212.131, 0.000)=EXP1(2=P1=( 2.00 VS )=T1 )
          =EXP1(2=P1=( 1.00 V1 )=T2 )
          =EXP1(2=P1=( -1.00 V1 )=D1 )
          =EXP1(2=P1=( 1.00 V1 )=D2 )
          +(-212.131, 0.000)=EXP1(2=P1=( -2.00 VS )=T1 )
          =EXP1(2=P1=( 1.00 V1 )=T2 )
          =EXP1(2=P1=( -1.00 V1 )=D1 )
          =EXP1(2=P1=( 1.00 V1 )=D2 )
          +( 0.000, 7.071)=EXP1(2=P1=( 1.00 V1 )=T2 )
          =EXP1(2=P1=( -1.00 V1 )=D1 )
          =EXP1(2=P1=( 1.00 V1 )=D2 )

```

Figure 19. Input data and output from the simulation of CH_3 selective shift correlation experiment. The θ pulse (pulse C) has been set to 45° .

$$\tilde{\rho}(2T_1) = (1/2) \begin{bmatrix} 0 & a & b & 0 \\ a^* & 0 & 0 & b \\ b^* & 0 & 0 & a \\ 0 & b^* & a^* & 0 \end{bmatrix}, \quad [4-11]$$

where $a = -i\delta$ and $b = i\Delta \exp\{2\pi i \text{ VS } T_1\}$. It should be noted that the density matrix elements ρ_{13} and ρ_{24} which correspond to proton transverse magnetizations are frequency labelled in T_1 . Further, the evolution of the density matrix is similar to that in the DEPT pulse sequence described in Section IV.2.a. The proton-shift labelled magnetizations are transferred to the multiple-quantum coherence levels by the carbon 90° pulse. They are then converted to observable carbon magnetization by the proton θ pulse. The chemical shift offsets during the precession periods D_1 , D_2 , are refocussed to yield carbon signals free of intensity and phase distortions. The carbon signals observed under proton noise decoupling is given by (Figure 17)

$$\begin{aligned} \text{Signal} = & (\Delta/\sqrt{2}) \cos\{2\pi \text{ VS } T_1\} \exp\{2\pi i \text{ VI } T_2\} + \\ & (\delta/\sqrt{2}) \exp\{2\pi i \text{ VI } T_2\}, \end{aligned} \quad [4-12]$$

after recognizing that $D1 = D2$. Double Fourier transformation of this signal with respect to $T1$ and $T2$ yields the 2D spectrum.

It should be noted that in Equation [4-12], there is no quadrature detection in the $T1$ time period and hence in its frequency counterpart, the ν_1 dimension. Lack of quadrature detection in $T1$, dictates that the proton carrier frequency be placed at one end of the proton spectral width for distinction of plus and minus frequencies. This is inefficient in that the ν_1 spectral width is doubled, leading to the situation where twice the number of $T1$ values are required to achieve the same resolution achieved using a quadrature detection method. A phase cycling sequence for introducing quadrature detection in $T1$ has been worked out using the simulation program and is given in Figure 20. The carbon signal at the end of this 4-phase cycle sequence is given by (Figure 20)

$$\text{Signal} = (\Delta/2\sqrt{2}) \exp\{2\pi i \text{ VS } T1\} \exp\{2\pi i \text{ VI } T2\} . \quad [4-13]$$

Another interesting feature of the signal in Equation [4-13] is the absence of carbon Boltzmann signals. The carbon Boltzmann signals are nulled by cycling the first 90° carbon pulse through all four phases of the rotating

INPUT FOR 2D SELECTIVE DEPT EXPT WITH QUADRATURE DETECTION

COMM QUADRATURE DETECTION IN T1 DOMAIN

```
SPIN11S1
SET PULSC 45.0
PHASECYCLE 4
PULSSA+XSA+XSA+XSA+X
PRECT1
PULSIB+XIB+XIB+XIB+X
PRECT1
PRECD1
SUBSD1=1/( 2J)
PULSSB+XSB+XSB+XSB+X
PULSIA+XIA+YIA-XIA-Y
PRECD1
SUBSD1=1/( 2J)
PULSSC+YSC-XSC-YSC+X
PULSIB+XIB+XIB+XIB+X
PRECD2
SUBSD2=1/( 2J)
DCPLS T2
MEASIXYOIXYOIXYOIXYO
PHASECYCLE 4
STOP
```

OUTPUT FOR 2D DEPT EXPT WITH QUADRATURE DETECTION IN T1

Carbon-13 Signals (Decoupled) After 4-Phasecycles

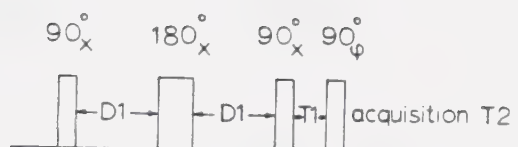
```
SIGNAL =      +(-141.421, -0.000)*EXPI(2*PI*( 2.00 VS      )*T1 )
               *EXPI(2*PI*(      1.00 VI      )*T2 )
               *EXPI(2*PI*(      -1.00 VI      )*D1 )
               *EXPI(2*PI*(      1.00 VI      )*D2 )
```

Figure 20. Input data and output from the 4-phase cycle CH selective shift correlation experiment. The signal exhibits quadrature phase in T1 domain.

frame. The phase of the second 90° proton pulse is rotated in the same direction but with a 90° relative phase shift from the carbon pulse. This ensures that only the transferred polarization signals are detected by the carbon receiver. This phase cycling also effects quadrature detection in ν_1 (Figure 20).

c. INADEQUATE Experiment

The INADEQUATE experiment has been developed to observe natural abundance ^{13}C - ^{13}C couplings without interference from the much more intense resonance due to the corresponding ^{13}C - ^{12}C fragments (58). This sequence takes advantage of the phase properties of multiple-quantum coherences. Variations of the basic INADEQUATE sequence have been employed in the observation of ^{13}C - ^{13}C couplings with enhanced sensitivity (62); in a two dimensional version for easier interpretation of spectra (63); for observation of long range ^{13}C - ^{13}C couplings (64); and for tracing out the carbon skeleton in a molecule (58). The main difficulty in identifying the weak ^{13}C - ^{13}C satellite lines in normal carbon spectra stems from the presence of many other weak signals due to spinning side bands, incomplete proton decoupling and sample impurities (58). The basic INADEQUATE pulse sequence is shown in Figure 21 and contains the minimum



Cycle	Read Pulse (φ)	Receiver
1	+x	$M_x + iM_y$
2	+y	$-M_y + iM_x$

INADEQUATE PULSE INPUT FOR C-C SYSTEM

```

HOMO
SPIN11S1
WRDM
PULSSA+X
WRDM
PRECD1
PULSSB+X
PRECD1
SUBSD1=1/( 4J)
WRDM
PULSSA+X
WRDM
PRECT1
WRDM
PHASECYCLE 2
PULSSA+XSA+Y
PRECT2
WRDM
MEASSXYOSXY1
PHASECYCLE 2
STOP
  
```

Figure 21. Pulse sequence and input data for simulation of the INADEQUATE experiment on ^{13}C - ^{13}C fragment.

phase cycling required to remove the strong resonances from molecules which contain only a single ^{13}C nucleus. More complicated phase cycles are often used to correct for pulse imperfections and other experimental problems (62).

In this section, the simulation of the INADEQUATE sequence applied to a homonuclear IIS1 system (a ^{13}C - ^{13}C fragment), to the S spins of a heteronuclear IIS1 system (a ^{13}C - ^{12}C fragment), and to a homonuclear IIS2 system (a ^{13}C - ^{13}C - ^{13}C fragment in an isotopically enriched molecule) are described.

The input to the simulation program to perform the INADEQUATE sequence on the IIS1 homonuclear system is shown in Figure 21. The output from the simulation program is given in Figure 22. The initial density matrix for the homonuclear IIS1 system (Figure 22) can be written as

$$\rho(0) = (1/2) \begin{bmatrix} 2\Delta & 0 & 0 & 0 \\ 0 & 0 & 0 & 0 \\ 0 & 0 & 0 & 0 \\ 0 & 0 & 0 & -2\Delta \end{bmatrix} . \quad [4-14]$$

The initial $90^\circ(+x)$ pulse puts all of the magnetization into the transverse plane and the four components ρ_{12} , ρ_{34} , ρ_{13} and ρ_{24} are proportional to the complex

INADEQUATE SEQUENCE FOR C-C SYSTEMInitial Density Matrix

```
DM ( 1, 1) = +( 100.000, 0.0 )
DM ( 2, 2) = +( 0.0 , 0.0 )
DM ( 3, 3) = +( 0.0 , 0.0 )
DM ( 4, 4) = +(-100.000, 0.0 )
```

Density Matrix After First 90 Pulse

```
DM ( 1, 2) = +( 0.0 , 50.000)
DM ( 1, 3) = +( 0.0 , 50.000)
DM ( 2, 4) = +( 0.0 , 50.000)
DM ( 3, 4) = +( 0.0 , 50.000)
```

Density Matrix After Second 1/(4J) Precession Period

```
DM ( 1, 2) = +( 50.000, -0.000)
DM ( 1, 3) = +( 50.000, -0.000)
DM ( 2, 4) = +(-50.000, -0.000)
DM ( 3, 4) = +(-50.000, -0.000)
```

Density Matrix After Second 90 Pulse

```
DM ( 1, 4) = +( 0.0 , 100.000)
```

Density Matrix After Precession Period T1

```
DM ( 1, 4) = +( 0.0 , 100.000)*EXP1(2*PI*( 1.00 VS 1.00 V1 )*T1)
```

D.M. During Acquisition, After Third 90 Pulse (+x ; Phasecycle 1)

```
DM ( 1, 1) = +( 50.000, 0.0 ) * SIN(2*PI*( 1.00 VS 1.00 V1 )*T1)
DM ( 1, 2) = +( -50.000, 0.0 ) * COS(2*PI*( 1.00 VS 1.00 V1 )*T1)
DM ( 1, 3) = +( -50.000, 0.0 ) * EXP1(2*PI*( 1.00 VS 1.00 V1 )*T2)
DM ( 1, 4) = +( -50.000, 0.0 ) * COS(2*PI*( 1.00 VS 1.00 V1 )*T1)
DM ( 2, 2) = +( -50.000, 0.0 ) * SIN(2*PI*( 1.00 VS 1.00 V1 )*T1)
DM ( 2, 3) = +( -50.000, 0.0 ) * EXP1(2*PI*( 1.00 VS 1.00 V1 )*T2)
DM ( 2, 4) = +( 50.000, 0.0 ) * COS(2*PI*( 1.00 VS 1.00 V1 )*T1)
DM ( 3, 3) = +( -50.000, 0.0 ) * SIN(2*PI*( 1.00 VS 1.00 V1 )*T1)
DM ( 3, 4) = +( 50.000, 0.0 ) * EXP1(2*PI*( 1.00 VS 1.00 V1 )*T2)
DM ( 4, 4) = +( 50.000, 0.0 ) * SIN(2*PI*( 1.00 VS 1.00 V1 )*T1)
```

D.M. During Acquisition, After Third 90 Pulse (+y ; Phasecycle 2)

```
DM ( 1, 1) = +( -50.000, 0.0 ) * SIN(2*PI*( 1.00 VS 1.00 V1 )*T1)
DM ( 1, 2) = +( 0.0 , 50.000) * COS(2*PI*( 1.00 VS 1.00 V1 )*T1)
DM ( 1, 3) = +( 0.0 , 50.000) * EXP1(2*PI*( 1.00 VS 1.00 V1 )*T2)
DM ( 1, 4) = +( -50.000, 0.0 ) * SIN(2*PI*( 1.00 VS 1.00 V1 )*T1)
DM ( 2, 2) = +( 50.000, 0.0 ) * SIN(2*PI*( 1.00 VS 1.00 V1 )*T1)
DM ( 2, 3) = +( 50.000, 0.0 ) * EXP1(2*PI*( 1.00 VS 1.00 V1 )*T2)
DM ( 2, 4) = +( 0.0 , -50.000) * COS(2*PI*( 1.00 VS 1.00 V1 )*T1)
DM ( 3, 3) = +( 50.000, 0.0 ) * SIN(2*PI*( 1.00 VS 1.00 V1 )*T1)
DM ( 3, 4) = +( 0.0 , -50.000) * EXP1(2*PI*( 1.00 VS 1.00 V1 )*T2)
DM ( 4, 4) = +( -50.000, 0.0 ) * SIN(2*PI*( 1.00 VS 1.00 V1 )*T1)
```

Carbon-13 Signals During Acquisition

```
SIGNAL = +(-100.000, 0.0 ) * COS(2*PI*( 1.00 VS 1.00 V1 )*T1)
          *EXP1(2*PI*( 1.00 VS 1.00 V1 )*T2)
          +( 100.000, 0.0 ) * COS(2*PI*( 1.00 VS 1.00 V1 )*T1)
          *EXP1(2*PI*( 1.00 VS 1.00 V1 )*T2)
          +( 100.000, 0.0 ) * COS(2*PI*( 1.00 VS 1.00 V1 )*T1)
          *EXP1(2*PI*( 1.00 VS 1.00 V1 )*T2)
          +(-100.000, 0.0 ) * COS(2*PI*( 1.00 VS 1.00 V1 )*T1)
          *EXP1(2*PI*( 1.00 VS 1.00 V1 )*T2)
```

Figure 22. Output data from simulation of INADEQUATE experiment on ^{13}C - ^{13}C fragment.

magnetizations associated with the resonances at $\nu_I + J/2$, $\nu_I - J/2$, $\nu_S + J/2$ and $\nu_S - J/2$ respectively. During the first precession period, these magnetization components dephase and if the duration of the precession is exactly $1/(4J)$, phase differences of 90° between the $\nu_I - J/2$ and $\nu_I + J/2$ magnetization vectors and between the $\nu_S - J/2$ and $\nu_S + J/2$ vectors are built up. The 180° pulse is applied to cancel the phase shifts due to resonance offsets which build up during the first precession period by refocussing them during the second precession period. Thus, at the end of the second precession, the magnetizations associated with the $\nu_I - J/2$ and $\nu_S - J/2$ resonances will lie along the $-x$ axis of the rotating frame and the magnetizations associated with the $\nu_I + J/2$ and $\nu_S + J/2$ resonances will lie along the $+x$ axes. The $90^\circ(+x)$ pulse causes all of the magnetizations to be transformed into the double-quantum coherence ρ_{14} which is modulated at frequency $\nu_I + \nu_S$. During the T_1 delay, the double quantum coherence acquires a phase shift of $2\pi(\nu_I + \nu_S)T_1$. The density matrix at this point, is given by (Figure 22)

$$\tilde{\rho}(2D_1+T_1) = (1/2) \begin{bmatrix} 0 & 0 & 0 & a \\ 0 & 0 & 0 & 0 \\ 0 & 0 & 0 & 0 \\ a^* & 0 & 0 & 0 \end{bmatrix}, \quad [4-15]$$

where $a = 2i\Delta \exp\{2\pi i(VS+VI)T_1\}$. The $90^\circ(\phi)$ pulse converts most of the double-quantum coherence back to observable magnetization. For $\phi = +x$, the $VI + J/2$ and $VS + J/2$ magnetizations lie along the $-x$ direction (ignoring the small phase shifts $2\pi(VS+VI)T_1$) and the $VI - J/2$ and $VS - J/2$ magnetizations lie along the $+x$ direction. For $\phi = +y$, the $VI + J/2$ and $VS + J/2$ magnetizations lie along the $+y$ direction and the $VI - J/2$ and $VS - J/2$ magnetizations lie along the $-y$ direction. The phase of the detector is chosen to measure $M_x + iM_y$ for $\phi = +x$ and $-M_y + iM_x$ for $\phi = -y$, which yields 1:-1 intensity patterns at $VI \pm J/2$ and at $VS \pm J/2$ in the Fourier transformed spectrum.

The input to the simulation program for the INADEQUATE sequence on the S spins of an IISl system is similar to that for the homonuclear IISl system given in Figure 21, but the HOMO and SUBS commands are deleted. The simulation results for this case are given in Figure 23. In this case, all pulses are applied only to the S spin so that first $90^\circ(+x)$ pulse simply generates transverse magnetization components at frequencies $VS + J/2$ and $VS - J/2$, associated with the density matrix elements ρ_{13} and ρ_{24} respectively. Here J represents the coupling of the S spin (^{13}C) to a heteronucleus (^1H), not

INADEQUATE SEQUENCE ON HETERO NUCLEAR 1 S SYSTEMInitial Density Matrix

```
DM ( 1, 1) = +( 52.500, 0.0 )
DM ( 2, 2) = +( 47.500, 0.0 )
DM ( 3, 3) = +( -47.500, 0.0 )
DM ( 4, 4) = +( -52.500, 0.0 )
```

Density Matrix After First 90 Pulse

```
DM ( 1, 1) = +( 2.500, 0.0 )
DM ( 1, 3) = +( 0.0, 50.000)
DM ( 2, 2) = +( -2.500, 0.0 )
DM ( 2, 4) = +( 0.0, 50.000)
DM ( 3, 3) = +( 2.500, 0.0 )
DM ( 4, 4) = +( -2.500, 0.0 )
```

Density Matrix After Second D1 Precession Period

```
DM ( 1, 1) = +( 2.500, 0.0 )
DM ( 1, 3) = +( 0.0, -50.000)
DM ( 2, 2) = +( -2.500, 0.0 )
DM ( 2, 4) = +( 0.0, -50.000)
DM ( 3, 3) = +( 2.500, 0.0 )
DM ( 4, 4) = +( -2.500, 0.0 )
```

Density Matrix After Second 90 Pulse

```
DM ( 1, 1) = +( 52.500, 0.0 )
DM ( 2, 2) = +( 47.500, 0.0 )
DM ( 3, 3) = +( -47.500, 0.0 )
DM ( 4, 4) = +( -52.500, 0.0 )
```

Density Matrix After Precession Period T1

```
DM ( 1, 1) = +( 52.500, 0.0 )
DM ( 2, 2) = +( 47.500, 0.0 )
DM ( 3, 3) = +( -47.500, 0.0 )
DM ( 4, 4) = +( -52.500, 0.0 )
```

D.M. During Acquisition, After 90(+X) Pulse (Phasecycle 1)

```
DM ( 1, 1) = +( 2.500, 0.0 )
DM ( 1, 3) = +( 0.0, 50.000)*EXP(2*PI*( 1.00 VS 0.50 J)*T2)
DM ( 2, 2) = +( -2.500, 0.0 )
DM ( 2, 4) = +( 0.0, 50.000)*EXP(2*PI*( 1.00 VS -0.50 J)*T2)
DM ( 3, 3) = +( 2.500, 0.0 )
DM ( 4, 4) = +( -2.500, 0.0 )
```

D.M. During Acquisition, After 90(+Y) Pulse (Phasecycle 2)

```
DM ( 1, 1) = +( 2.500, 0.0 )
DM ( 1, 3) = +( -50.000, 0.0 )*EXP(2*PI*( 1.00 VS 0.50 J)*T2)
DM ( 2, 2) = +( -2.500, 0.0 )
DM ( 2, 4) = +( -50.000, 0.0 )*EXP(2*PI*( 1.00 VS -0.50 J)*T2)
DM ( 3, 3) = +( 2.500, 0.0 )
DM ( 4, 4) = +( -2.500, 0.0 )
```

Carbon-13 Signals During Acquisition

RESULTANT SIGNAL IS ZERO

Figure 23. Output data from simulation of INADEQUATE experiment on ^{13}C - ^{12}C fragment.

a ^{13}C - ^{13}C coupling. The 180° pulse causes the phase shifts which build up on ρ_{13} and ρ_{24} during the first precession period to be refocussed in the second period and the magnetization vectors for the two components both lie along the $-y$ axis. Hence the second $90^\circ(+x)$ pulse rotates these components to the $+z$ axis and the density matrix is identical to its initial thermal equilibrium value. It does not change during the T_1 interval. The $90^\circ(\phi)$ pulse converts the carbon z magnetization into components along the $+y$ (for $\phi = +x$) or $-x$ (for $\phi = +y$) directions. With detector phases set to measure $M_x + iM_y$ for $\phi = +x$ and $-M_y + iM_x$ for $\phi = +y$, it is clear that the sum of the two acquisitions will be zero as the output in Figure 23 shows.

It is interesting to consider the simulation of the INADEQUATE sequence on an ILS2 homonuclear system in order to determine the behaviour of a molecule containing three coupled ^{13}C nuclei with this pulse sequence. This example is relevant in ^{13}C studies on isotopically enriched molecules. The output of the simulation for this case is given in Figure 24. The components of the carbon FID with frequencies $\text{VI} - J$, VI , $\text{VI} + J$, $\text{VS} - J/2$ and $\text{VS} + J/2$ have different phases so the Fourier transformed spectrum will consist of both dispersive and absorptive components. If we assume that the delay T_1 is very short (in practice ~ 10

INADEQUATE SEQUENCE ON THREE COUPLED CARBON (C-C-C) SYSTEM

Carbon-13 Signals During Acquisition (from 2 phasecycles)

```

SIGNAL =  +( -25.000,  0.0  ) * COS(2*PI*( 1.00 VS  1.00 VI  0.50 J)*T1)
              *EXPI(2*PI*(
              +(  0.0  , -25.000) * COS(2*PI*( 2.00 VS  1.00 VI  1.00 J)*T2)
              *EXPI(2*PI*(
              +( 25.000,  0.0  ) * COS(2*PI*( -1.00 VS -1.00 VI  0.50 J)*T1)
              *EXPI(2*PI*(
              +(  0.0  , -25.000) * COS(2*PI*( 2.00 VS  1.00 VI -1.00 J)*T2)
              *EXPI(2*PI*(
              +(-25.000,  0.0  ) * COS(2*PI*( 1.00 VS  1.00 VI -0.50 J)*T1)
              *EXPI(2*PI*(
              +(  0.0  , -25.000) * COS(2*PI*( 2.00 VS  1.00 VI  1.00 J)*T2)
              *EXPI(2*PI*(
              +(-50.000,  0.0  ) * COS(2*PI*( -1.00 VS -1.00 VI -0.50 J)*T1)
              *EXPI(2*PI*(
              +(  0.0  , -25.000) * COS(2*PI*( 2.00 VS  1.00 VI  0.50 J)*T2)
              *EXPI(2*PI*(
              +(-50.000,  0.0  ) * COS(2*PI*( 1.00 VS  1.00 VI -0.50 J)*T1)
              *EXPI(2*PI*(
              +( 50.000,  0.0  ) * COS(2*PI*( -1.00 VS -1.00 VI -0.50 J)*T2)
              *EXPI(2*PI*(
              +( 50.000,  0.0  ) * COS(2*PI*( 1.00 VS  1.00 VI -0.50 J)*T1)
              *EXPI(2*PI*(
              +( 25.000,  0.0  ) * COS(2*PI*( -1.00 VS -1.00 VI -0.50 J)*T2)
              *EXPI(2*PI*(
              +(  0.0  , 50.000) * COS(2*PI*( 2.00 VS  1.00 VI  1.00 J)*T1)
              *EXPI(2*PI*(
              +(  0.0  , 50.000) * COS(2*PI*( 2.00 VS  1.00 VI -1.00 J)*T2)
              *EXPI(2*PI*(

```

Figure 24. Output data from simulation of the INADEQUATE experiment on ^{13}C - ^{13}C - ^{13}C fragment.

μs), the phase factors involving double quantum frequencies $V_S \pm V_I + J/2$ and $2V_S \pm J$ can be set to unity. Then, if the spectrum is phased so that the lines at $V_S - J$ and $V_S + J$ are absorptions with relative intensities 2:-2, the line at V_I will be purely dispersive and have relative intensity 1; while the lines at $V_I - J$ and $V_I + J$ will have absorptive components of intensity 1:-1, and dispersive components of magnitude $-1/2:-1/2$. It should be noted that the multiple-quantum signals arise from even-order coherence, i.e. in the case of IIS₂ system, from zero- and double-quantum coherences. The INADEQUATE signals for a molecule containing three ^{13}C nuclei are rather different from those for molecules with only two ^{13}C nuclei in that the phases of the various lines are significantly different.

d. Unexpected Effects of Spin Decoupling

Recently Levitt et al. (53) have demonstrated that unanticipated effects can be observed in certain experiments employing spin decoupling. They have studied the effect of heteronuclear decoupling applied to the S spins, on the resonance of another nuclear species I, in IS_n spin systems which are in arbitrary states at the start of the decoupling period. It was concluded that, even under strong decoupling the two spin systems, I and

S, do not behave independently. The multiplet components of I spin magnetization are affected by the rf perturbation to the S spin when the I multiplet components differ in magnitude or phase at the beginning of the decoupling period.

An analysis of the time evolution of the density operator $\hat{\rho}(t)$ during the decoupling period, was carried out by Levitt et al. (53), and has shown that the necessary conditions for the S spin decoupling field to affect the I spin expectation value $\langle Q \rangle$ are:

$$(1) \quad [\hat{H}_S, \hat{\rho}(0)] \neq 0$$

[4-16]

$$(2) \quad [\hat{H}_S, \hat{Q}] \neq 0 \quad ,$$

where \hat{H}_S is the S spin Hamiltonian during the decoupling period and $\hat{\rho}(0)$ is the density operator at the start of the decoupling period. The above conditions have been used to explain the effect of S spin decoupling on the I spin multiplet components (53). Consider the example of an IS system. When the I spin multiplets have the same phase, for example, a state obtained after a $90^\circ(+y)$ I pulse acting on an equilibrium system, $\hat{\rho}(0)$ is proportional to \hat{I}_x . If the system is then subjected to strong S spin decoupling, the effective S spin Hamiltonian \hat{H}_S in the S spin rotating frame is given by

$$\hat{H}_S = \omega_S \hat{S}_x .$$

\hat{H}_S does not affect the expectation value $\langle Q \rangle$ because $\hat{\rho}(0)$ commutes with \hat{H}_S . However, if the I spin multiplets are allowed to dephase for a time period, before the start of the decoupling, the magnetization components will develop a phase difference. At the start of the decoupling period (time $t = 0$), the density operator of the system will have a component which is proportional to $\hat{I}_x \hat{S}_z$. Now $\hat{\rho}(0)$ does not commute with \hat{H}_S and, as a consequence, the I spin multiplets are affected by the S spin decoupler.

This unexpected effect of spin decoupling has been demonstrated by Levitt et al. (53) using two variants of a 2D gated decoupling experiment. The pulse sequences are shown in Figure 25. The gated decoupler carbon J resolved experiment without proton decoupling during the observation period is shown in Figure 25A. The proton decoupler is turned on before the carbon 180° refocussing pulse in the evolution period. The other variant of this experiment, shown in Figure 25B, has the proton decoupler turned on after the carbon 180° pulse in the evolution period. It might, at first, be expected that both experiments would yield identical results. The pulse sequence in Figure 25A gives 1:1, 1:2:1, 1:3:3:1 multiplets on diagonals tilted by $\tan^{-1}(1/2)$ with respect

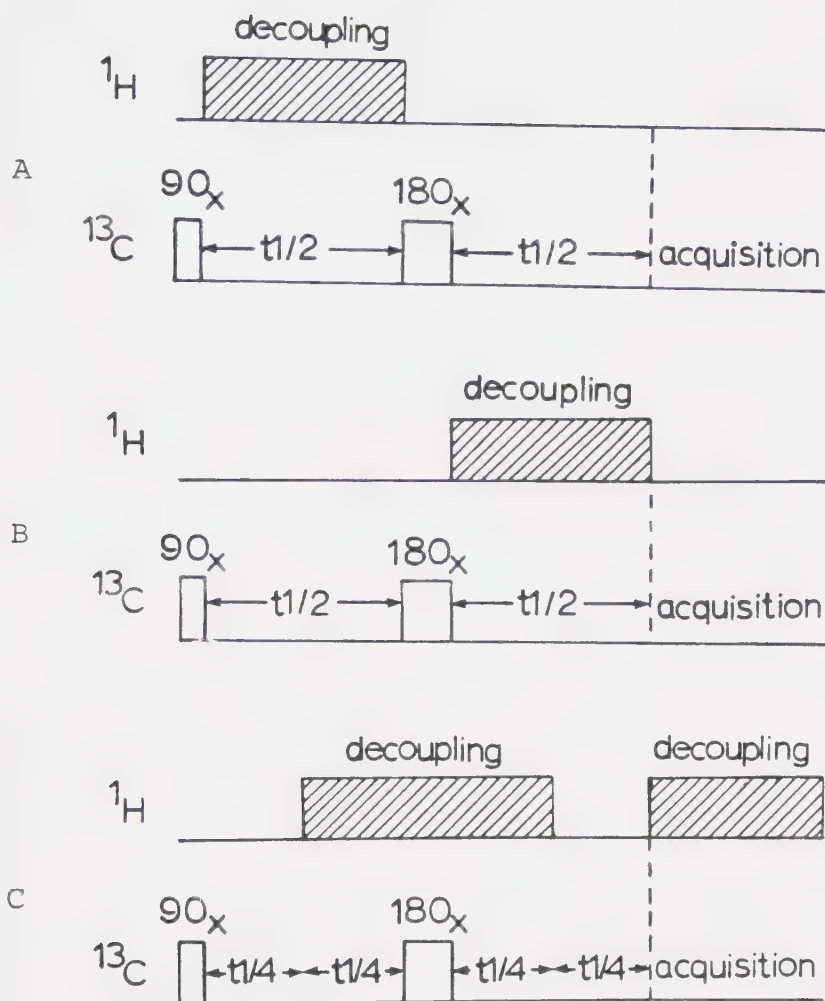


Figure 25. 2D gated decoupler ^{13}C J- δ resolved pulse sequences: (A) the decoupler is gated on during the first half of the evolution period t_1 ; (B) the decoupler is gated on during the second half; and (C) the decoupler is gated on in the middle of the evolution period t_1 .

to the ν_1 axis for CH, CH₂ and CH₃ groups respectively. With the sequence in Figure 25B, one obtains an $(n+1) \times (n+1)$ rectangular array of peaks for each CH_n group with ν_1 cross section intensities 1:1 and 1:1 for CH, 1:1:1, 1:4:1 and 1:1:1 for CH₂, and 1:1:1:1, 1:5:5:1, 1:5:5:1 and 1:1:1:1 for CH₃ with spherical decoupling.

In the following, the results of a density matrix analysis of the behaviour of all three spin systems using the pulse sequences in Figures 25A and 25B, carried out using the simulation program are reported. The simulation results for CH, CH₂ and CH₃ systems are given in Figures 26-29. A detailed description is presented for the CH₂ system below. The simulations were carried out with a special version of the decoupling subprogram which employs the spherical randomization decoupling procedure instead of the normal decoupling process.

For the CH₂ spin system at thermal equilibrium, the density matrix in the basis defined in Section II.4, is (Figures 27 and 28)

INPUT PULSE SEQUENCE FOR GATED-DECOUPLER 2D EXPERIMENTS

```

COMM  ILLUSIONS OF SPIN DECOUPLING  SEQUENCE A
SPIN11S1
PULS1A+X
DCPLS  T1
PULS1B+X
PRECT1
PRECT2
MEAS1XY0
NEXT
COMM  ILLUSIONS OF SPIN DECOUPLING  SEQUENCE B
SPIN11S1
PULS1A+X
PRECT1
PULS1B+X
DCPLS  T1
PRECT2
MEAS1XY0
STOP

```

OUTPUT FOR PULSE SEQUENCE A ON CH SYSTEM

Carbon-13 Signals During Acquisition

```

SIGNAL =      +(  0.0  ,  -2.500)*EXPI(2*PI*(
                                *EXPI(2*PI*(
                                1.00 VI      0.50 J  )*T1 )
                                0.50 J  )*T2 )
              +(  0.0  ,  -2.500)*EXPI(2*PI*(
                                *EXPI(2*PI*(
                                1.00 VI      -0.50 J  )*T1 )
                                -0.50 J  )*T2 )

```

OUTPUT FOR PULSE SEQUENCE B ON CH SYSTEM

Carbon-13 Signals During Acquisition

```

SIGNAL =      +(  0.0  ,  -1.250)*EXPI(2*PI*(
                                *EXPI(2*PI*(
                                1.00 VI      -0.50 J  )*T1 )
                                0.50 J  )*T2 )
              +(  0.0  ,  -1.250)*EXPI(2*PI*(
                                *EXPI(2*PI*(
                                1.00 VI      0.50 J  )*T1 )
                                0.50 J  )*T2 )
              +(  0.0  ,  -1.250)*EXPI(2*PI*(
                                *EXPI(2*PI*(
                                1.00 VI      -0.50 J  )*T1 )
                                -0.50 J  )*T2 )
              +(  0.0  ,  -1.250)*EXPI(2*PI*(
                                *EXPI(2*PI*(
                                1.00 VI      0.50 J  )*T1 )
                                -0.50 J  )*T2 )

```

Figure 26. Input data and output from simulation of gated decoupler pulse sequences A and B on CH system.

OUTPUT FOR GATED DECOUPLER SEQUENCE A ON CH₂ SYSTEM

Density Matrix After 90(+X) Carbon Pulse

```
DM ( 1, 1) = +( 100.000,  0.0 )
DM ( 1, 2) = +(   0.0 ,  2.500)
DM ( 2, 2) = +( 100.000,  0.0 )
DM ( 3, 4) = +(   0.0 ,  2.500)
DM ( 5, 5) = +(-100.000,  0.0 )
DM ( 5, 6) = +(   0.0 ,  2.500)
DM ( 6, 6) = +(-100.000,  0.0 )
DM ( 7, 8) = +(   0.0 ,  2.500)
```

Density Matrix After the Decoupling period

```
DM ( 1, 2) = +(   0.0 ,  2.500)*EXPI(2*PI*(      1.00 VI      )*T1 )
DM ( 3, 4) = +(   0.0 ,  2.500)*EXPI(2*PI*(      1.00 VI      )*T1 )
DM ( 5, 6) = +(   0.0 ,  2.500)*EXPI(2*PI*(      1.00 VI      )*T1 )
DM ( 7, 8) = +(   0.0 ,  2.500)*EXPI(2*PI*(      1.00 VI      )*T1 )
```

Carbon Signals During Acquisition

```
SIGNAL =      +(   0.0 , -2.500)*EXPI(2*PI*(      1.00 VI      1.00 J )*T1 )
               *EXPI(2*PI*(      1.00 VI      1.00 J )*T2 )
               +(   0.0 , -5.000)*EXPI(2*PI*(      1.00 VI      )*T2 )
               +(   0.0 , -2.500)*EXPI(2*PI*(      1.00 VI     -1.00 J )*T1 )
               *EXPI(2*PI*(      1.00 VI     -1.00 J )*T2 )
```

Figure 27. Output data from simulation of gated decoupler pulse sequence A on CH₂ system.

OUTPUT FOR GATED DECOUPLER SEQUENCE B ON CH₂ SYSTEM

Density Matrix Before the Decoupling Period

```
DM ( 1, 1) = +( 100.000, 0.0 )
DM ( 1, 2) = +( 0.0 , -2.500)*EXPI(2*PI*( -1.00 VI -1.00 J )*T1 )
DM ( 2, 2) = +( 100.000, 0.0 )
DM ( 3, 4) = +( 0.0 , -2.500)*EXPI(2*PI*( -1.00 VI )*T1 )
DM ( 5, 5) = +(-100.000, 0.0 )
DM ( 5, 6) = +( 0.0 , -2.500)*EXPI(2*PI*( -1.00 VI 1.00 J )*T1 )
DM ( 6, 6) = +(-100.000, 0.0 )
DM ( 7, 8) = +( 0.0 , -2.500)*EXPI(2*PI*( -1.00 VI )*T1 )
```

Density Matrix After the Decoupling Period

```
DM ( 1, 2) = +( 0.0 , -0.833)*EXPI(2*PI*( -1.00 J )*T1 )
              +( 0.0 , -0.833)
DM ( 3, 4) = +( 0.0 , -0.833)*EXPI(2*PI*( 1.00 J )*T1 )
              +( 0.0 , -0.833)*EXPI(2*PI*( -1.00 J )*T1 )
              +( 0.0 , -0.833)
DM ( 5, 6) = +( 0.0 , -0.833)*EXPI(2*PI*( 1.00 J )*T1 )
              +( 0.0 , -0.833)*EXPI(2*PI*( -1.00 J )*T1 )
              +( 0.0 , -0.833)
DM ( 7, 8) = +( 0.0 , -0.833)*EXPI(2*PI*( 1.00 J )*T1 )
              +( 0.0 , -2.500)
```

Carbon Signals During Acquisition

```
SIGNAL = +( 0.0 , -0.833)*EXPI(2*PI*( -1.00 J )*T1 )
              *EXPI(2*PI*( 1.00 VI 1.00 J )*T2 )
              +( 0.0 , -0.833)*EXPI(2*PI*( 1.00 VI 1.00 J )*T2 )
              +( 0.0 , -0.833)*EXPI(2*PI*( 1.00 VI 1.00 J )*T1 )
              *EXPI(2*PI*( 1.00 VI 1.00 J )*T2 )
              +( 0.0 , -0.833)*EXPI(2*PI*( 1.00 VI -1.00 J )*T1 )
              *EXPI(2*PI*( 1.00 VI )*T2 )
              +( 0.0 , -3.333)*EXPI(2*PI*( 1.00 VI )*T2 )
              +( 0.0 , -0.833)*EXPI(2*PI*( 1.00 VI 1.00 J )*T1 )
              *EXPI(2*PI*( 1.00 VI )*T2 )
              +( 0.0 , -0.833)*EXPI(2*PI*( 1.00 VI -1.00 J )*T1 )
              *EXPI(2*PI*( 1.00 VI -1.00 J )*T2 )
              +( 0.0 , -0.833)*EXPI(2*PI*( 1.00 VI -1.00 J )*T2 )
              +( 0.0 , -0.833)*EXPI(2*PI*( 1.00 VI 1.00 J )*T1 )
              *EXPI(2*PI*( 1.00 VI -1.00 J )*T2 )
```

Figure 28. Output data from simulation of gated decoupler pulse sequence B on CH₂ system.

OUTPUT FOR GATED DECOUPLER SEQUENCE A ON CH3 SYSTEM

Carbon Signals During Acquisition

SIGNAL =	+(0.0 , -2.500)*EXPI(2*PI*(1.00 VI	1.50 J)*T1)
	*EXPI(2*PI*(1.50 J)*T2)
	+(0.0 , -7.500)*EXPI(2*PI*(1.00 VI	0.50 J)*T1)
	*EXPI(2*PI*(0.50 J)*T2)
	+(0.0 , -7.500)*EXPI(2*PI*(1.00 VI	-0.50 J)*T1)
	*EXPI(2*PI*(-0.50 J)*T2)
	+(0.0 , -2.500)*EXPI(2*PI*(1.00 VI	-1.50 J)*T1)
	*EXPI(2*PI*(-1.50 J)*T2)

OUTPUT FOR GATED DECOUPLER SEQUENCE B ON CH3 SYSTEM

Carbon Signals During Acquisition

SIGNAL =	+(0.0 , -0.625)*EXPI(2*PI*(1.00 VI	-1.50 J)*T1)
	*EXPI(2*PI*(1.50 J)*T2)
	+(0.0 , -0.625)*EXPI(2*PI*(1.00 VI	-0.50 J)*T1)
	*EXPI(2*PI*(1.50 J)*T2)
	+(0.0 , -0.625)*EXPI(2*PI*(1.00 VI	0.50 J)*T1)
	*EXPI(2*PI*(1.50 J)*T2)
	+(0.0 , -0.625)*EXPI(2*PI*(1.00 VI	1.50 J)*T1)
	*EXPI(2*PI*(1.50 J)*T2)
	+(0.0 , -0.625)*EXPI(2*PI*(1.00 VI	-1.50 J)*T1)
	*EXPI(2*PI*(0.50 J)*T2)
	+(0.0 , -3.125)*EXPI(2*PI*(1.00 VI	-0.50 J)*T1)
	*EXPI(2*PI*(0.50 J)*T2)
	+(0.0 , -3.125)*EXPI(2*PI*(1.00 VI	0.50 J)*T1)
	*EXPI(2*PI*(0.50 J)*T2)
	+(0.0 , -0.625)*EXPI(2*PI*(1.00 VI	1.50 J)*T1)
	*EXPI(2*PI*(0.50 J)*T2)
	+(0.0 , -0.625)*EXPI(2*PI*(1.00 VI	-1.50 J)*T1)
	*EXPI(2*PI*(-0.50 J)*T2)
	+(0.0 , -3.125)*EXPI(2*PI*(1.00 VI	-0.50 J)*T1)
	*EXPI(2*PI*(-0.50 J)*T2)
	+(0.0 , -3.125)*EXPI(2*PI*(1.00 VI	0.50 J)*T1)
	*EXPI(2*PI*(-0.50 J)*T2)
	+(0.0 , -0.625)*EXPI(2*PI*(1.00 VI	1.50 J)*T1)
	*EXPI(2*PI*(-0.50 J)*T2)
	+(0.0 , -0.625)*EXPI(2*PI*(1.00 VI	-1.50 J)*T1)
	*EXPI(2*PI*(-1.50 J)*T2)
	+(0.0 , -0.625)*EXPI(2*PI*(1.00 VI	-0.50 J)*T1)
	*EXPI(2*PI*(-1.50 J)*T2)
	+(0.0 , -0.625)*EXPI(2*PI*(1.00 VI	0.50 J)*T1)
	*EXPI(2*PI*(-1.50 J)*T2)
	+(0.0 , -0.625)*EXPI(2*PI*(1.00 VI	1.50 J)*T1)
	*EXPI(2*PI*(-1.50 J)*T2)

Figure 29. Output data from simulation of gated decoupler pulse sequences A and B on CH₃ system.

$$\tilde{\rho}(0) = (1/2) \begin{bmatrix} 2\Delta+\delta & 0 & 0 & 0 & 0 & 0 & 0 & 0 \\ 0 & 2\Delta-\delta & 0 & 0 & 0 & 0 & 0 & 0 \\ 0 & 0 & \delta & 0 & 0 & 0 & 0 & 0 \\ 0 & 0 & 0 & -\delta & 0 & 0 & 0 & 0 \\ 0 & 0 & 0 & 0 & -2\Delta+\delta & 0 & 0 & 0 \\ 0 & 0 & 0 & 0 & 0 & -2\Delta-\delta & 0 & 0 \\ 0 & 0 & 0 & 0 & 0 & 0 & \delta & 0 \\ 0 & 0 & 0 & 0 & 0 & 0 & 0 & -\delta \end{bmatrix}, [4-17]$$

where Δ and δ have been set to 100 and 5 respectively in the simulation program. Here the I spin corresponds to the carbon and S spins correspond to protons. In both sequences A and B (shown in Figures 25A and 25B respectively), a $90^\circ(+x)$ carbon pulse is applied first, and the density matrix becomes (Figures 27 and 28)

$$\tilde{\rho}_{+}^{AB}(0) = (1/2) \begin{bmatrix} 2\Delta & i\delta & 0 & 0 & 0 & 0 & 0 & 0 \\ -i\delta & 2\Delta & 0 & 0 & 0 & 0 & 0 & 0 \\ 0 & 0 & 0 & i\delta & 0 & 0 & 0 & 0 \\ 0 & 0 & -i\delta & 0 & 0 & 0 & 0 & 0 \\ 0 & 0 & 0 & 0 & -2\Delta & i\delta & 0 & 0 \\ 0 & 0 & 0 & 0 & -i\delta & -2\Delta & 0 & 0 \\ 0 & 0 & 0 & 0 & 0 & 0 & 0 & i\delta \\ 0 & 0 & 0 & 0 & 0 & 0 & -i\delta & 0 \end{bmatrix}, [4-18]$$

where the superscripts A and B refer to the pulse sequences. In Sequence A, the proton decoupler is turned on immediately after the carbon pulse and, since all of the carbon multiplets are in phase at this point, it decouples the proton-carbon interactions during the period T_1 . Hence, at time T_1 , the density matrix (Figure 27) is

$$\tilde{\rho}^A(T_1) = (1/2) \begin{bmatrix} 0 & a^* & 0 & 0 & 0 & 0 & 0 & 0 \\ a & 0 & 0 & 0 & 0 & 0 & 0 & 0 \\ 0 & 0 & 0 & a^* & 0 & 0 & 0 & 0 \\ 0 & 0 & a & 0 & 0 & 0 & 0 & 0 \\ 0 & 0 & 0 & 0 & 0 & a^* & 0 & 0 \\ 0 & 0 & 0 & 0 & a & 0 & 0 & 0 \\ 0 & 0 & 0 & 0 & 0 & 0 & 0 & a^* \\ 0 & 0 & 0 & 0 & 0 & 0 & a & 0 \end{bmatrix}, \quad [4-19]$$

where $a = i\delta \exp\{2\pi i \nu_I T_1\}$. The 180° carbon pulse and subsequent delay period T_1 , refocusses the carbon chemical shifts but retains the modulation due to heteronuclear coupling to the protons. Carbon signals are then acquired in the absence of proton decoupling. The signals computed by the simulation program (Figure 27) yields the conventional 1:2:1 triplet at positions $(J, \nu_I + J)$, $(0, \nu_I)$, $(-J, \nu_I - J)$, where J represents the carbon-proton coupling constant. This result is in complete agreement with the reported experimental spectrum (53).

In the case of pulse sequence B (Figure 28), the carbon magnetization components develop phase differences during the evolution period T_1 . The 180° carbon pulse following the period T_1 interchanges the labels of the carbon magnetization components and the density matrix after the 180° pulse is given by (Figure 28)

$$\tilde{\rho}_B(T_1) = (1/2) \begin{bmatrix} 2\Delta & b & 0 & 0 & 0 & 0 & 0 & 0 \\ b^* & 2\Delta & 0 & 0 & 0 & 0 & 0 & 0 \\ 0 & 0 & 0 & c & 0 & 0 & 0 & 0 \\ 0 & 0 & c^* & 0 & 0 & 0 & 0 & 0 \\ 0 & 0 & 0 & 0 & -2\Delta & d & 0 & 0 \\ 0 & 0 & 0 & 0 & d^* & -2\Delta & 0 & 0 \\ 0 & 0 & 0 & 0 & 0 & 0 & 0 & c \\ 0 & 0 & 0 & 0 & 0 & 0 & c^* & 0 \end{bmatrix}, \quad [4-20]$$

where $b = -i\delta \exp\{2\pi i(-VI-J)T_1\}$, $c = -i\delta \exp\{2\pi i(-VI)T_1\}$, and $d = -i\delta \exp\{2\pi i(-VI+J)T_1\}$. It should be noted that the carbon magnetization components, corresponding to density matrix elements ρ_{12} , ρ_{34} , ρ_{56} and ρ_{78} have different phases. Proton decoupling is then applied during the next evolution period T_1 . The density matrix at the end of the decoupling period T_1 is given by (Figure 28)

$$\tilde{\rho}_B(2T1) = (1/2) \begin{bmatrix} 0 & e & 0 & 0 & 0 & 0 & 0 & 0 \\ e^* & 0 & 0 & 0 & 0 & 0 & 0 & 0 \\ 0 & 0 & 0 & e & 0 & 0 & 0 & 0 \\ 0 & 0 & e^* & 0 & 0 & 0 & 0 & 0 \\ 0 & 0 & 0 & 0 & 0 & e & 0 & 0 \\ 0 & 0 & 0 & 0 & e^* & 0 & 0 & 0 \\ 0 & 0 & 0 & 0 & 0 & 0 & 0 & f \\ 0 & 0 & 0 & 0 & 0 & 0 & f^* & 0 \end{bmatrix}, \quad [4-21]$$

where $e = (-i\delta/3)[\exp\{-2\pi i J T1\} + 1 + \exp\{2\pi i J T1\}]$ and $f = -i\delta$. Carbon signals in the absence of proton decoupler has been computed (Figure 28), which leads to a 3×3 array of peaks at positions $(J, VI+J)$, (J, VI) , $(J, VI-J)$; $(0, VI+J)$, $(0, VI)$, $(0, VI-J)$; $(-J, VI+J)$, $(-J, VI)$, $(-J, VI-J)$ with relative intensities 1:1:1:1:4:1:1:1:1. This 2D spectrum is again in agreement with experimental results reported (53).

If the proton decoupler is gated on during the acquisition period of either sequence A or B, the 2D correlation map will consist of 1:1, 1:2:1 and 1:3:3:1 patterns of peaks at the appropriate carbon chemical shift in ν_2 for CH, CH₂ and CH₃ groups respectively. The equivalence of sequences A and B when the decoupler is gated on during acquisition, might tempt one to conclude (incorrectly) that "illusions" of spin decoupling are observed only in coupled spectra.

If the decoupling period is placed in the center of the evolution period (Figure 25C) rather than at the beginning (sequence A) or end (sequence B), carbon signals acquired in the presence of proton decoupling will show effects of decoupling during the evolution period. Carbon signals are acquired in the presence of proton decoupler irradiation. The 2D contour map and the v_1 cross-sections obtained from 2-butanol (90% in CDCl_3) with the pulse sequence C are shown in Figure 30. The 2D map consists of a triplet for the CH group, a quintet for the CH_2 group and septets for the CH_3 group, with spacings between the lines equal to $J_{\text{CH}}/4$.

Density matrix analysis of the pulse sequence C applied on CH (IIS1), CH_2 (IIS2) and CH_3 (IIS3) systems are shown in Figures 31, 32 and 33 respectively. The spherical randomization decoupling procedure has been used for the simulation. A brief description of the CH results (from Figure 31) are given in the following.

For the CH spin system at thermal equilibrium, the density matrix in the basis defined in Section II.4, is (Figure 31)

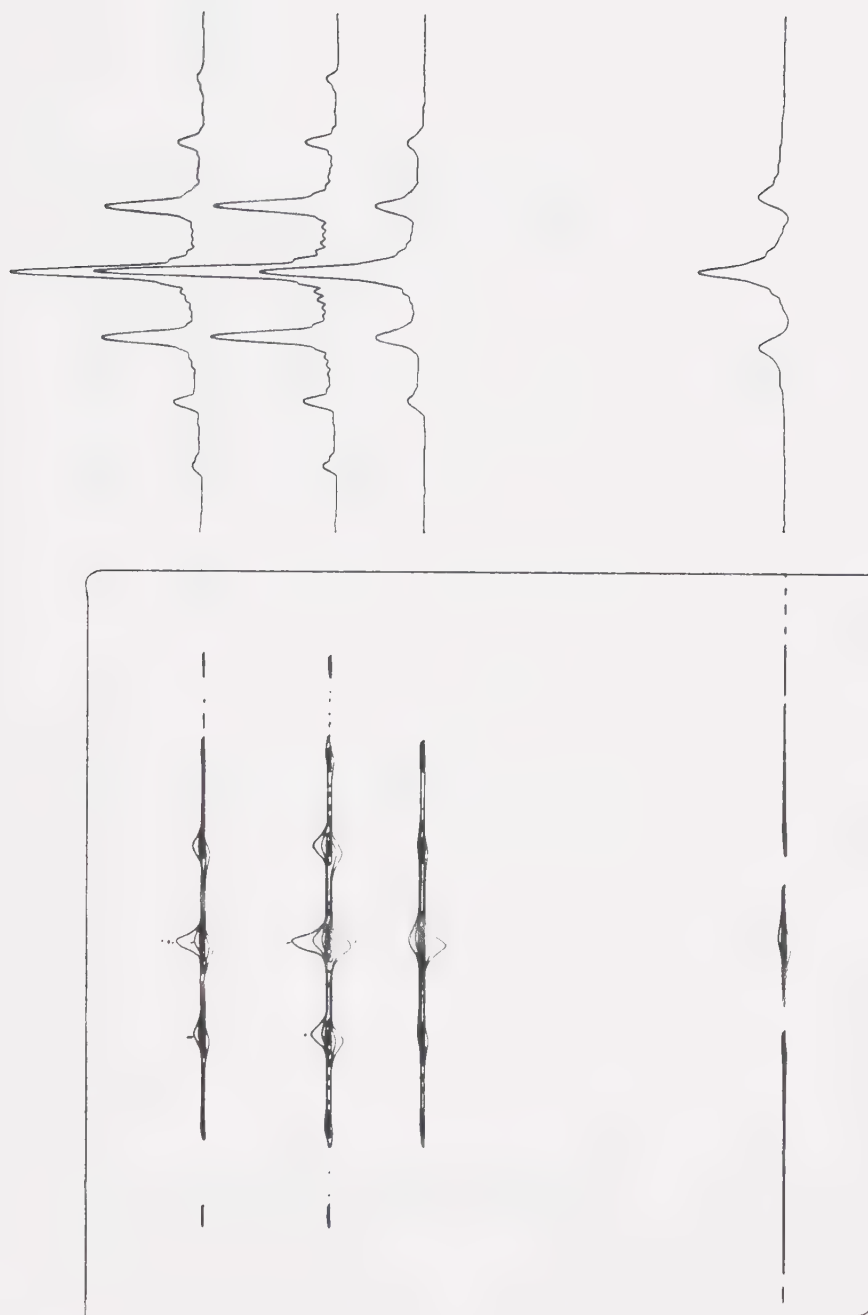


Figure 30.

2D J- δ resolved spectrum of 2-butanol obtained with pulse sequence C (with decoupled acquisition). Horizontal cross sections are shown at the right. Vertical (f_2) span is 4000 Hz/1024 data points, horizontal (f_1) ranges are ± 125 Hz/256 points. Data at 64 values of t_1 were acquired (64 scans per t_1 value) on a Bruker WH-200 spectrometer.

INPUT FOR SEQUENCE C (DECOUPLED) ON CH SYSTEM

```

COMM  ILLUSIONS OF SPIN DECOUPLING  SEQUENCE C
SPIN11S1
WRDM
PULSIA+X
PRECD1
WRDM
DCPLS  T1
PULSIB+X
DCPLS  T1
WRDM
PRECD1
DCPLS  T2
WRDM
MEASIXY0
STOP

```

OUTPUT FOR SEQUENCE C (DECOUPLED) ON CH SYSTEMInitial Thermal Equilibrium Density Matrix

```

DM ( 1, 1) = +( 52.500,  0.0 )
DM ( 2, 2) = +( 47.500,  0.0 )
DM ( 3, 3) = +( -47.500,  0.0 )
DM ( 4, 4) = +( -52.500,  0.0 )

```

Density Matrix After Carbon 90(+X) Pulse and Precession D1

```

DM ( 1, 1) = +( 50.000,  0.0 )
DM ( 1, 2) = +(  0.0 ,  2.500)*EXPI(2*PI*(          1.00 VI   0.50 J )*D1 )
DM ( 2, 2) = +( 50.000,  0.0 )
DM ( 3, 3) = +( -50.000,  0.0 )
DM ( 3, 4) = +(  0.0 ,  2.500)*EXPI(2*PI*(          1.00 VI  -0.50 J )*D1 )
DM ( 4, 4) = +( -50.000,  0.0 )

```

Density Matrix After the Decoupling Period

```

DM ( 1, 2) = +(  0.0 , -1.250)*EXPI(2*PI*(          -1.00 VI  -0.50 J )*D1 )
              +(  0.0 , -1.250)*EXPI(2*PI*(          -1.00 VI   0.50 J )*D1 )
DM ( 3, 4) = +(  0.0 , -1.250)*EXPI(2*PI*(          -1.00 VI  -0.50 J )*D1 )
              +(  0.0 , -1.250)*EXPI(2*PI*(          -1.00 VI   0.50 J )*D1 )

```

Density Matrix During Decoupled Acquisition Period

```

DM ( 1, 2) = +(  0.0 , -1.250)*EXPI(2*PI*(          1.00 VI              )*T2 )
              +(  0.0 , -0.625)*EXPI(2*PI*(          1.00 VI              )*T2 )
              *EXPI(2*PI*(          1.00 J )*D1 )
              +(  0.0 , -0.625)*EXPI(2*PI*(          1.00 VI              )*T2 )
              *EXPI(2*PI*(          -1.00 J )*D1 )

DM ( 3, 4) = +(  0.0 , -1.250)*EXPI(2*PI*(          1.00 VI              )*T2 )
              +(  0.0 , -0.625)*EXPI(2*PI*(          1.00 VI              )*T2 )
              *EXPI(2*PI*(          1.00 J )*D1 )
              +(  0.0 , -0.625)*EXPI(2*PI*(          1.00 VI              )*T2 )
              *EXPI(2*PI*(          -1.00 J )*D1 )

```

Carbon Signals During Decoupled Acquisition

```

SIGNAL =  +(  0.0 , -2.500)*EXPI(2*PI*(          1.00 VI              )*T2 )
           +(  0.0 , -1.250)*EXPI(2*PI*(          1.00 VI              )*T2 )
           *EXPI(2*PI*(          1.00 J )*D1 )
           +(  0.0 , -1.250)*EXPI(2*PI*(          1.00 VI              )*T2 )
           *EXPI(2*PI*(          -1.00 J )*D1 )

```

Figure 31. Input data and output from simulation of gated decoupler pulse sequence C (with decoupled acquisition) on CH system.

OUTPUT FOR SEQUENCE C (DECOUPLED) ON CH₂ SYSTEM

Carbon Signals During Decoupled Acquisition

SIGNAL =	+(0.0 , -5.000)*EXPI(2*PI*(1.00 VI) *T2)
	+(0.0 , -1.667)*EXPI(2*PI*(1.00 VI) *T2)
	*EXPI(2*PI*(1.00 J) *D1)
	+(0.0 , -0.833)*EXPI(2*PI*(1.00 VI) *T2)
	*EXPI(2*PI*(2.00 J) *D1)
	+(0.0 , -1.667)*EXPI(2*PI*(1.00 VI) *T2)
	*EXPI(2*PI*(-1.00 J) *D1)
	+(0.0 , -0.833)*EXPI(2*PI*(1.00 VI) *T2)
	*EXPI(2*PI*(-2.00 J) *D1)

Figure 32. Output data from simulation of gated decoupler pulse sequence C (with decoupled acquisition) on CH₂ system.

OUTPUT FOR SEQUENCE C (DECOUPLED) ON CH₃ SYSTEM

Carbon Signals During Decoupled Acquisition

SIGNAL =	+(0.0 , -7.500)*EXP1(2*PI*(1.00 VI)•T2)
	+(0.0 , -4.375)*EXP1(2*PI*(1.00 VI)•T2)
	•EXP1(2*PI*(1.00 J)•D1)
	+(0.0 , -1.250)*EXP1(2*PI*(1.00 VI)•T2)
	•EXP1(2*PI*(2.00 J)•D1)
	+(0.0 , -0.625)*EXP1(2*PI*(1.00 VI)•T2)
	•EXP1(2*PI*(3.00 J)•D1)
	+(0.0 , -4.375)*EXP1(2*PI*(1.00 VI)•T2)
	•EXP1(2*PI*(-1.00 J)•D1)
	+(0.0 , -1.250)*EXP1(2*PI*(1.00 VI)•T2)
	•EXP1(2*PI*(-2.00 J)•D1)
	+(0.0 , -0.625)*EXP1(2*PI*(1.00 VI)•T2)
	•EXP1(2*PI*(-3.00 J)•D1)

Figure 33. Output data from simulation of gated decoupler pulse sequence C (with decoupled acquisition) on CH₃ system.

$$\tilde{\rho}(0) = (1/2) \begin{bmatrix} \delta+\Delta & 0 & 0 & 0 \\ 0 & -\delta+\Delta & 0 & 0 \\ 0 & 0 & \delta-\Delta & 0 \\ 0 & 0 & 0 & -\delta-\Delta \end{bmatrix}, \quad [4-22]$$

where Δ and δ have been set at 100 and 5 respectively in the simulation program. The application of a carbon 90° pulse followed by the free precession period $D1$ transforms the density matrix to

$$\tilde{\rho}(D1) = (1/2) \begin{bmatrix} \Delta & g & 0 & 0 \\ g^* & \Delta & 0 & 0 \\ 0 & 0 & -\Delta & h \\ 0 & 0 & h^* & -\Delta \end{bmatrix}, \quad [4-23]$$

where $g = i\delta \exp\{2\pi i (VI+J/2)D1\}$, and

$h = i\delta \exp\{2\pi i (VI-J/2)D1\}$.

Proton decoupling is carried out during two $T1$ time periods, in the middle of the evolution period $(D1+2T1+D1)$. It should be noted that the time period $D1 = T1$, and it is only the program limitation which dictates the use of two different time variables. A carbon 180° pulse is applied in the middle of the decoupling period $(2T1)$. The density matrix at the end of the decoupling period is given by (Figure 31)

$$\tilde{\rho}(D1+2T1) = (1/4) \begin{bmatrix} 0 & j & 0 & 0 \\ j^* & 0 & 0 & 0 \\ 0 & 0 & 0 & j \\ 0 & 0 & j^* & 0 \end{bmatrix}, \quad [4-24]$$

where $j = -i\delta[\exp\{2\pi i(-VI-J/2)D1\} + \exp\{2\pi i(-VI+J/2)D1\}]$. Equation [4-24] shows that during the decoupling period the carbon magnetization components remain fixed in the carbon rotating frame and the proton spin quantum numbers of the magnetizations associated with the proton spin states to be randomized. Further free precession for a period $D1$ serves to refocus the carbon chemical shifts developed during the initial $D1$ period. The density matrix during decoupled acquisition of carbon spin signals, is given by (Figure 31)

$$\tilde{\rho}(D1,T2) = (1/8) \begin{bmatrix} 0 & k & 0 & 0 \\ k^* & 0 & 0 & 0 \\ 0 & 0 & 0 & k \\ 0 & 0 & k^* & 0 \end{bmatrix}, \quad [4-25]$$

where $k = -i\delta \exp\{2\pi i VI T2\}[\exp\{2\pi i J D1\} + 2 + \exp\{-2\pi i J D1\}]$. The carbon signals are given by (Figure 30)

Signal $\propto -i(\delta/4) \exp\{2\pi i \text{VI T}_2\} \times$

$$[\exp\{2\pi i \text{J D}_1\} + 2 + \exp\{-2\pi i \text{J D}_1\}] , \quad [4-26]$$

which gives rise to the 1:2:1 triplet in the 2D map. The program output given in Figures 32 and 33, show that one obtains a quintet with relative intensities 1:2:6:2:1 for CH_2 and a septet with relative intensities 1:2:7:21:7:2:1 for the CH_3 group, as obtained in the experimental 2D map for 2-butanol in Figure 30.

When the proton decoupler is gated off during the acquisition period, the coupled carbon frequencies present during the acquisition period T_2 , gives rise to a $(n+1) \times (n+1)$ parallelogram of peaks for the CH_n group in the 2D map (Figure 34). This observation can be rationalized by considering the density matrix for the CH group (Figure 35) during coupled acquisition given by

$$\tilde{\rho}(\text{D}_1, \text{T}_2) = (1/4) \begin{bmatrix} 0 & n & 0 & 0 \\ n^* & 0 & 0 & 0 \\ 0 & 0 & 0 & m \\ 0 & 0 & m^* & 0 \end{bmatrix} , \quad [4-27]$$

where $n = -i\delta \exp\{2\pi i(\text{VI} + \text{J}/2)\text{T}_2\} [1 + \exp\{2\pi i \text{J D}_1\}]$, and

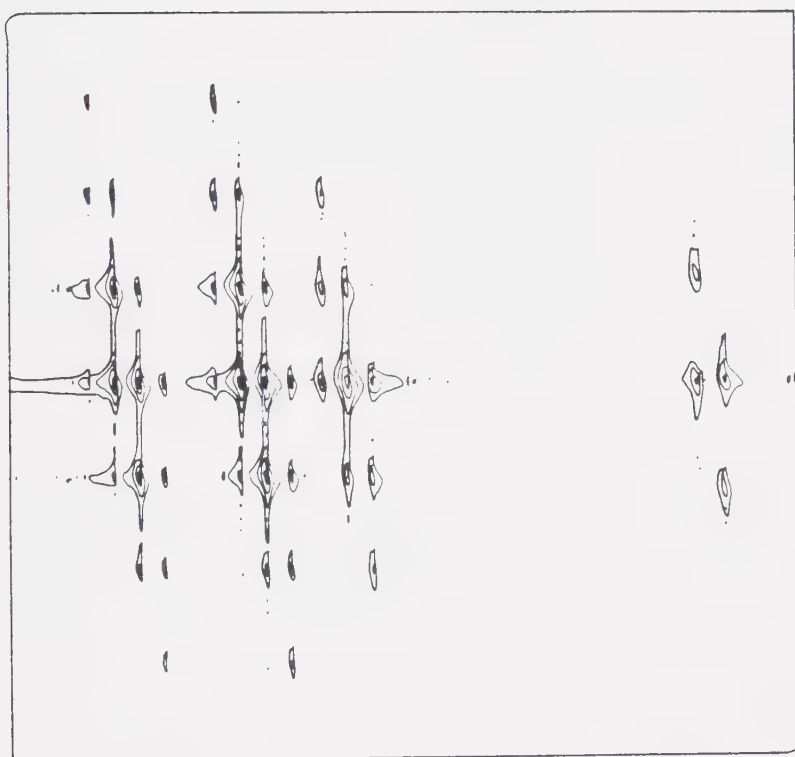


Figure 34. 2D J- δ resolved spectrum of 2-butanol obtained with pulse sequence C (with coupled acquisition). Frequency ranges are as in Figure 30. The amplitudes of the horizontal cross sections are expected to have intensity ratios: 1:1:1:1 (CH group); 1:1:1:1:4:1:1:1:1 (CH₂ group); and 1:1:1:1:1:1:5:1:1:1:1:1:1:1 (CH₃ group).

OUTPUT FOR SEQUENCE C (COUPLED) ON CH SYSTEM

Density Matrix During Acquisition (Decoupler Gated Off)

DM (1, 2) = +(0.0 , -1.250)*EXPI(2*PI*(1.00 VI 0.50 J)*T2)
 +(0.0 , -1.250)*EXPI(2*PI*(1.00 VI 0.50 J)*T2)
 *EXPI(2*PI*(1.00 J)*D1)
 DM (3, 4) = +(0.0 , -1.250)*EXPI(2*PI*(1.00 VI -0.50 J)*T2)
 *EXPI(2*PI*(-1.00 J)*D1)
 +(0.0 , -1.250)*EXPI(2*PI*(1.00 VI -0.50 J)*T2)

Carbon Signals During Acquisition (Decoupler Gated Off)

SIGNAL = +(0.0 , -1.250)*EXPI(2*PI*(1.00 VI 0.50 J)*T2)
 +(0.0 , -1.250)*EXPI(2*PI*(1.00 VI 0.50 J)*T2)
 *EXPI(2*PI*(1.00 J)*D1)
 +(0.0 , -1.250)*EXPI(2*PI*(1.00 VI -0.50 J)*T2)
 *EXPI(2*PI*(-1.00 J)*D1)
 +(0.0 , -1.250)*EXPI(2*PI*(1.00 VI -0.50 J)*T2)

Figure 35. Output data from simulation of gated decoupler pulse sequence C (with coupled acquisition) on CH system.

$m = -i\delta \exp\{2\pi i(VI-J/2)T_2\}[1 + \exp\{2\pi i J D_1\}]$. The carbon signals are then given by

$$\begin{aligned} \text{Signal} \propto & -i(\delta/4)[\exp\{2\pi i(VI+J/2)T_2\}\{1 + \exp(2\pi i J D_1)\} \\ & + \exp\{2\pi i(VI-J/2)T_2\}\{1 + \exp(-2\pi i J D_1)\}] \quad , \quad [4-28] \end{aligned}$$

which gives rise to a 2×2 parallelogram of peaks with intensity 1:1:1:1, in the 2D contour map. The density matrix simulations for the coupled spectra for CH_2 and CH_3 systems are given in Figures 36 and 37 respectively. For CH_2 and CH_3 systems, one obtains from the calculation, a 3×3 and 4×4 parallelogram of peaks, the positions and relative intensities of which, are in accordance with experimental results for 2-butanol (Figure 34).

IV.3 Summary

Simulations of several pulse sequences applied to a variety of spin systems were included in this chapter, in order to demonstrate some of the applications of the simulation program. The utility of various features of the program, such as rf pulses of any given flip angle, broadband decoupler irradiation facility and the phase cycling feature, were emphasized in the examples. The

OUTPUT FOR SEQUENCE C (COUPLED) ON CH2 SYSTEM

Carbon Signals During Acquisition (Decoupler Gated Off)

```

SIGNAL =  +( 0.0 , -0.833)*EXPI(2*PI*(          1.00 VI   1.00 J  )*T2 )
          +( 0.0 , -0.833)*EXPI(2*PI*(          1.00 VI   1.00 J  )*T2 )
            *EXPI(2*PI*(          1.00 J  )*D1 )
          +( 0.0 , -0.833)*EXPI(2*PI*(          1.00 VI   1.00 J  )*T2 )
            *EXPI(2*PI*(          2.00 J  )*D1 )
          +( 0.0 , -0.833)*EXPI(2*PI*(          1.00 VI          )*T2 )
            *EXPI(2*PI*(         -1.00 J  )*D1 )
          +( 0.0 , -3.333)*EXPI(2*PI*(          1.00 VI          )*T2 )
          +( 0.0 , -0.833)*EXPI(2*PI*(          1.00 VI          )*T2 )
            *EXPI(2*PI*(          1.00 J  )*D1 )
          +( 0.0 , -0.833)*EXPI(2*PI*(          1.00 VI  -1.00 J  )*T2 )
            *EXPI(2*PI*(         -2.00 J  )*D1 )
          +( 0.0 , -0.833)*EXPI(2*PI*(          1.00 VI  -1.00 J  )*T2 )
            *EXPI(2*PI*(         -1.00 J  )*D1 )
          +( 0.0 , -0.833)*EXPI(2*PI*(          1.00 VI  -1.00 J  )*T2 )

```

Figure 36. Output data from simulation of gated decoupler pulse sequence C (with coupled acquisition) on CH₂ system.

OUTPUT FOR SEQUENCE C (COUPLED) ON CH3 SYSTEM

Carbon Signals During Acquisition (Decoupler Gated Off)

SIGNAL =	+(0.0 , -0.625)*EXPI(2*PI*(1.00 VI	1.50 J)*T2)
	+(0.0 , -0.625)*EXPI(2*PI*(1.00 VI	1.50 J)*T2)
	*EXPI(2*PI*(1.00 J)*D1)
	+(0.0 , -0.625)*EXPI(2*PI*(1.00 VI	1.50 J)*T2)
	*EXPI(2*PI*(2.00 J)*D1)
	+(0.0 , -0.625)*EXPI(2*PI*(1.00 VI	1.50 J)*T2)
	*EXPI(2*PI*(3.00 J)*D1)
	+(0.0 , -0.625)*EXPI(2*PI*(1.00 VI	0.50 J)*T2)
	*EXPI(2*PI*(-1.00 J)*D1)
	+(0.0 , -3.125)*EXPI(2*PI*(1.00 VI	0.50 J)*T2)
	+(0.0 , -3.125)*EXPI(2*PI*(1.00 VI	0.50 J)*T2)
	*EXPI(2*PI*(1.00 J)*D1)
	+(0.0 , -0.625)*EXPI(2*PI*(1.00 VI	0.50 J)*T2)
	*EXPI(2*PI*(2.00 J)*D1)
	+(0.0 , -0.625)*EXPI(2*PI*(1.00 VI	-0.50 J)*T2)
	*EXPI(2*PI*(-2.00 J)*D1)
	+(0.0 , -3.125)*EXPI(2*PI*(1.00 VI	-0.50 J)*T2)
	*EXPI(2*PI*(-1.00 J)*D1)
	+(0.0 , -3.125)*EXPI(2*PI*(1.00 VI	-0.50 J)*T2)
	+(0.0 , -0.625)*EXPI(2*PI*(1.00 VI	-0.50 J)*T2)
	*EXPI(2*PI*(1.00 J)*D1)
	+(0.0 , -0.625)*EXPI(2*PI*(1.00 VI	-1.50 J)*T2)
	*EXPI(2*PI*(-3.00 J)*D1)
	+(0.0 , -0.625)*EXPI(2*PI*(1.00 VI	-1.50 J)*T2)
	*EXPI(2*PI*(-2.00 J)*D1)
	+(0.0 , -0.625)*EXPI(2*PI*(1.00 VI	-1.50 J)*T2)
	*EXPI(2*PI*(-1.00 J)*D1)
	+(0.0 , -0.625)*EXPI(2*PI*(1.00 VI	-1.50 J)*T2)

Figure 37. Output data from simulation of gated decoupler pulse sequence C (with coupled acquisition) on CH₃ system.

experiments simulated in this chapter included DEPT, selective 2D heteronuclear shift correlation, INADEQUATE and 2D gated J- δ correlation experiments which demonstrate certain unexpected effects of spin decoupling.

PART 2

NUCLEAR RELAXATION STUDY OF
HEXAMETHYLPHOSPHORAMIDE

CHAPTER V

DESCRIPTION OF SPIN RELAXATION MECHANISMS

V.1 Introduction

In this chapter, some of the important spin relaxation mechanisms and the application of relaxation rate measurements in studying molecular motion in liquids are discussed. Various relaxation mechanisms and their characteristic correlation times are described. Theoretical relaxation rate expressions for various mechanisms are presented. A brief review of the diffusion models for describing molecular motion in liquids is also given. Finally the objectives of the project are described.

V.2 Spin Relaxation and Applications of Relaxation Studies

Magnetic relaxation processes are responsible for restoring any non-equilibrium state of the spin system to thermal equilibrium. The interactions which cause magnetic relaxation give rise to a coupling between the

nuclear spin system and the lattice. The lattice acts as a heat sink and comprises the collection of translational, rotational and other degrees of freedom of the molecule (65). The coupling between nuclear spins and lattice acts as a pathway for energy transfer from the spins to the lattice. The coupling between the spin system and the lattice is inherently weak (66), but it is via this coupling that nuclear spin relaxation occurs.

A spin system in a static magnetic field at equilibrium, has the various spin states populated according to the Boltzmann probability distribution. Any perturbation from this equilibrium state causes the system to respond in such a way that the spin populations return to thermal equilibrium values, with the rate of recovery characterized by the time constants T_1 and T_2 (66). The spin-lattice relaxation time T_1 is of more importance in the study of molecular mechanics in liquids than is the spin-spin relaxation time T_2 , due to the ease of measurement of T_1 . The spin-lattice relaxation time describes the recovery of the longitudinal component of the macroscopic magnetization (M_z) back to its thermal equilibrium value, while the spin-spin relaxation time T_2 determines the recovery of the transverse components (M_x and M_y) from a nonequilibrium state (66). The longitudinal components and transverse components may have

different rates associated with them since the dynamics of the interaction processes associated with their recovery are different. For the interaction process to be effective in bringing about relaxation, it must be time dependent, must involve the spin of interest and should fluctuate on a time scale such that its frequency is comparable to or greater than the resonance frequency of the spin. T_1 relaxation is affected by high frequency processes, while the T_2 relaxation is influenced by high frequency processes as well as those with low frequencies such as chemical exchange (3). Hence in most cases, T_2 can never be longer than T_1 , however, for molecules tumbling rapidly in liquids, they are often equal. Relaxation effects have been introduced phenomenologically (67) in the classical Bloch equations:

$$\frac{dM_z}{dt} = - \frac{(M_z - M_0)}{T_1} ,$$

$$\frac{dM_x}{dt} = \omega_0 M_y - \frac{M_x}{T_2} , \quad [5-1]$$

$$\frac{dM_y}{dt} = -\omega_0 M_x - \frac{M_y}{T_2} ,$$

where M_0 is the thermal equilibrium value of M_z and ω_0 is the resonance frequency of the spin.

Magnetic relaxation rate measurements provide a powerful and highly versatile tool for the study of molecular dynamics and structure (3,65,68-71). In the field of molecular dynamics, overall molecular reorientation (66,70), internal motion of molecular fragments in nonrigid systems (72,73) and relative translational motion between molecules (66,70) can be investigated using spin relaxation rate measurements. Relaxation data can be used to test models (77-80) of the microdynamic behavior of liquids. In the determination of organic molecular structure, nuclear spin relaxation measurements play a very useful role, particularly the ^{13}C spin relaxation rates. Many of these applications have been reviewed by Lyster et al. (68). The ^{13}C - ^1H dipolar relaxation rates have been used in spectral assignment since they can provide information regarding the number of protons and their distances to the carbon nucleus. This method is commonly used for distinguishing between protonated and non-protonated carbons. Another common technique which is used in assignment of complex spectra is specific deuteration.

As mentioned above, nuclear spin relaxation can be induced by any mechanism which provides a time dependent magnetic field at the site of the nucleus (3,66). Hence spin relaxation measurements are an excellent tool for

probing molecular dynamics, since molecular motion renders time dependence to many of the spin interactions. More specifically, the relaxation rates are functions of certain quantities known as the correlation times. A correlation time is the time constant characterizing the decay of a particular molecular property, i.e. it is the time in which the system loses memory of its previous state. Hence, for short correlation times, the system loses phase memory quickly and for long correlation times, the phase memory persists for longer periods, i.e. a correlation time can be viewed qualitatively as the time constant characterizing the exponential decay of the correlation function for the particular property.

The physical interactions which give rise to various relaxation processes have different correlation functions. The relaxation rates arising from these interactions are proportional to the spectral density of the interaction, which is just the Fourier transform of the correlation function (66). The spectral density, which is a function of frequency, describes how the power available for relaxation is distributed along the frequency dimension. The spin relaxation rate is related to the spectral density by certain constants characterizing the intensity of the coupling between the spins and the lattice. The importance of the relaxation

rate measurements stems from the fact that if these coupling constants are known, the experimental determination of relaxation rates enables the measurement of the correlation times. To make further connection of the correlation times to the way in which molecules reorient in liquids, one has to refer to appropriate models for the molecular reorientation. The predictions of the particular model, about the relation between different correlation times, are then compared with the experimentally observed variation. Thus relaxation studies are of great importance in testing various theoretical models describing molecular rotation (70).

V.3 Spin Relaxation Mechanisms

The spin-lattice relaxation rate of a nucleus is the sum of contributions from various relaxation mechanisms. For the general case, the time dependent interaction $\hat{H}_{int}(t)$ which gives rise to spin relaxation is of the form (66)

$$\hat{H}_{int}(t) = \sum_q \hat{I}_q F_q(t) , \quad [5-2]$$

where \hat{I}_q are spin operators (spin angular momentum operators and bilinear combinations of these operators)

and $F_q(t)$ are time dependent lattice functions characteristic of the spin-lattice interaction. The time dependence of \hat{H}_{int} is assumed to be random, and the relaxation rate, R_1 , in the limit of strong motional narrowing, is a linear combination of the form

$$R_1 = 1/T_1 \propto \sum_q a_q |F_q(0)|^2 \tau_q, \quad [5-3]$$

where τ_q is the correlation time over which the correlation function $\overline{F_q(t) F_q^*(0)}$ has significant amplitude, and a_q are simple numerical coefficients. τ_q is the zero frequency component of the spectral density $J^{(q)}(\omega)$, and will be related to the details of molecular motion which modulate $F_q(t)$, and $|F_q(0)|^2$ will be a measure of the strength of the interaction producing spin relaxation.

Some of the important relaxation mechanisms are intramolecular and intermolecular dipole-dipole interactions, spin-rotation interactions, nuclear quadrupolar interactions and chemical shift anisotropy. In the case of spin 1/2 nuclei, the dipolar interactions and spin-rotation interactions are the major contributors to relaxation, while in nuclei which have a quadrupole moment, the quadrupolar relaxation almost entirely determines the relaxation rate. In certain cases, the

presence of internal motion of groups can influence the relaxation rates due to some of the above mentioned interactions.

a. Dipolar Interactions

Dipolar interactions between two spins on the same molecule acquire time dependence when the angle between the internuclear vector (which is fixed in the molecular frame) and the applied field varies with time as a result of molecular reorientation. Hence the intramolecular dipolar interaction is characterized by a molecular reorientational correlation time τ_θ . The functions which describe the orientation of the internuclear vector with respect to the applied field are the spherical harmonics of order two, and τ_θ then describes the decay time for the correlation function of the spherical harmonics. The case of intermolecular dipolar interaction is more complicated since in this case, the time dependence of the interaction originates from two sources: (i) as a result of the relative translational motion of neighboring molecules, the internuclear vector changes its magnitude and direction with time, (ii) molecular reorientation imparts further time dependence to the dipolar interactions. As a result, the translational diffusion coefficient of the molecule enters into the relaxation rate expressions.

Since τ_θ decreases with increasing temperature, the contribution of the dipolar mechanism to R_1 decreases with temperature.

The expression for the relaxation rate, R_1^I , due to dipolar interactions between two like spins I and S, has been given by Abragam (66) as

$$R_1^I = (3/2) \gamma_I^4 \hbar^2 I(I+1) \{ J^{(1)}(\omega_I) + J^{(2)}(2\omega_I) \} , \quad [5-4]$$

where γ_I , I and ω_I represent the magnetogyric ratio, spin and Larmor frequency of the nucleus I. The functions $J^{(q)}(\omega)$ represent the spectral densities of the dipolar interactions. When I and S are unlike spins, the relaxation rate of nucleus I is given by (66)

$$R_1^I = \gamma_I^2 \gamma_S^2 \hbar^2 S(S+1) \{ (1/12) J^{(0)}(\omega_I - \omega_S) + (3/2) J^{(1)}(\omega_I) + (3/4) J^{(2)}(\omega_I + \omega_S) \} , \quad [5-5]$$

where S is the spin of the S nucleus. The above expressions for the relaxation rates are general in that the spectral densities have not been specified as arising from any specific mechanism such as random rotation or translation.

1. Random Rotation

Using the Debye model for random rotation of molecules, the relaxation rate expression for like spins is given by (66)

$$R_1 = (2/5)r^{-6} \gamma_I^4 \hbar^2 I(I+1) \left\{ \tau_\theta / (1 + \omega_I^2 \tau_\theta^2) + 4\tau_\theta / (1 + 4\omega_I^2 \tau_\theta^2) \right\}, \quad [5-6]$$

where r is the internuclear distance. In the limit of extreme narrowing, i.e. $\omega_I^2 \tau_\theta^2 \ll 1$, and for spin $1/2$ nuclei, Equation [5-6] reduces to

$$R_1 = (3/2) r^{-6} \gamma_I^4 \hbar^2 \tau_\theta. \quad [5-7]$$

For the case of unlike spins I and S , the relaxation rate of the I nucleus at extreme narrowing is given by

$$R_1^I = 4\gamma_I^2 \gamma_S^2 \hbar^2 S(S+1) \tau_\theta / (3 r^6).$$

The correlation time τ_θ is related to the overall rotational diffusion coefficient D_r by $\tau_\theta = 1/(6D_r)$.

In the case where internal motion of groups is present, the internal motion is superimposed on the overall rotation of the molecule and the effective

correlation time τ_{eff} is a function of τ_θ and the internal motion correlation time τ_i . The dynamics of internal rotation can be studied if τ_i can be isolated. The most common method of isolation of τ_i is by studying the relaxation rates of two different nuclei such that τ_{eff} and τ_θ can be determined independently. The mathematical ground work for isolating the internal motion from the overall rotation was provided by Woessner (72). The applications of this method have been compiled in a review by Lambert et al. (81). If the internal motion is independent of the overall motion and if the internal rotation occurs about the principal axis in the molecular system, its effect can be introduced into the dipolar rate equation by simply adding an internal diffusion constant D_i ($D_i = 1/\tau_i$) to the diffusion constant D_r about the principal axis (72). For an isotropic (spherical) system, the intramolecular dipolar relaxation rate in the presence of internal motion is (72)

$$R_1^I = (\gamma_I^2 \gamma_S^2 \hbar^2 / r^6) [A / (6D_r) + B / (6D_r + D_i) + C / (6D_r + 4D_i)], \quad [5-8]$$

where the geometrical constants A, B and C are given by

$A = (3 \cos^2 \Delta - 1)^2 / 4$, $B = 3 \sin^2 \Delta \cos^2 \Delta$, $C = (3/4) \sin^4 \Delta$, where Δ is angle between the internuclear vector and the internal rotation axis. Equation [5-8] is derived assuming that the internal diffusion is a stochastic process and that all internal rotational orientations have equal probability.

2. Translational Motion

Based on a simple diffusion model of translation, Abragam (66) has given the internuclear dipolar relaxation rate as

$$R_1 = \pi N \gamma_I^4 \hbar^2 / (5 a D_t) , \quad [5-9]$$

where N is the number of spins per cm^3 , a is the hydrodynamic radius of the molecule and D_t is the translational diffusion coefficient. This simple model of translation presented by Abragam (66) is in fact quite crude. It fails to consider that, in general, intermolecular dipolar interactions depend on both translational and reorientational motion and that the correlation function for the interaction depends on both angles and distances (82). Features should also be introduced to account for the fact that nuclei are not necessarily at the center of the molecule (82). Another drawback of the simple diffusion model is that the

microscopic detail of the translational motion is obscured since only the gross features of translation are described by the diffusion coefficient D_t (82). Torrey (83) has introduced random walk theory to calculate the internuclear dipolar relaxation rate and other models are due to Hubbard (84) and Oppenheim and Bloom (85). Hubbard's model takes into account the effects of molecular reorientation on the intermolecular dipolar relaxation rate.

b. Spin-Rotation Interaction

The spin-rotation relaxation mechanism is of importance in spin 1/2 systems. In this case, the rotational angular momentum of the molecule produces fluctuating magnetic fields at the site of the nucleus since the electron density in the molecule behaves as a charge system with an angular velocity. Hence the fluctuations of the magnetic fields so produced are determined by the time dependence of the angular momentum of the molecule, with the correlation time τ_J . In the case of spherical molecules the relaxation rate is given by (86,87)

$$R_1 = 2kTIC^2\tau_J/\hbar^2 , \quad [5-10]$$

where I is the moment of inertia and C is the isotropic part of the spin-rotation constant. For symmetric top molecules the relaxation rate expression is given by (88)

$$R_1 = 2kT(C_{\parallel}^2 I_{\parallel} + 2C_{\perp}^2 I_{\perp})\tau_J / (3\hbar^2) , \quad [5-11]$$

where the symbols \parallel and \perp denote the parallel and perpendicular components of the respective quantities. It has been shown by Hubbard (84) that when $\tau_J \ll \tau_{\theta}$ and in extreme narrowing, the spin-rotation relaxation rate is proportional to τ_J . Hubbard also showed that τ_J is proportional to D_r/T . τ_J increases with increasing temperature and hence the spin-rotation mechanism gains importance at higher temperatures.

τ_J contains information on the molecular collision frequency. The spin-rotation interaction is more important in small symmetrical molecules with weak intermolecular interactions since they tend to possess rather large angular velocities. Determination of the spin-rotation contribution to the total relaxation rate is often difficult since the components of the spin-rotation interaction tensor are not usually known. Flygare (89) has proposed a method which circumvents the task of determining the elements of the spin-rotation tensor experimentally. This method takes advantage of the

relation between spin-rotation constants and chemical shift anisotropy. Spin-rotation constants can be related to chemical shifts since both depend on the electron density distribution in the molecule.

c. Nuclear Quadrupole Interaction

For nuclei with spin $I > 1/2$ the nuclear quadrupolar contribution dominates the total relaxation rate (3,66,70). Nuclei with spin $I > 1/2$ possess an electric quadrupole moment (produced by the non-spherical symmetry of the nuclear charge distribution) which interacts with the electric field gradient produced by the surrounding electric charges at the site of the nucleus. The electric field gradient becomes time dependent due to molecular motion. The quadrupole interaction vanishes when the nucleus has an electrical environment which has cubic or higher symmetry (70).

Quadrupolar relaxation is an intramolecular process and provides a very convenient method for determining the reorientational correlation time τ_θ in many cases. For the case of extreme narrowing, the expression for quadrupolar relaxation rate has been given by Abragam (66) as

$$R_1 = \frac{3}{40} \frac{2I+3}{I^2(2I-1)} \left(1 - \frac{\eta^2}{3}\right) \left(\frac{e^2 q Q}{h}\right)^2 \tau_\theta, \quad [5-12]$$

where I is the spin quantum number, (e^2qQ/h) is the quadrupole coupling constant, and η is the asymmetry parameter

$$\eta = \frac{\partial^2 V / \partial x^2 - \partial^2 V / \partial y^2}{\partial^2 V / \partial z^2}, \quad [5-13]$$

where $V(x,y,z)$ is the electric potential due to the electrons and $\{x,y,z\}$ form a molecular coordinate system centred at the nucleus with z axis chosen to be the principal axis of highest symmetry for the field gradient tensor.

For cases where the asymmetry parameter η and the nuclear quadrupole coupling constant can be determined, Equation [5-12] provides a more convenient and accurate method for determining τ_0 than the dipolar relaxation rate expression in Equation [5-7]. This is due to the fact that for nuclei with a quadrupole moment, quadrupolar interaction dominates strongly all other mechanisms and there are no intermolecular contributions to the relaxation rate.

If the quadrupolar nucleus is situated in a group which executes internal rotation, the effect of the internal motion is superimposed on the overall reorientational motion. Following Woessner's approach (72)

for internal motion modulation of dipolar interactions, the reorientation correlation time in Equation [5-12] can be replaced (73,126) by an effective correlation time as is done in Equation [5-8].

V.4 Brief Review of Rotational Diffusion Models

The earliest of the models for rotational diffusion in liquids was proposed by Debye (90) to describe dielectric relaxation. The Debye model of diffusion was applied to spin relaxation by Bloembergen, Purcell and Pound (91). In the Debye model, the motion of molecules in liquid is pictured as the rotation which macroscopic spheres undergo in a continuous viscous medium. The molecules are acted upon by torques produced by the Brownian motion in the fluid. The model further assumes that the duration of each rotational step or the time between the action of two consecutive torques, is small compared to the time required for the molecule to change its orientation appreciably. This implies that the molecule experiences many changes in angular momentum before it changes its orientation. Since the duration of a rotational step is characterized by the angular momentum correlation time τ_J and the overall rotation by the reorientational correlation time τ_θ , the Debye model

assumes that $\tau_\theta \gg \tau_J$. Hubbard (84) has used the classical Langevin approach and shown that, for spherical molecules, the reorientational correlation time τ_θ can be related to the angular momentum correlation time τ_J by

$$\tau_\theta \tau_J = I_{av}/6kT , \quad [5-14]$$

where I_{av} is the average moment of inertia of the molecule, k is the Boltzmann constant and T is the absolute temperature. The assumption that $\tau_\theta \gg \tau_J$ is especially objectionable when dealing with the reorientation of spherical or nearly spherical molecules for which it has been found that τ_θ and τ_J are of the same order of magnitude (79). Thus the Debye model fails to describe molecular reorientation in the whole range of τ_θ variation with τ_J .

When τ_θ and τ_J are of comparable magnitude, the molecule reorients through a large angle in a single diffusion step, just as in the dilute gas where molecules rotate freely between collisions. The concept of free rotation and its effect on τ_θ was recognized by many workers (77,92-94), but many of the theories developed were only approximate and were not valid over the entire range of τ_θ and τ_J .

The first successful theory which did not incorporate the assumption of small angle diffusion was due to Gordon

(77). This model has been called the extended diffusion model and he applied it to the case of linear molecules. In the extended diffusion model, no restrictions on the size of reorientational steps were imposed and the model follows the succession of diffusive steps in microscopic detail. The extended diffusion model has been extended to apply for spherical top molecules by McClung (79,95,96), Mountain (97), McClung and Versmold (80); for symmetric top molecules by McClung (98), Fixman and Rider (78), and other workers (99-102); and to asymmetric top molecules by Leicknam et al. (103).

In the extended diffusion model, the molecular motion is examined in detail during each successive diffusion step. It is assumed that the molecule rotates freely between collisions. The collision events are thought to be instantaneous and act as terminators of the diffusive steps. As the result of a collision event, the molecular angular momentum is randomized. This leads to two extreme situations: 1) a case where both the direction and the angular momentum are randomized, referred to as the J-diffusion model and, 2) a case where only the direction of the angular momentum is randomized - the M-diffusion model. The durations of the diffusive steps are assumed to be random and to follow a Poisson distribution with the characteristic time τ_J , since each collision event randomizes the components of the angular momentum.

It has been shown (79) that the extended J-diffusion model gives the same results as the Debye model when $\tau_\theta \gg \tau_J$ and reduces to the perturbed-free-rotor model (104) when $\tau_\theta \ll \tau_J$. In the Debye limit ($\tau_\theta \gg \tau_J$), the variation of τ_θ with respect to τ_J for the J-diffusion model agrees with Equation [5-14] derived by Hubbard (86). In this limit, τ_θ has an inverse τ_J dependence. When $\tau_\theta \ll \tau_J$, i.e. at the perturbed-free-rotor limit or dilute gas limit, τ_θ has a direct dependence on τ_J (104) and

$$\tau_\theta = \tau_J/5 . \quad [5-15]$$

The calculations done (79) using the extended diffusion model show the transition from the Debye limit to the perturbed-free-rotor limit. Calculations using the M-diffusion model show that, in the Debye limit, τ_θ is inversely proportional to τ_J , but the proportionality constant is different from that in the Debye model. This has been explained (79,105) as due to the fact that Debye model assumes randomization of the magnitude of the angular momentum at each step termination which is not assumed in the extended M-diffusion model. When the anisotropic intermolecular interactions are very weak, the M-diffusion model may be a better approximation because

randomization of the magnitude of the angular momentum at each collisional event is expected to be less probable. The J-diffusion and M-diffusion models are equivalent in the dilute gas limit, and τ_θ exhibits a linear relationship with τ_J .

The application of the extended diffusion models has been carried out by comparing the predicted variation of τ_θ with τ_J , with the observed variation determined using spin relaxation measurements. Independent determinations of τ_θ and τ_J can be made experimentally from relaxation time measurements of different nuclei in suitable molecules. An exhaustive survey of these applications has been given by McClung (105). The extended diffusion model has been applied to linear, spherical top and symmetric top molecules. In most of the applications, τ_J was determined from the measurements of spin-rotational contributions to the relaxation rates of spin 1/2 nuclei such as ^1H , ^{19}F and ^{31}P , and τ_θ was determined from relaxation rates of quadrupolar nuclei. In most cases, the J-diffusion limit of the extended diffusion model was found to give results in quantitative agreement with the experimentally observed τ_θ variation with τ_J . The M-diffusion model did not seem to agree very well with most of the experimental observations. The J-diffusion model results however, as expected, did not agree well with

experimental observations on certain linear molecules which have strong intermolecular interactions such as hydrogen bonding. The reasonably widespread success of the J-diffusion model is not surprising since it is capable of yielding results equivalent to the classical Debye diffusion model when $\tau_\theta \gg \tau_J$ and those similar to the results given by dilute gas model at the limit $\tau_\theta \ll \tau_J$.

V.5 Objectives of the Project

The primary objective of this work is to investigate the relative importance of various relaxation mechanisms in the molecule hexamethylphosphoramide, $\text{O}=\text{P}[\text{N}(\text{CH}_3)_2]_3$, (HMPA) and its deuterated analog (HMPD). Relaxation rates for the ^{31}P , ^{14}N , ^2H and ^1H nuclei have been studied over a wide range of temperature. The variation of the translational diffusion coefficient with temperature for hexamethylphosphoramide has been measured to facilitate separation of the contribution to relaxation rates from intermolecular dipolar interactions. It was intended that the reorientational correlation time τ_θ and the angular momentum correlation time τ_J be determined from the relaxation data. With the knowledge of the coupling constants in the relaxation rate

expressions, from other independent sources, the correlation times characterizing various relaxation processes for different nuclei, can be determined. The knowledge of the variation of the reorientational correlation time τ_θ with the angular momentum correlation time τ_J can then be used to test the applicability of the extended diffusion model in describing molecular reorientation in hexamethylphosphoramide.

V.6 Summary

A discussion of various spin relaxation mechanisms, their characteristic correlation times and the application of relaxation data in the study of molecular motion has been presented. Quantitative expressions for various relaxation rates were given. Two models describing molecular rotational motion - the Debye model and the extended diffusion model were described. The objectives of the project were also laid out. The next chapter deals with the experimental aspects of spin-lattice relaxation rate determination and the measurement of translational diffusion coefficients. In the following chapter the results and data analysis for HMPA and HMPD are presented.

CHAPTER VI

EXPERIMENTAL

VI.1 Introduction

This chapter discusses the experimental aspects of the determination of spin-lattice relaxation times and translational diffusion coefficients. The instrumentation used for the measurements is described in brief. Two methods have been adopted for measuring T_1 relaxation times: (i) the inversion recovery experiment and (ii) the triplet sequence which was used for measuring relatively long relaxation times. The last part of the chapter describes the measurement of translational diffusion coefficients by the stationary (time independent) field gradient method.

VI.2 Sample Preparation

Hexamethylphosphoramide (Aldrich Chemical Co.) was dried by storing over molecular sieves (Fisher Scientific Co. Type 3A). It was then vacuum distilled into a clean NMR tube attached to the vacuum assembly. The sample was

then degassed using the pump-freeze-thaw technique three times. After degassing, the NMR tube was sealed under vacuum. An identical procedure was used for preparing the sample of the deuterated compound. For the measurement of ^{31}P T_1 in HMPD, a chemical means of deoxygenation of the sample using $[\text{Co}^{\text{II}}(\text{bipy})_3](\text{ClO}_4)_2$ with sodium borohydride (106) was employed. In an oxygenated solution these compounds give a pale yellow-brown color which changes on removal of oxygen to an extremely oxygen sensitive intense blue color (106). This mixture was added to the HMPD sample and the HMPD was vacuum distilled into an NMR tube. The ^{31}P relaxation times in this sample did not differ significantly from those in the sample prepared with the pump-freeze-thaw degassing technique.

VI.3 Instrumentation

The measurement of T_1 values was carried out with a Bruker SXP4-100 high power pulsed NMR spectrometer and a 14 k Gauss Varian Associates electromagnet and V3506 magnetic field flux stabilizer. The Bruker SXP4-100 pulsed spectrometer was operated under the control of a Nicolet 1180 minicomputer along with a Nicolet 293A programmable pulser. The data were stored on a hard disk using a Diablo Disk Drive Unit under the control of the

Nicolet 1180 minicomputer. Analysis of the data was carried out on the minicomputer in the BASIC language and, to a lesser extent, in the Nicolet 1180 Assembler language.

The spectrometer has four independent radio frequency (rf) channels which can be gated on or off by the Nicolet 293A programmable pulser. The phase of the rf pulse can be continuously adjusted in each of the four independent channels. Tuning the spectrometer to the required radio frequency is carried out by adjusting two variable capacitors on the high power amplifier and on the probe arm.

The detector part of the circuitry consists of a preamplifier followed by an amplifier which can be operated in both phase sensitive and diode detection mode. The amplifier, when operating in the diode detection mode, gives a signal which is the square root of the sum of the absorption and dispersion signals. The signal after diode detection is unaffected by moderate changes in magnetic field or radio frequency. Phase sensitive detection has the advantage of linearity of response over the full dynamic range of the amplifier and better signal-to-noise ratio, particularly at low signal intensities. The detector also contains a rf filter with band width adjustable from 100 kHz to 100 Hz.

The pulse lengths corresponding to 90° and 180° tip angles are determined prior to the T_1 experiment. Using a [wait - pulse - acquire] sequence the diode detected signal observed should be a maximum for a 90° pulse and it should be a minimum for a 180° pulse. The spectrometer was tuned prior to determination of the pulse lengths. Tuning was carried out by adjusting the tuning capacitors such that, with an initial pulse length much less than an approximate 90° pulse, the signal observed was a maximum. The pulse length was then increased so that the amplitude of the FID decreased to about three-fourths of its maximum value and the capacitors were again adjusted to give a minimum signal amplitude. Accurate determination of the pulse lengths was carried out using a computer program based on an optimization algorithm (107). This program attempts to minimize the signal obtained after a 180° pulse. The 90° pulse length was then taken as half of the 180° pulse duration.

In experiments requiring rf pulses of different phases, the relative phases of the pulses on each pulse channel were adjusted manually by observing the FID in the phase sensitive mode after a 90° pulse. The phases of the last three channels are always in reference to the phase of the first channel. These relative phases were adjusted to the desired values as required in particular experiments.

In all temperature dependent studies, the temperature of the sample was controlled by a Bruker B-ST 100/700 temperature control unit. A Doric Trendicator 400 digital thermometer using a copper-constantan thermocouple was used to measure the temperature. The temperature was measured before and after the T_1 determination and the variation in temperature was less than $\pm 0.5^\circ\text{C}$. Sample was allowed to equilibrate for 15-20 minutes after insertion into the probe.

VI.4 Measurement of T_1 Relaxation Time

a. Inversion Recovery Experiment

Relaxation times which were not extraordinarily long were measured using this conventional $180^\circ\text{-}\tau\text{-}90^\circ$ pulse sequence (3). The experiment can be represented by, wait- $[180^\circ\text{-}\tau_0\text{-}90^\circ]$ -wait- $[180^\circ\text{-}\tau_0+\Delta\text{-}90^\circ]$ -wait- $[180^\circ\text{-}\tau_0+2\Delta\text{-}90^\circ]$ -..., where τ_0 and Δ are the initial delay and the increment to the delay respectively. The wait time is approximately 5-6 times the T_1 value. Typically about ten τ values were used such that $\tau_0 + 10\Delta \approx 3T_1$. The initial value τ_0 was chosen as 0.7 times the approximate T_1 value. The FID after the 90° pulse was detected in the diode detection mode, digitized and the intensity of the magnetization was calculated by

integrating over about 50 data points in the initial part of the FID. The total acquisition time for the complete FID was typically in the range of 5-25 mS. The signal intensity $M(\tau)$ for each τ value was then fit into an equation of form

$$M(\tau) = A + B \exp(-\tau/T_1) , \quad [6-1]$$

using a non-linear least squares analysis algorithm. The computer program was designed to make repetitive T_1 measurements and to calculate the variance and the standard deviation. The diode detection mode was employed for signal acquisition since it was independent of moderate variations in the magnetic field over the period of time required to carry out the repetitive T_1 measurements.

b. Triplet Sequence

The triplet sequence (108-111) was used for determination of T_1 values which were relatively long. This sequence is more difficult to carry out and has more stringent requirements concerning the accuracy of the pulse lengths. The advantage of using the triplet sequence is the saving in time, since the wait time is avoided. The triplet sequence can be represented by

$180^\circ_x - \tau - [90^\circ_x - \delta - 180^\circ_x - \delta - 90^\circ_x - \Delta]_n$, where δ must be much smaller than T_2 and was typically about 1 ms, and $\Delta = \text{acq.time}/n$, typically about 100 ms. The part of the pulse sequence enclosed by the brackets is repeated n times (typically $n = 256$). Data were acquired after the first 90°_x pulse of the pulse train enclosed in brackets, using the phase sensitive detection mode. Thus 256 data points were collected during the acquisition time, one data point for each pass through the sequence in brackets.

The triplet sequence is basically similar to the inversion recovery sequence, except that after the signal acquisition period, instead of allowing the magnetization to evolve back to the thermal equilibrium value, the dephased magnetization vectors are refocussed by the 180°_x pulse and rotated back to the $-Z$ axis by the second 90°_x pulse. This process is then repeated a number of times, thus collecting a data point $(M(\tau), \tau)$ during each spin echo formation. The data points were fit to Equation [6-1] using the non-linear least squares analysis program. Typical precision of T_1 measurements was about $\pm 5\%$; however, when the T_1 values were very long as in ^{31}P in HMPD the reproducibility was between $\pm 5\%$ and $\pm 10\%$.

VI.5 Measurement of Translational Diffusion Coefficients

The translational diffusion coefficient of hexamethylphosphoramide was measured by the stationary field gradient technique (3,112-114). The amplitude of the spin echo from equivalent spins is modulated by diffusion of spins along a magnetic field gradient in the sample. The effective T_2 relaxation time $T_{2\text{eff}}$ in the presence of a field gradient, contains an extra term involving the diffusion coefficient D_t . Hence for the experimental determination of D_t , the transverse relaxation time is measured using the spin echo technique, in the presence and absence of a magnetic field gradient. Both stationary and time dependent field gradients can be employed (3,115,116); however the experiments carried out here were done using the stationary field gradient.

In the first part of the experiment, the relaxation time T_2 of the sample was determined in the absence of any field gradient using the Carr-Purcell-Meiboom-Gill (CPMG) pulse sequence (112,117). The CPMG pulse sequence can be represented as, $90^\circ_x - \tau/2 - [180^\circ_y - \tau]_n$, where a train of echoes is generated by the 180°_y pulses and the τ time intervals. The 90°_x pulse creates transverse y magnetization which is allowed to dephase for a time period $\tau/2$. A 180°_y pulse is then applied which refocusses

the chemical shift precession and an echo is formed at time $\tau/2$ after the 180°_y pulse. This echo is sampled by the A/D convertor of the 1180 computer. A further train of echoes is formed by successive 180°_y pulses and τ delays. The amplitude $M(t)$ of the spin echo at time t in the absence of magnetic field gradients is given by (3)

$$M(t) = A + B \exp(-t/T_2) , \quad [6-2]$$

where A and B are fitting parameters. In the presence of a field gradient of magnitude G , the echo amplitude is modified as (3,113)

$$M(t) = A + B \exp\left[-t\left(\frac{1}{T_2} + \frac{\gamma^2 G^2 D_t \tau^2}{3}\right)\right] , \quad [6-3]$$

where D_t is the diffusion coefficient and τ is the time between the 180° pulses.

The signal was sampled in the phase sensitive detection mode at the maximum of the echo amplitude. For the case where no field gradient was applied, the T_2 value was determined by fitting the data to Equation [6-2] using a non-linear least squares program. The CPMG sequence compensates for pulse length errors by using a 90° phase shifted channel for the 180° pulses. Trial runs of the experiment were carried out during which the relative

phases of pulses were adjusted using the spectrometer rf phase control knobs and the pulse durations were optimized by adjusting the potentiometer knob settings on the Nicolet-1180 computer which control the pulse lengths used by the computer program. The criterion for adjusting the phases and pulse lengths was the symmetry of the spin echoes displayed on an oscilloscope screen.

The second part of the experiment was carried out by measuring the effective relaxation time in the presence of a stationary field gradient. The field gradient was generated by passing current through a pair of copper coils mounted on the aluminum side plates on either side of the probe. The coils consisted of several turns of wire and were arranged so that the current flowed through the two coils in opposite directions. The current to the coils was supplied by a Union Carbide 6 volts No. MS31 cell, and was gated on or off under computer control in synchronization with the CPMG pulse sequence, using programmable level line 7 of the Nicolet 293A pulser.

The field gradient was calibrated using samples of distilled water and benzene whose diffusion constants were given in literature (118,119). The field gradient G (Gauss/cm) as a function of the current I (mA) passing through the coils, was obtained using

$$G = mI , \quad [6-4]$$

where $m = 0.155 \pm 0.005 \text{ Gauss cm}^{-1}\text{mA}^{-1}$. The CPMG experiment was first carried out in the absence of the field gradient to determine T_2 . $T_{2\text{eff}}$ was then obtained from the experiment done in the presence of field gradients, and fitting the data to Equation [6-2]. The field gradient was then calculated from the relation (Equations [6-2] and [6-3])

$$1/T_{2\text{eff}} = 1/T_2 + \gamma^2 G^2 D_t \tau^2 / 3 . \quad [6-5]$$

The field gradient G was determined for various values of current through the cells, and a calibration chart of field gradient against current was constructed. The current passing through the coils was measured with a Simpson digital multimeter model 461.

The effective relaxation time of hexamethyl phosphoramidate was then determined in the presence of the field gradient. From the value of $T_{2\text{eff}}$ the diffusion coefficient D_t was calculated by substituting the known values of T_2 into Equation [6-5]. The diffusion coefficient of hexamethylphosphoramidate was measured over a temperature range 300-440 K. The precision of this method of measurement was approximately $\pm 10\%$.

VI.6 Summary

A description of the experimental aspects of spin relaxation time determination was given in this chapter. The NMR spectrometer system used was described briefly. The spin lattice relaxation time was measured using two techniques: (i) inversion recovery experiment and (ii) triplet sequence. Both of the above methods were described briefly. It was followed by a discussion of the measurement of diffusion coefficient employing the stationary field gradient technique. Brief accounts of the field gradient coil calibration procedure, CPMG experiment and relevant equations were given. The results of the experiments and discussions concerning the separation of relaxation rates into contributions from the individual relaxation mechanisms are presented in the next chapter.

CHAPTER VII

RESULTS AND DISCUSSION

VII.1 Introduction

The results of the nuclear relaxation and diffusion experiments on HMPA and HMPD and the analysis of the data are presented in this chapter. Section VII.2 deals with the T_1 results for the ^{31}P nucleus in HMPD and the determination of the angular momentum correlation time. This is followed by the analysis of ^{14}N T_1 data in HMPA, in Section VII.3. Section VII.4 deals with the ^2H relaxation data analysis. The T_1 data for ^{31}P nuclei in HMPA, the translational diffusion coefficient results for HMPA, and the delineation of the contributions to the ^{31}P relaxation rate in HMPA are presented in Section VII.5. The conclusions derived from the study are presented in Section VII.6.

VII.2 ^{31}P T_1 (HMPD) Results and Analysis

The variation of the spin lattice relaxation time of

^{31}P in the deuterated analog (HMPD) with temperature was studied from 295 K to 460 K. The results are shown in Figure 38 and are tabulated in Table 2. The relaxation times were relatively long and the measurements were carried out using the triplet pulse sequence described in Chapter VI. The relaxation time at room temperature was approximately 48 sec and it decreased to about 12 sec at 460 K. To a good approximation, the ^{31}P relaxation in the deuterated compound can be considered to arise solely from the spin-rotation interaction, since the dipolar interaction between ^{31}P and ^2H would be relatively weak. The observed variation of the relaxation rate with temperature in Figure 38 shows the typical characteristic of spin-rotation relaxation: an increase in relaxation rate with increasing temperature. In order to obtain an approximate measure of the ^{31}P - ^2H dipolar contributions, a calculation using the reorientation correlation time from the ^2D relaxation rate (see Section VII.4) was carried out, which yielded a value of 370 sec for the dipolar T_1 at room temperature. The experimentally measured T_1 was approximately 48 sec at the same temperature. The contribution of ^{31}P - ^2H dipolar mechanism to the overall relaxation rate at room temperature, where the dipolar contribution is expected to be larger than at high temperatures, is only slightly larger than the uncertainty

Table 2
Relaxation Data and Results for ^{31}P in HMPD

Temp. (K)	T_1 obs. (sec)	τ_J obs. ($\times 10^{14}$ sec)	τ_J calc. ($\times 10^{14}$ sec)
294.8	48	4.3	4.1
300.6	42	4.9	4.3
312.6	40	5.0	4.8
313.0	38	5.0	4.8
327.2	39	4.8	5.3
327.8	37	5.0	5.4
333.2	33	5.7	5.6
340.2	32	5.7	5.8
350.1	29	6.0	6.2
359.2	26	6.5	6.6
369.2	25	6.6	7.0
370.5	25	6.7	7.0
384.5	20	7.8	7.6
385.4	21	7.6	7.6
400.2	18	8.4	8.2
406.8	18	8.2	8.5
409.9	17	8.9	8.6
420.4	16	9.1	9.0
425.1	15	9.5	9.2
430.4	15	9.4	9.5
445.7	13	10.6	10.1
450.5	13	10.3	10.3
460.9	12	11.1	10.7

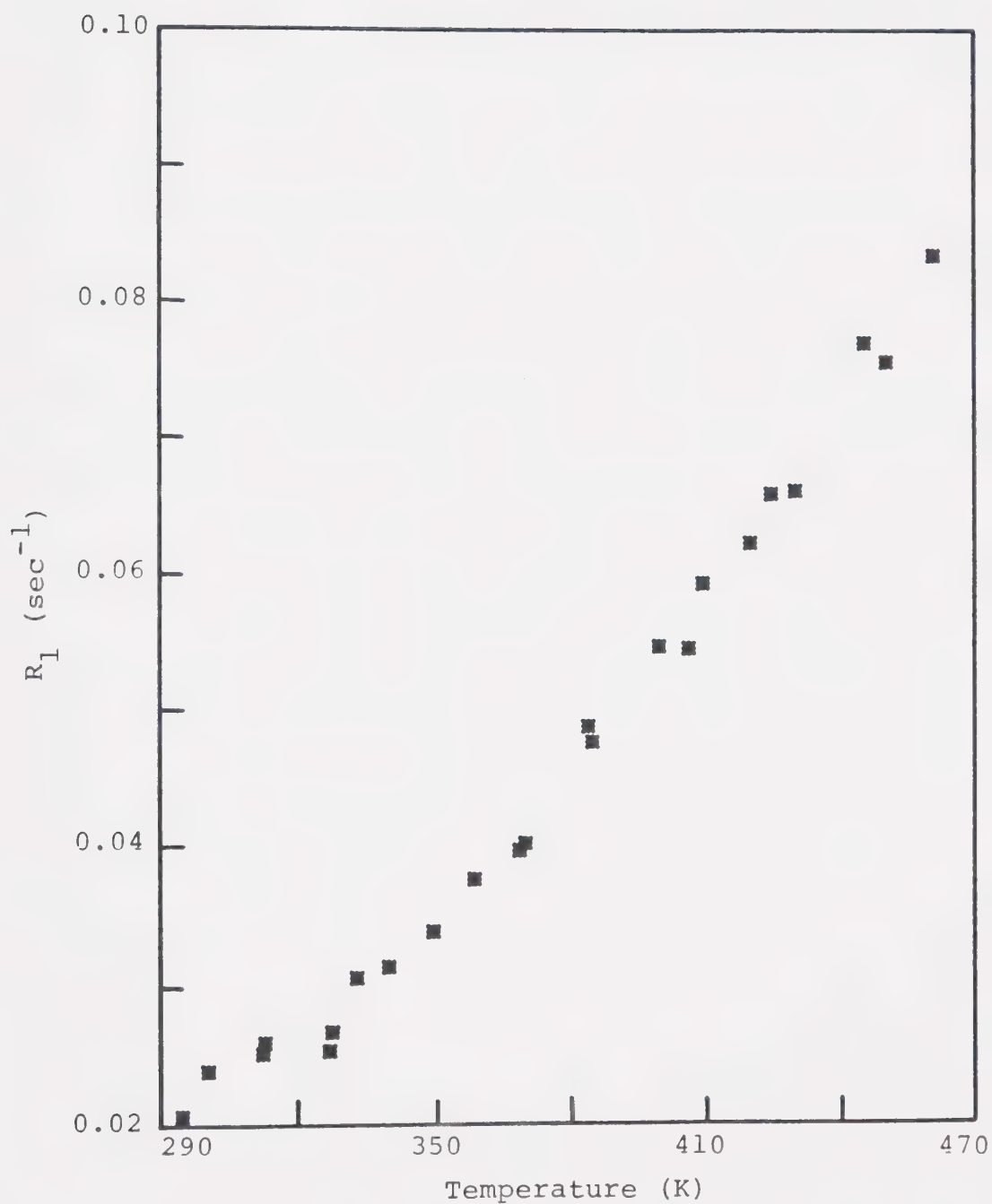


Figure 38. Observed relaxation rates of ^{31}P in HMPD. The T_1 relaxation times were measured with the triplet pulse sequence.

in the T_1 measurements. Similar calculations of the dipolar interactions with ^{14}N nuclei, yields a relaxation time of approximately 830 sec for ^{31}P nucleus at room temperature. Hence dipolar contributions to the ^{31}P relaxation in HMPD can be neglected.

It is possible to extract the angular momentum correlation time τ_J from the observed variation of ^{31}P T_1 values with temperature in the deuterated compound using Equation [5-11], provided that C_{\parallel} and C_{\perp} , the parallel and perpendicular components of the spin-rotation interaction tensor, and I_{\parallel} and I_{\perp} , the corresponding moments of inertia of HMPD are known. The moments of inertia I_{\parallel} and I_{\perp} of HMPD were determined from the x-ray crystal structure data reported by Le Carpentier, Schlupp and Weiss (120) for the compounds $\text{MoO}(\text{O}_2)_2\text{PO}[\text{N}(\text{CH}_3)_2]_3\text{H}_2\text{O}$ and $\text{MoO}(\text{O}_2)_2\text{PO}[\text{N}(\text{CH}_3)_2]_3\text{C}_5\text{H}_5\text{N}$. Average values of the bond lengths and bond angles in the two compounds, the C-H distance (1.101×10^{-8} cm) and the H-C-H tetrahedral angle ($109^\circ 28'$) were used in the calculation of moments of inertia. The average moments of inertia were calculated to be: $I_{\parallel} = 1.31 \pm 0.02 \times 10^{-37}$ g cm² and $I_{\perp} = 0.98 \pm 0.01 \times 10^{-37}$ g cm².

The components of the spin-rotation constant tensor were determined from ^{31}P chemical shifts utilizing the relationship between spin-rotation constants and the

paramagnetic part of the chemical shift (89). Flygare and Goodisman (121) have shown that the paramagnetic part of the chemical shift and the components of the spin-rotation tensor are related by

$$\sigma_{av} = \sigma_{av}^d(\text{free atom}) + \frac{|e|\hbar}{6mnc\mu_O g} (M_{xx}I_x + M_{yy}I_y + M_{zz}I_z) , \quad [7-1]$$

where σ_{av} is the average chemical shift, $\sigma_{av}^d(\text{free atom})$ is the free-atom diamagnetic susceptibility, e is the electron charge, m is the electron mass, c is the speed of light, μ_O is the nuclear magneton, g is the nuclear g -factor and M_{xx} , M_{yy} and M_{zz} are the components of the spin-rotation tensor (in ergs). The spin-rotation tensor C (in radians/sec) is related to M by $M = \hbar C$. Equation [7-1] can be rearranged to the form

$$C_{\alpha\alpha} = \gamma\hbar^2 [\sigma_{\alpha} - \sigma_{av}^d(\text{free atom})] / [\mu_e I_{\alpha}], \quad \alpha = x, y, z, \quad [7-2]$$

where γ is the nuclear magnetogyric factor and μ_e is the Bohr magneton ($\mu_e = |e|\hbar/[2mc]$).

The parallel and perpendicular components of the spin-rotation constant for HMPD, C_{\parallel} and C_{\perp} , where $C_{\parallel} = C_{zz}$ and $C_{\perp} = C_{xx} = C_{yy}$ can be determined from Equation [7-1]

if the anisotropic components of the chemical shift tensor, σ_{\parallel} and σ_{\perp} are known. The ^{31}P spectrum of solid HMPA at 77 K shown in Figure 39 was measured by Dr. J. Ripmeester at the National Research Council, Ottawa. The resonance frequency of ^{31}P was 72.87 MHz and the spectrum was measured with a sweep width of 125 KHz collected in a memory size of 512 points and zero filled to 4096 points before Fourier transformation. The delay between successive scans was 160 sec and four scans were co-added. The spectrum shows the anisotropic line shape resulting from a system with axial or near axial symmetry. The components of the chemical shift tensor σ_{\parallel} and σ_{\perp} were obtained by fitting the spectrum to an anisotropic line shape function with axial symmetry and Gaussian line broadening. The simulation was analogous to that for paramagnetic line shapes of polycrystalline substances reported by Ibers and Swalen (122), who used Lorentzian rather than Gaussian broadening. The chemical shift anisotropy was determined to be $\sigma_{\parallel} - \sigma_{\perp} = 163.8 \pm 0.1$ ppm. The average chemical shift of ^{31}P in HMPA with reference to PH_3 given by Pople et al. (123) and the chemical shift of PH_3 relative to the free phosphorous atom given by Davis et al. (124):

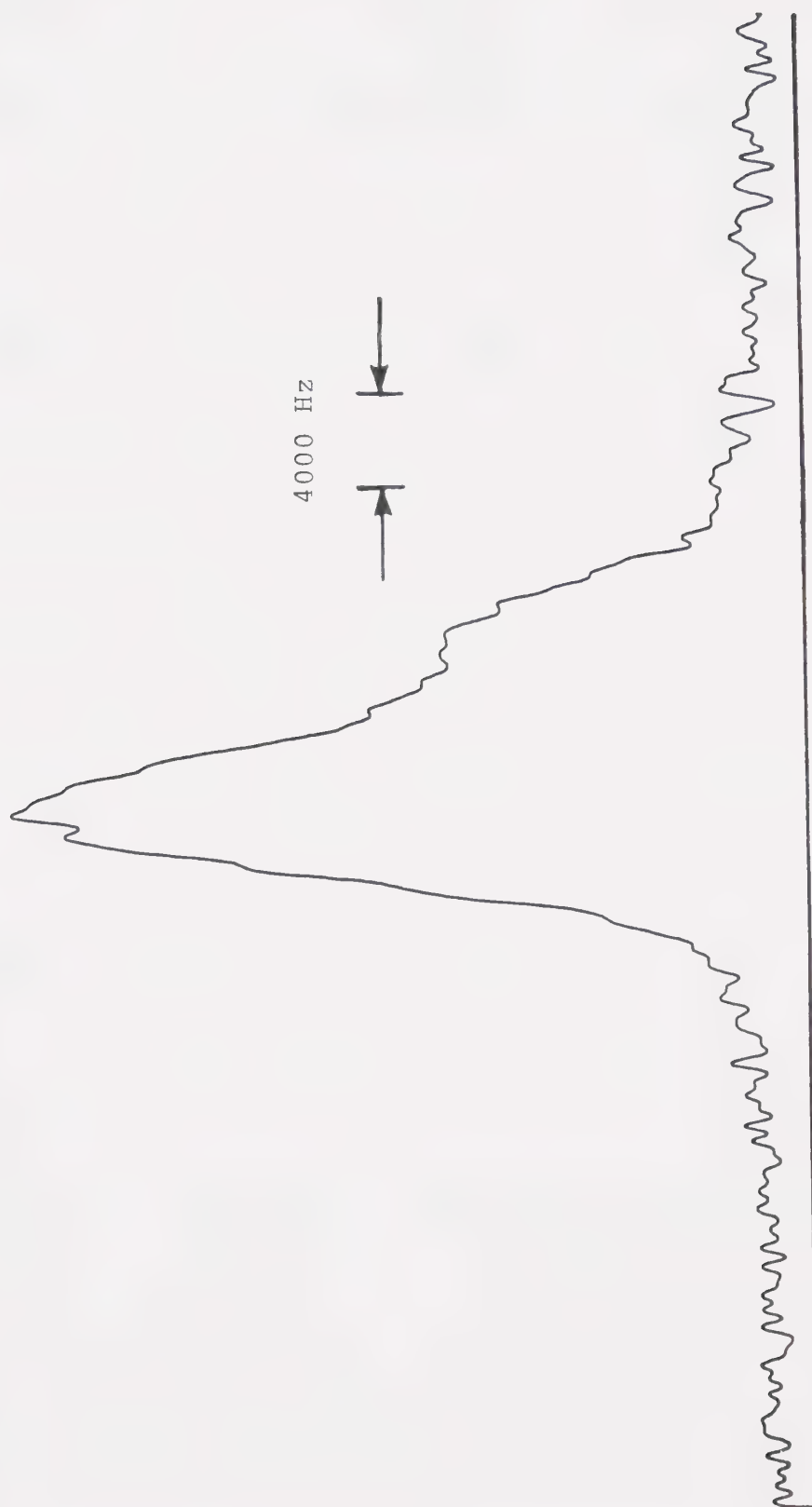


Figure 39. Observed ^{31}P spectrum of solid HMPD. The spectrum was obtained at 77 K. The resonance frequency was 72.87 MHz with a sweep width of 125 kHz collected over 512 data points and zero filled to 4096 points. The delay between experiments was 160 sec and 4 scans were co-added.

$$\sigma_{av}(HMPA) - \sigma_{av}(PH_3) = -261 \pm 1 \text{ ppm} ,$$

[7-3]

$$\sigma_{av}(PH_3) - \sigma_{av}^d(\text{free atom}) = -366.4 \pm 0.1 \text{ ppm}$$

give

$$\sigma_{av}(HMPA) - \sigma_{av}^d(\text{free atom}) = -628 \pm 1 \text{ ppm.} \quad [7-4]$$

Equation [7-4] and the measured chemical shift anisotropy in HMPA given by

$$\sigma_{\parallel}(HMPA) - \sigma_{\perp}(HMPA) = 163.8 \pm 0.1 \text{ ppm}$$

were used to obtain the components of the chemical shift tensor relative to free atom value as

$$\sigma_{\parallel}(HMPA) - \sigma_{av}^d(\text{free atom}) = -518 \pm 1 \text{ ppm} ,$$

[7-5]

$$\sigma_{\perp}(HMPA) - \sigma_{av}^d(\text{free atom}) = -682 \pm 1 \text{ ppm} .$$

Equation [7-5] and the calculated moments of inertia were substituted in Equation [7-2] to obtain

$$C_{xx,yy} = C_{\perp} = -1.44 \pm 0.01 \text{ KHz}$$

$$C_{zz} = C_{\parallel} = -0.82 \pm 0.01 \text{ KHz}$$

The angular momentum correlation time τ_J was determined from the ^{31}P relaxation rate using Equation [5-11] and the above values C_\perp , C_\parallel , I_\perp and I_\parallel . The values of τ_J , together with the values calculated from the least squares fit to the form

$$\tau_J = A_1 \exp(-B_1/T) , \quad [7-6]$$

are given in Table 2. The non-linear least squares program determined the fitting parameters to be:

$A_1 = 5.8 \pm 0.5 \times 10^{-13}$ sec and $B_1 = 780 \pm 30$ K. The value of τ_J at 300 K is 4.1×10^{-14} sec and it increased to 1.1×10^{-13} sec at 460 K.

VII.3 ^{14}N T_1 Results and Analysis

The variation of T_1 of the ^{14}N nuclei in HMPA was measured over the temperature range 300 K - 445 K. The T_1 experiments were carried out using the inversion recovery method described in Chapter VI. The experimental results are given in Table 3. The measured T_1 values showed a smooth increase with increasing temperature. The value at 300 K is 0.5 mS and it increases to about 2 mS at the highest temperature. Figure 40 shows the variation of

Table 3
Relaxation Data and Results for ^{14}N in HMPA

Temp. (K)	T_1 obs. (msec)	$\tau_{\text{eff}}^{\text{N}}$ obs. ($\times 10^{12}$ sec)	$\tau_{\text{eff}}^{\text{N}}$ calc. ($\times 10^{12}$ sec)
304.8	0.50	5.8	6.0
304.9	0.48	6.1	6.0
317.7	0.59	5.0	5.0
318.2	0.58	5.0	5.0
330.7	0.69	4.3	4.2
331.8	0.73	4.0	4.1
343.4	0.88	3.7	3.6
348.7	0.91	3.3	3.4
355.4	0.97	3.2	3.2
357.7	1.0	3.0	3.1
365.4	1.1	2.8	2.8
378.8	1.2	2.5	2.5
387.0	1.2	2.4	2.3
399.4	1.4	2.0	2.1
412.4	1.5	1.9	1.9
423.4	1.7	1.7	1.7
430.1	1.8	1.6	1.6
439.1	1.9	1.5	1.5
445.2	2.0	1.4	1.5

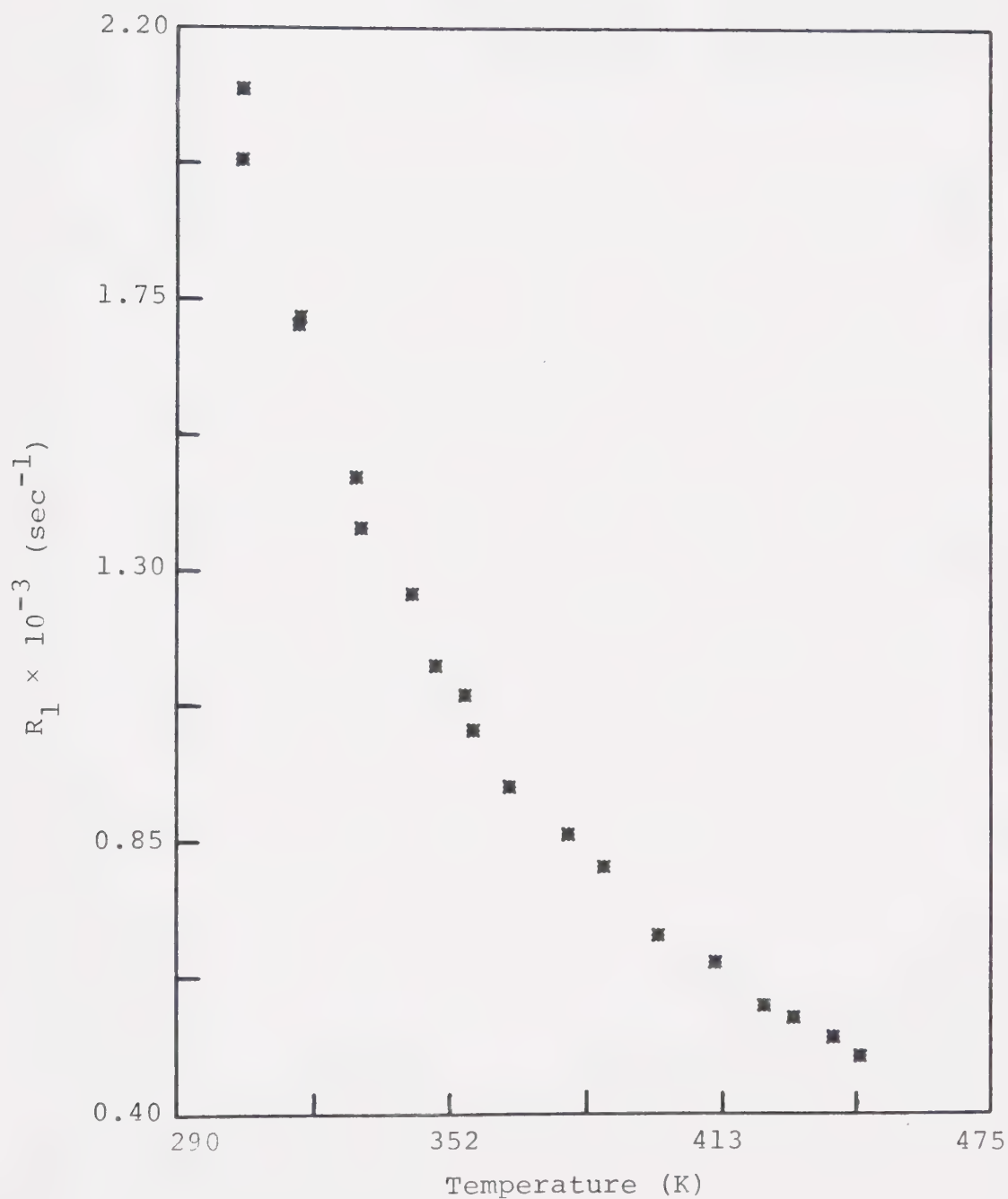


Figure 40. Observed relaxation rates of ^{14}N in HMPA. The T_1 relaxation times were measured using the inversion-recovery pulse sequence.

the ^{14}N relaxation rate R_1 with temperature. The smooth decrease of R_1 with temperature indicates that the quadrupolar relaxation mechanism dominates all other processes, as is typical for nuclei with quadrupole moments.

Since the quadrupolar relaxation process entirely dominates other relaxation mechanisms, the ^{14}N T_1 data provide a very convenient means for determination of the reorientational correlation time τ_θ . The temperature dependence of R_1 is due to that of τ_θ (Equation [5-12]). τ_θ can be easily determined from R_1 data if the nuclear quadrupolar coupling constant (e^2qQ/h) and the asymmetry parameter (η) are known. The quadrupole coupling constant and the asymmetry parameter were determined from the ^{14}N nuclear quadrupole resonance data reported by Krause and Whitehead (125). They have reported the temperature dependence of ^{14}N quadrupole resonance frequencies of HMPA over the temperature range from 77 K to 200 K. The quadrupole coupling constant and the asymmetry parameter were calculated at the melting point of HMPA using their relationships with observed nuclear quadrupole resonance frequencies (125). Two sets of ^{14}N quadrupole resonance frequencies are reported (125). The separation between these frequencies decreases with increasing temperature, but the lines do not coalesce below the melting point. It

was therefore concluded (125) that the frequency separation was due to crystallographically inequivalent nitrogen atoms, there being two inequivalent nitrogen lattice sites per unit cell in HMPA. The separation of resonance lines introduces some uncertainty into the calculations reported here. The average values of quadrupole coupling constant and asymmetry parameter evaluated from two sets of frequency data, were calculated. The average value of the quadrupole coupling constant e^2Qq/h was calculated to be 4.8 ± 0.2 MHz and the asymmetry parameter η to be 0.13 ± 0.01 .

The calculated values for the quadrupole coupling constant and the asymmetry parameter, along with the experimental R_1 values, were used in Equation [5-12] to obtain the reorientational correlation time τ_θ^N . These values are included in Table 3. The τ_θ^N values for various temperatures were fit into the equation

$$\tau_\theta^N = A_2 \exp(B_2/T) , \quad [7-7]$$

where A_2 and B_2 are fitting parameters. The non-linear least squares analysis yielded: $A_2 = 6.9 \pm 0.3 \times 10^{-14}$ sec and $B_2 = 1360 \pm 20$ K.

It is now appropriate to attempt a comparison of the observed variation of τ_θ^N with τ_J , with that predicted

using theoretical models for molecular reorientation. The relative magnitudes of the observed τ_{θ}^N (from ^{14}N data) and τ_J (from ^{31}P data in HMPD) are such that $\tau_{\theta}^N \gg \tau_J$ and hence these values correspond to rotational motion in the Debye limit (79,90). In this limit, the extended J-diffusion model (77,95-103) and the rotational Fokker-Planck-Langevin (FPL) model (78) give results which are identical to those given by Debye diffusion model (90). The investigated range of τ_{θ}^N and τ_J , does not extend into the transition region between the Debye limit and the dilute gas limit. It is in this transition region where a rigorous test of the validity of the extended J-diffusion and FPL models could be made. Hence the τ_{θ}^N and τ_J results obtained in this work do not afford an opportunity to test models for rotational motion in liquids.

The experimentally determined variation of τ_{θ}^N and τ_J has been compared with the variation predicted by the Hubbard relation (Equation [5-14]). The plots of the correlation times are shown in Figure 41. It is evident from Figure 41 that the observed variation of τ_{θ}^N with τ_J does not agree with the theoretical variation. The Hubbard relation predicts substantially larger values for τ_{θ} than those experimentally observed and the deviation of the experimental τ_{θ} values from the theoretical values becomes larger at higher temperatures. These deviations

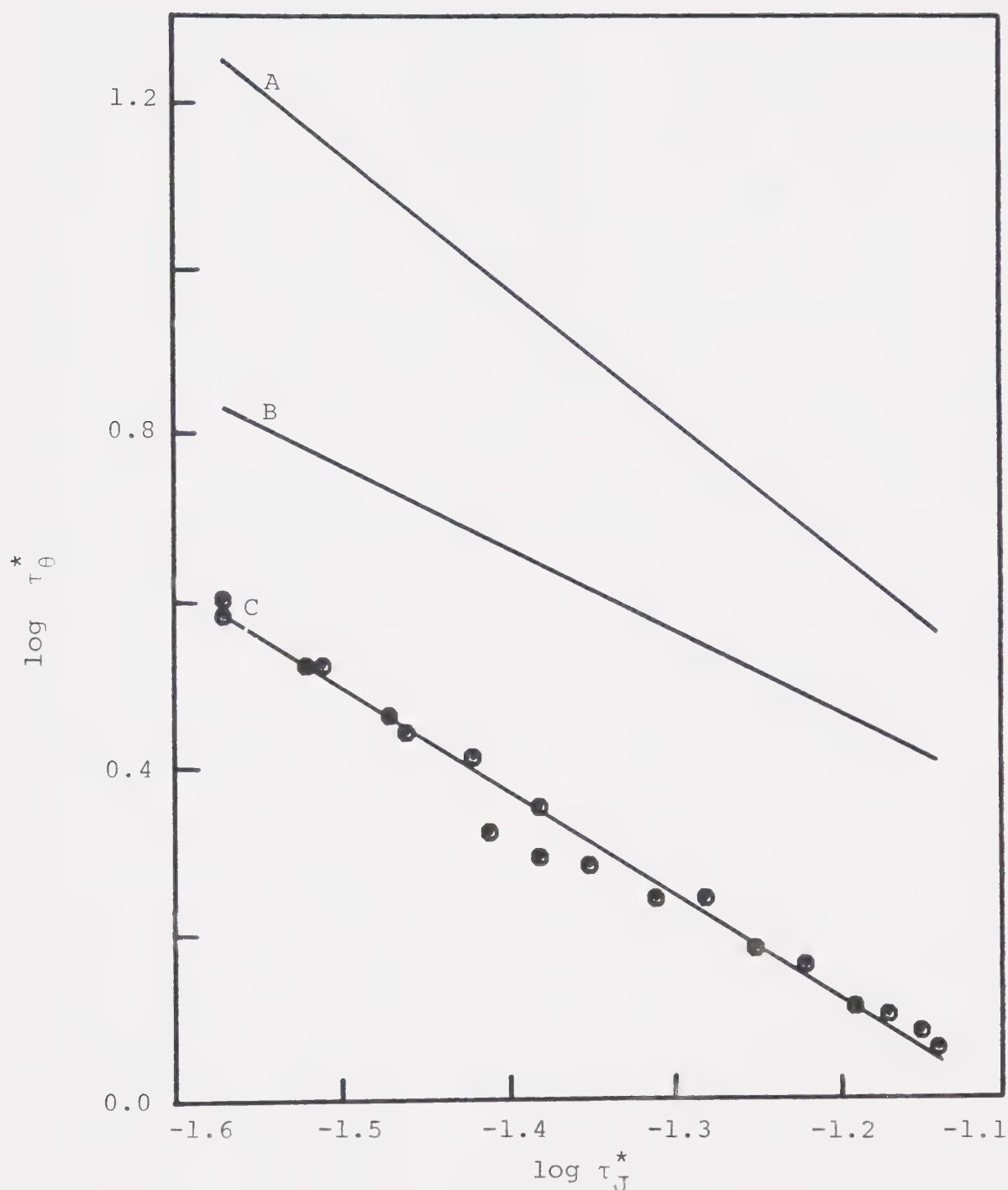


Figure 41. Variation of τ_θ with τ_J for HMPD. A, B and C represent $\log \tau_i^{*PN}$, $\log \tau_\theta^*$ and $\log \tau_{eff}^{*N}$ respectively. The asterisks denote reduced correlation times, for example, $\tau_J^* = (kT/I)^{1/2} \tau_J$. The experimentally observed variation is represented by dots.

are much larger than the uncertainties in τ_{θ}^N and τ_J due to experimental errors in the T_1 measurements and the uncertainties in the ^{14}N quadrupole constant and the ^{31}P spin rotation tensor. The increasing deviation with increasing temperature (larger τ_J values) suggests that the internal rotation process about the P-N bond must be taken into account in the theoretical model. Although the internal rotation about the P-N bond may be expected to possess a relatively large activation energy, it could affect the efficiency of ^{14}N relaxation in the high temperature range.

The reorientational correlation time τ_{θ}^N deduced from the ^{14}N data (Equation [7-7], Table 3) is therefore an effective correlation time (τ_{eff}^N) which is a function of the correlation time for molecular tumbling (τ_{θ}) and that for internal rotation about the P-N bond (τ_i^{PN}). The internal motion about the P-N bond is superimposed on the overall molecular tumbling. It is possible to isolate the internal motion about the P-N bond if it is assumed that the molecular reorientation of HMPA is described by the Hubbard relation (Equation [5-14]). The effective correlation time τ_{eff}^N for the case of isotropic reorientation is given by (73,126)

$$\tau_{\text{eff}}^{\text{N}} = A\tau_{\theta} + B\tau_{\theta}\tau_1^{\text{PN}}/(\tau_{\theta}+\tau_1^{\text{PN}}) \\ + C\tau_{\theta}\tau_1^{\text{PN}}/(4\tau_{\theta}+\tau_1^{\text{PN}}) , \quad [7-8]$$

where A, B and C are defined in Equation [5-8]. The angle Δ in Equation [5-8] in the case of quadrupolar relaxation corresponds to the angle between the internal rotation axis and the principal field gradient axis. The principal field gradient axis is assumed to lie along the nitrogen atom-lone pair direction and hence Δ is expected to be close to the tetrahedral angle. Equation [7-8] assumes that the internal motion and overall molecular tumbling are independent. The temperature dependence of the internal motion correlation time can be described by an equation of form

$$\tau_1^{\text{PN}} = A_3 \exp(B_3/T) , \quad [7-9]$$

where A_3 and B_3 are fitting parameters. The parameters A_3 and B_3 were determined by fitting the observed ^{14}N correlation times (Table 3) to Equation [7-8], and τ_{θ} was calculated from Hubbard relation (Equation [5-14]) with τ_{J} given by Equation [7-6]. The least squares analysis gave the following results: $A_3 = 1.2 \pm 0.2 \times 10^{-13}$ sec and

$B_3 = 1710 \pm 80$ K. Equation [7-9] shows the characteristic Arrhenius type variation and hence the energy barrier to internal rotation about the P-N bond can be extracted from it. The parameter B_2 corresponds to $\Delta E/R$ where ΔE is the internal rotation barrier and R is the gas constant. Hence the barrier to internal rotation has been calculated to be 3.4 ± 0.2 kcal/mole. No data on activation energies for the hindered rotation about P-N bonds are available in the literature for HMPA in liquid state, but P-N rotation barrier in solid HMPA has been estimated to be 6 kcal/mole by Andreeva et al. (127) from studies of ^{14}N nuclear quadrupole resonance. The energy barrier in liquid HMPA can be expected to be lower than the value estimated in the solid (127).

VII.4 ^2H T_1 Results and Analysis

The T_1 relaxation times of ^2H nuclei in the deuterated analog (HMPD) were studied as a function of temperature. The ^2H T_1 values were measured using the inversion recovery sequence over the temperature range 250-410 K. The relaxation time at 250 K was 0.40 sec and it increased to 3.3 sec at 410 K. The Experimental results are shown in Table 4. Figure 42 shows the variation of the relaxation rate R_1 with temperature.

Table 4
Relaxation Data and Results for ^2H Nucleus

Temp.	T_1 obs.	$\tau_{\text{eff}}^{\text{D}}$ obs.	$\tau_{\text{eff}}^{\text{D}}$ calc.	$\tau_{\text{i}}^{\text{CN}}$ calc.
(K)	(sec)	($\times 10^{12}$ sec)	($\times 10^{12}$ sec)	($\times 10^{12}$ sec)
253.7	0.40	6.1	5.8	19
264.4	0.53	4.6	4.7	15
274.5	0.64	3.8	3.9	12
283.2	0.74	3.3	3.3	10
290.8	0.87	2.8	2.9	9.0
295.2	0.92	2.7	2.7	8.3
309.4	1.1	2.2	2.2	6.6
316.0	1.2	2.0	2.0	5.9
328.7	1.4	1.7	1.7	4.9
340.2	1.7	1.5	1.5	4.2
349.7	1.9	1.3	1.3	3.7
358.6	2.0	1.2	1.2	3.4
366.8	2.2	1.1	1.1	3.1
376.5	2.4	1.0	0.99	2.8
387.8	2.8	0.88	0.89	2.5
397.8	3.3	0.75	0.81	2.2
408.2	3.3	0.75	0.74	2.0

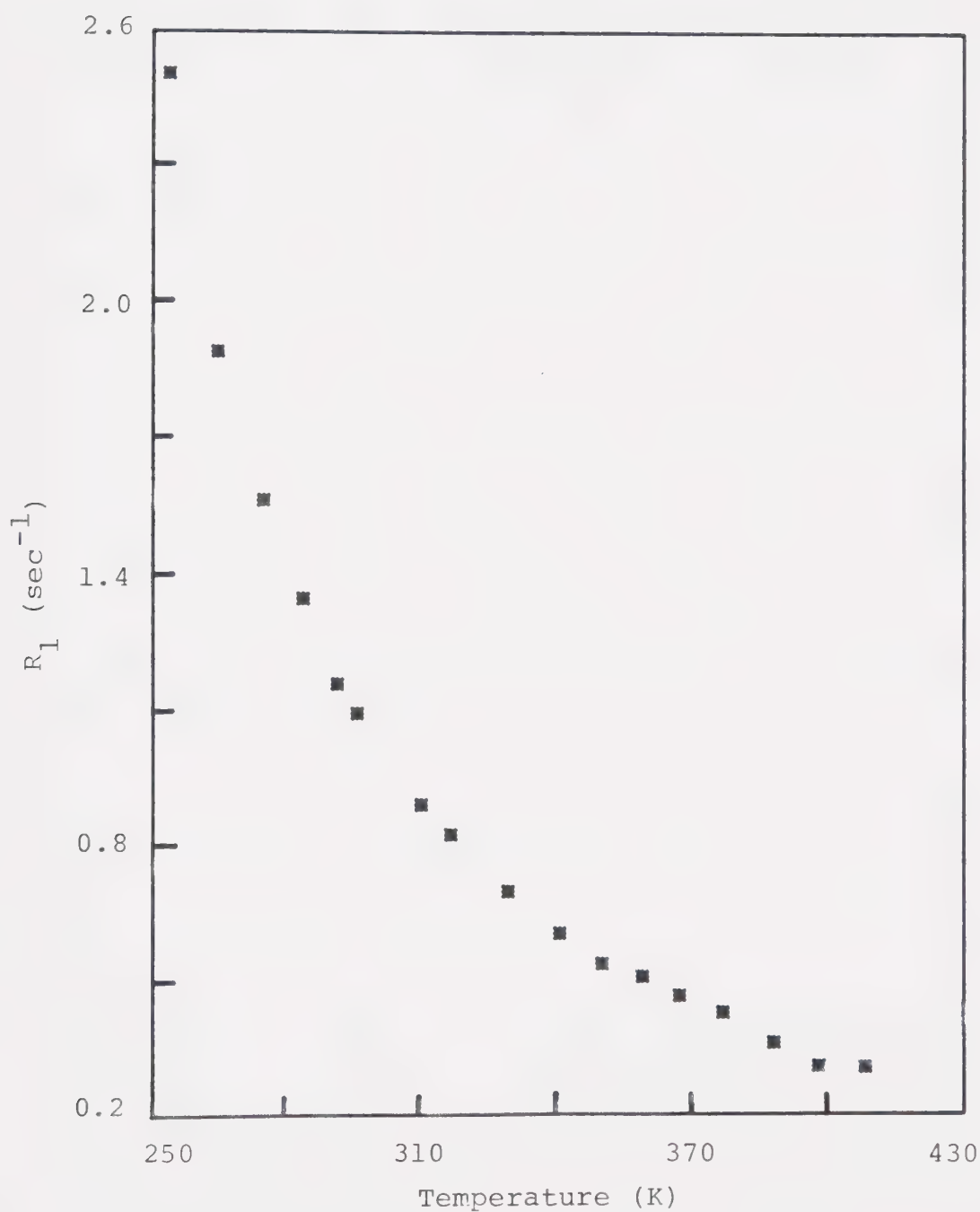


Figure 42. Observed relaxation rates of ^2H in HMPD. The T_1 relaxation times were measured with the inversion-recovery pulse sequence.

The ^2H relaxation in HMPD can be assumed to be entirely due to motional modulation of quadrupolar interactions. The quadrupolar relaxation rate of deuterium in the CD_3 group in HMPD is governed by three correlation times: (1) that due to molecular tumbling (τ_θ), (2) that due to internal rotation about P-N bond (τ_1^{PN}), and (3) that due to internal rotation about the C-N bond (τ_1^{CN}). The internal rotation about the P-N bond is superimposed on the molecular tumbling motion to yield the effective correlation time $\tau_{\text{eff}}^{\text{N}}$ discussed in Section VII.3. The internal motion of the CD_3 group is superimposed on $\tau_{\text{eff}}^{\text{N}}$ to give a third correlation time $\tau_{\text{eff}}^{\text{D}}$ which governs the time dependence of the ^2H quadrupolar interaction. Since all three motions are independent of each other, $\tau_{\text{eff}}^{\text{D}}$ can be written as

$$\begin{aligned} \tau_{\text{eff}}^{\text{D}} = & A' \tau_{\text{eff}}^{\text{N}} + B' \tau_{\text{eff}}^{\text{N}} \tau_1^{\text{CN}} / (\tau_{\text{eff}}^{\text{N}} + \tau_1^{\text{CN}}) \\ & + C' \tau_{\text{eff}}^{\text{N}} \tau_1^{\text{CN}} / (4 \tau_{\text{eff}}^{\text{N}} + \tau_1^{\text{CN}}) , \end{aligned} \quad [7-10]$$

where $\tau_{\text{eff}}^{\text{N}}$ is given by Equation [7-8] and A' , B' and C' are analogous to A , B and C respectively, in Equation [5-8]. In the definitions of A' , B' and C' , the angle variable is denoted by Δ' and is the angle between the internal rotation axis (the C-N bond) and principal axis

of the deuterium field gradient tensor (the C-D bond). Hence Δ' is the tetrahedral angle $109^\circ 28'$. The relaxation of the ^2H nuclei in HMPD thus provides an interesting case where the relaxation interaction is modulated by a time dependence characterized by three correlation times.

The quadrupolar relaxation rate in the presence of internal motion is obtained from Equation [5-12] by replacing τ_θ by $\tau_{\text{eff}}^{\text{D}}$. The deuterium quadrupole coupling in HMPD has not been reported, so we have assumed that the observed value, 166 ± 10 KHz (128), for the CD_3 deuterium quadrupole coupling constant in methylamine would provide an accurate estimate for the HMPD molecule. The value of e^2Qq/h for D in CD_3 group varies from 180 ± 5 KHz in CD_3I (129) to 133 ± 7 KHz in CD_3F (130) and the variation is related to the electronegativity of the group attached to the CD_3 group (131). Hence CD_3NH_2 seemed the logical molecule to use in estimating e^2Qq/h for D in HMPD. The asymmetry parameter η for deuterium in CD_3 group is very close to zero due to the cylindrical symmetry of the electric field gradient and can be dropped to a good approximation (132). Hence the relaxation rate expression (Equation [5-12]) reduces to

$$R_1 = \frac{3}{8} \left(\frac{e^2qQ^2}{h} \right)^2 \tau_{\text{eff}}^{\text{D}} \quad . \quad [7-11]$$

The deuterium T_1 data (Table 4) were analyzed to yield the effective correlation time $\tau_{\text{eff}}^{\text{D}}$ which is also given in Table 4.

The effective correlation time $\tau_{\text{eff}}^{\text{N}}$ appearing in Equation [7-10] was determined from the ^{14}N data in Section VII.3. The temperature dependence of the internal rotation correlation time was assumed to have the form

$$\tau_1^{\text{CN}} = A_4 \exp(B_4/T) , \quad [7-12]$$

where A_4 and B_4 are fitting parameters. The observed deuterium correlation times ($\tau_{\text{eff}}^{\text{D}}$) (Equation [7-11]) were fit to Equation [7-10] using Equations [7-8], [7-9], [7-12] and the Hubbard model. Fixing A_3 and B_3 at the values obtained from least squares analysis (Section VII.3), the best fit values for A_4 and B_4 were determined. The non-linear least squares analysis gave the following results: $A_4 = 5.1 \pm 0.7 \times 10^{-14}$ sec and $B_4 = 1500 \pm 40$ K. The barrier to the rotation of the CD_3 group in HMPD was determined from the parameter B_4 to be 3.0 ± 0.1 kcal/mole. This compares favourably with the set of methyl rotation barrier values for various organic molecules compiled by Lambert et al. (81), for example, 2.9 kcal/mole in 1,1,1-trichloroethane [CH_3CCl_3] and 3.5

kcal/mole in tertiarybutylchloride $[(CH_3)_3CCl]$ (133,134). Andreeva et al. (127) have reported the CH_3 rotational barrier in solid HMPA to be 2 kcal/mole, but have stressed that their work gives a lower bound.

VII.5 ^{31}P T_1 (HMPA) Results and Analysis

The longitudinal relaxation times of ^{31}P in HMPA were measured over the temperature range 299 K to 460 K. T_1 measurements were carried out using the inversion recovery sequence described in Chapter VI. The experimental results are shown in Figure 43 and Table 5. The T_1 value at 296 K was 18 sec which increased to a maximum of 20 sec at 311 K and then decreased steadily to 10 sec at 461 K. The occurrence of a maximum in the temperature variation of T_1 indicates the presence of two competing relaxation mechanisms: the spin rotation and dipolar contributions, which have complimentary temperature dependence. The total relaxation rate can be written as

$$R_1 = R_{1SR} + R_{1intraDD} + R_{1interDD} , \quad [7-13]$$

where R_{1SR} , $R_{1intraDD}$ and $R_{1interDD}$ are given by Equations [5-11], [5-8] and [5-9] respectively. The spin rotation relaxation rate increases with increasing temperature

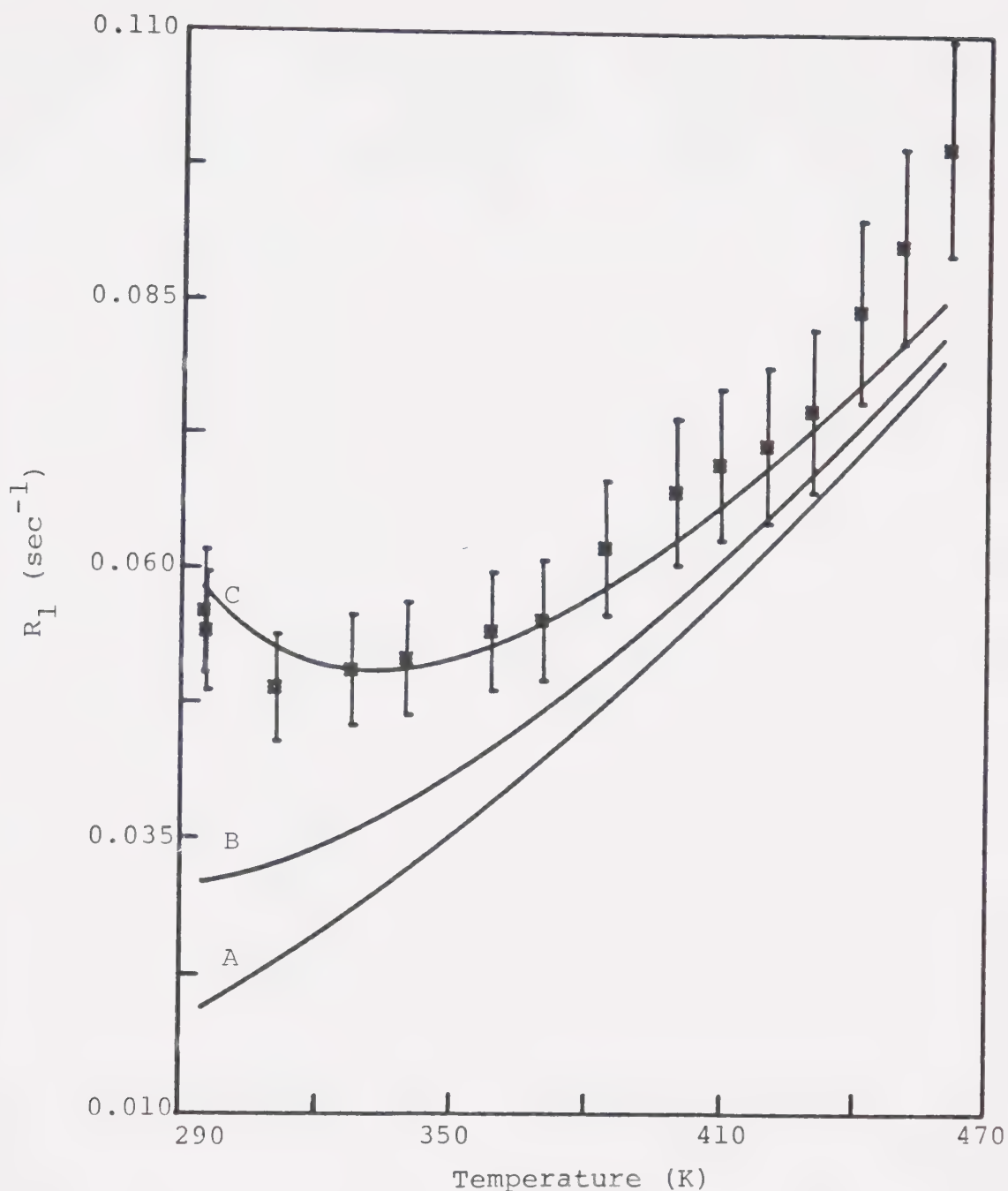


Figure 43. Comparison of calculated and observed ^{31}P relaxation rates in HMPA. The asterisk points show the observed T_1 relaxation rates with $\pm 10\%$ error bounds. The solid lines denote the calculated relaxation rates: curve A represents the spin-rotation relaxation rate; curve B represents the sum of spin-rotation and intramolecular dipolar relaxation rates; and curve C represents the sum of spin-rotation, intramolecular and intermolecular dipolar relaxation rates.

Table 5
Relaxation Data for ^{31}P in HMPA

Temp. (K)	T_1 (sec)
295.0	18
295.6	18
311.0	20
327.8	20
340.2	19
359.2	18
370.5	18
384.5	16
400.2	15
409.9	14
420.4	14
430.4	13
441.2	12
450.5	11
460.9	10

while the intramolecular and intermolecular dipolar relaxation rates decrease with increasing temperature, but at different rates. An attempt was made to delineate the contributions due to spin-rotation, inter- and intramolecular dipolar interactions over the temperature range studied. To attain this objective, the individual relaxation rates were computed using parameters determined from the analysis of ^{14}N , ^2H and ^3P in HMPD data in previous sections. The correlation times $\tau_{\text{eff}}^{\text{N}}$ and $\tau_{\text{i}}^{\text{CN}}$ obtained from the ^{14}N and ^2H data were used to compute the R_{lintra} term. The angular momentum correlation time τ_{J} determined from ^3P in HMPD was used to calculate R_{ISR} . The translational diffusion coefficients which were measured over the entire temperature range were used in the calculation of R_{inter} .

a. Calculation of Spin-Rotation Relaxation Rates

Equation [5-11] was employed to calculate the spin-rotational contribution to the total relaxation rate. The moments of inertia were calculated as described in Section VII.4 using crystallographic data (120). The following moments of inertia were obtained: $I_{\parallel} = 1.08 \pm 0.02 \times 10^{-37}$ g cm² and $I_{\perp} = 0.81 \pm 0.01 \times 10^{-37}$ g cm². The components of the spin-rotation tensor were evaluated using Equation [7-2], with the results: $C_{\parallel} = -0.99 \pm 0.02$ KHz and

$C_{\perp} = -1.74 \pm 0.02$ KHz. The angular momentum correlation time τ_J in HMPA was assumed to be equal to that in HMPD. This should prove to be a reasonable assumption since their moments of inertia are quite similar. The contribution R_{1SR} to the total relaxation rate was then calculated using Equation [5-11]. The results are given in Table 6.

b. Calculation of Intermolecular Dipolar Relaxation Rates

The translational diffusion coefficient D_t of HMPA was measured using the stationary field gradient technique described in Chapter VI. The experimental results are given in Table 7. The diffusion coefficient at 304 K is $3.8 \times 10^{-6} \text{ cm}^2\text{sec}^{-1}$ and it increases to $2.3 \times 10^{-5} \text{ cm}^2\text{sec}^{-1}$ at 450 K. The experimental data were fit to the equation

$$D_t = A_5 \exp(B_5/T) , \quad [7-14]$$

where the fitting parameters A_5 and B_5 were determined to be: $A_5 = 1.2 \pm 0.2 \times 10^{-3} \text{ cm}^2\text{sec}^{-1}$ and $B_5 = -1740 \pm 50$ K. Equation [5-9] was used to compute $R_{1interDD}$. The factor a in Equation [5-9] represents the hydrodynamic radius of HMPA, i.e. the effective radius of the HMPA molecule if the molecule is assumed to be spherical in shape and to be

Table 6

Comparison of Calculated and Observed ^1H Relaxation Rates in HMPA

Temp. (K)	$R_{\text{ISRcalc.}}$ (sec^{-1})	$R_{\text{IDDIntracalc.}}$ (sec^{-1})	$R_{\text{IDDIntercalc.}}$ (sec^{-1})	$R_{\text{ITotalcalc.}}$ (sec^{-1})	$R_{\text{I obs.}}$ (sec^{-1})
295.0	0.020	0.012	0.027	0.058	0.056
295.5	0.020	0.012	0.027	0.058	0.054
310.9	0.024	0.0091	0.020	0.053	0.049
327.8	0.029	0.0073	0.015	0.051	0.051
340.1	0.032	0.0062	0.012	0.051	0.052
359.1	0.039	0.0050	0.0095	0.053	0.054
370.4	0.042	0.0045	0.0082	0.055	0.056
384.4	0.048	0.0039	0.0069	0.058	0.062
400.1	0.054	0.0034	0.0058	0.063	0.068
409.9	0.058	0.0031	0.0052	0.066	0.070
420.4	0.062	0.0029	0.0047	0.070	0.072
430.4	0.066	0.0027	0.0042	0.073	0.075
441.1	0.071	0.0025	0.0038	0.077	0.084
450.4	0.075	0.0023	0.0035	0.081	0.090
460.9	0.080	0.0022	0.0032	0.086	0.100

Table 7

Translational Diffusion Coefficients of HMPA

Temp (K)	D obs. ($\times 10^6 \text{ cm}^2 \text{ sec}^{-1}$)	D l.s.fit ($\times 10^6 \text{ cm}^2 \text{ sec}^{-1}$)
304.2	3.9	4.0
309.4	4.4	4.4
318.6	5.1	5.2
329.0	6.2	6.2
341.4	7.6	7.5
351.0	7.6	8.6
355.0	8.9	9.1
357.2	10	9.3
361.2	11	9.9
369.9	13	11
381.4	12	13
391.2	14	14
402.0	16	16
410.2	18	18
421.0	22	20
430.4	21	21
440.0	23	23
449.6	23	26

immersed in a continuous viscous medium. The hydrodynamic radius was taken to be 4×10^{-8} cm. The calculated $R_{1interDD}$ values are given in Table 6.

c. Calculation of the Intramolecular Dipole Relaxation Rates

The intramolecular dipolar relaxation rates were calculated taking into account the effects of internal motion of methyl groups superimposed on the overall molecular reorientation. It has been shown (135) that when internal rotation modulates the internuclear separation, the intramolecular dipolar relaxation rates can be affected in certain molecular geometries. Hence in such cases, Equation [5-8] which does not take into account the modulation of internuclear distance, does not adequately determine the relaxation rate. In the work (135) mentioned above, the internuclear distance term appearing in the correlation functions, was expressed as a function of the internal rotation angle and the correlation functions were evaluated (135) assuming that a rotational diffusion model describes both internal and overall molecular rotation. The spectral density functions resulting from these correlation functions were substituted in Equation [5-5] to give the relaxation rate expression [Equation [11] of Reference (135)] for dipolar

relaxation with modulation of the internuclear distance by internal rotation.

In HMPA, the ^{31}P - ^1H internuclear separation is modulated by rotation of the methyl groups. Hence the approach described above was employed for the calculation of R_{lintraDD} . The effective reorientational correlation time $\tau_{\text{eff}}^{\text{N}}$ determined from the ^{14}N data in Section VII.3 and the internal rotation correlation time τ_1^{CN} obtained from the analysis of the ^2H data in Section VII.4, were substituted in Equation [11] of Reference (135) to evaluate the R_{lintraDD} term. The results are given in Table 6.

d. Comparison of Calculated and Experimental Relaxation Rates

The calculated values for spin-rotation, inter- and intramolecular dipolar relaxation rates along with the experimental relaxation rates of ^{31}P in HMPA are given in Table 6. Graphical illustration of the data in Table 6 is shown in Figure 43. At 311 K, the spin-rotation mechanism contributes approximately 48% of the total relaxation rate while the inter- and intramolecular dipolar rates are approximately 41% and 19% respectively. Although the calculated relaxation rate is only grossly consistent with the experimental value at 311 K, it exhibits a reassuring

feature: the contribution of dipolar relaxation mechanisms and spin-rotation mechanisms are approximately equal at the minimum in the plot of relaxation rate with temperature (136). The calculations (Table 6) show that the spin-rotation contribution is 48% at 311 K which is approximately the temperature at which the experimental plot shows a minimum (Figure 43). The spin-rotation contribution increases to about 80% at 400 K while the inter- and intramolecular dipolar contributions decrease to about 9% and 5% respectively. At 461 K the spin-rotation interaction contributes approximately 81% of the total relaxation rate and the dipolar mechanisms account for about 6% of the total rate. Although the calculated relaxation rates do not agree with experimental rates in a rigorous quantitative manner, the delineation of the contributions of various relaxation mechanisms remains valid considering the limits of experimental errors and the various approximations used.

Another interesting feature which emerges from Table 6 is that the intermolecular dipolar relaxation rates are larger than the intramolecular dipolar rates. Although this result seems surprising, it can be rationalized when the implications of the internal rotation of methyl groups are recognized. It has been shown (137) that the effect of internal motion is most pronounced when the internal

rotation correlation time τ_1^{CN} and the overall reorientational correlation time τ_θ are comparable. In HMPA, τ_1^{CN} and τ_θ correlation times are comparable (Equations [7-7] and [7-12]) and hence the internal motion can be expected to alter the intramolecular dipolar contribution when compared with situations where internal motion is absent or when τ_1^{CN} is different from τ_θ by several orders of magnitude.

VII.6 Conclusions

The work described in Chapters V, VI and VII of this thesis demonstrates the use of relaxation data for the various nuclei to obtain an overall picture of the molecular motion in HMPA.

The study of ^{31}P relaxation in the deuterated compound (HMPD) has yielded the angular momentum correlation times τ_J . The study of the deuterated form of the molecule has been useful in isolating the spin-rotation interaction of the ^{31}P nucleus.

From the ^{14}N data analysis, it has been found that the effective correlation time for reorientation is a function of the molecular tumbling correlation time and that for internal motion about the P-N bond. It was found that the inclusion of the internal motion about the P-N

bond was essential for agreement between the experimental variation of τ_{θ}^N with τ_J , and the corresponding variation predicted by the Hubbard relation. The internal rotation about the P-N bond was found to be quite hindered, with an activation energy of 3.4 ± 0.2 kcal/mole. The internal rotation correlation time τ_i^{PN} was about 5 times larger than the correlation time for molecular tumbling τ_{θ} (given by the Hubbard relation) at room temperature. At 450 K this ratio decreased to about 1.4. Thus at high temperatures the internal motion time scale was comparable to that for molecular tumbling and hence altered the effective reorientation correlation time τ_{eff}^N significantly.

The relative magnitude of τ_{θ} and τ_J was such that $\tau_{\theta} \gg \tau_J$, which is the Debye limiting situation. In the Debye limit, the results from various models for molecular reorientation, such as the J-diffusion model (77,95-103) and the Fokker-Planck-Langevin model (78), essentially reduce to those given by the Hubbard relation. The applicability of models for molecular reorientation can only be tested using the results at the transition stage between the Debye limit and the dilute gas limit. Hence it was not possible to test the validity of the J-diffusion or FPL models from the results on HMPA obtained in this work.

The relaxation study of ^2H in HMPD provided an interesting situation where the effective correlation time was affected by three types of motion: (1) overall molecular tumbling, (2) internal motion about the N-P bond and (3) internal motion of the CD_3 groups. It was found that the rotation of CD_3 groups was also relatively hindered with an activation energy of 3.0 ± 0.1 kcal/mol. This result seems to be in the correct range when compared with the results in the literature for activation energies for rotation of methyl groups. A comparison of the relative magnitudes of the correlation times, give the ratio of $\tau_1^{\text{PN}}:\tau_0:\tau_1^{\text{CN}}$ to be 40:15:1 at room temperature. At 450 K this ratio becomes approximately 30:20:1. The relative ratio of each internal correlation time to τ_0 is such that the effect of each internal motion process on the overall motion is appreciable.

It has been possible to delineate the individual contributions to ^{31}P relaxation in HMPA at various temperatures. The separation of the contributions was carried out by calculating the relaxation rates due to various mechanisms, using results derived from the analysis of ^{31}P in HMPD, ^{14}N and ^2H data. It was found that at about 311 K the spin-rotation and the total dipolar contributions were approximately equal at higher temperatures, the spin-rotation contribution became much

more dominant and accounted for most of the relaxation rate at 460 K. Another interesting observation was that the contribution of intermolecular dipolar interactions was larger than the intramolecular dipolar component. This can be rationalized on the basis that the internal motion of methyl groups, with correlation time comparable to that for molecular tumbling, reduces the effective spectral density and hence makes the intramolecular dipolar relaxation rate smaller than one would find in the absence of internal rotation.

VII.7 Summary

The results of the relaxation rate studies in HMPA and the data analysis were presented in this chapter. The use of ^{31}P T_1 values in HMPD to obtain angular momentum correlation time was described. The analysis of ^{14}N data to yield the correlation times for reorientation and internal motion about the N-P bond was presented. It was followed by ^2H data analysis yielding the correlation time for internal rotation of methyl groups. The delineation of contributions to the relaxation rate of ^{31}P in HMPA was discussed. Finally, the conclusions derived from this study were presented.

REFERENCES

1. C.P. Slichter, "Principles of Magnetic Resonance", 2nd Ed., Springer-Verlag, Berlin, 1978.
2. R.M. Lynden-Bell, Prog. NMR Spectrosc., 2, Chapter 4, 163 (1967).
3. T.C. Farrar and E.D. Becker, "Pulse and Fourier Transform NMR", Academic Press, New York, 1971.
4. A. Carrington and A.D. McLachlan, "Introduction to Magnetic Resonance", John Wiley and Sons, Inc., New York, 1967.
5. A.G. Redfield, IBM J. Res. Develop., 1, 19 (1957).
6. C.S. Johnson, Adv. Magn. Reson., 1, 33 (1965).
7. G. Bodenhausen, Prog. NMR Spectrosc., 14, 137 (1981).
8. J. Jeener, Ampere International Summer School, Basko Polje, Yugoslavia (1971), unpublished.
9. R. Freeman and G.A. Morris, Bull. Magn. Reson., 1, 5 (1979).
10. A. Bax, "Two Dimensional Nuclear Magnetic Resonance In Liquids", D. Reidel Publishing Company, Holland, 1982.
11. G. Bodenhausen, R. Freeman, R. Niedermeyer and D.L. Turner, J. Magn. Reson., 26, 133 (1977).

12. W.P. Aue, E. Bartholdi and R.R. Ernst, J. Chem. Phys., 64, 2229 (1976).
13. L. Muller, A. Kumar and R.R. Ernst, J. Chem. Phys., 63, 5490 (1975).
14. W.P. Aue, J. Karhan and R.R. Ernst, J. Chem. Phys., 64, 4226 (1976).
15. G. Bodenhausen, R. Freeman and D.L. Turner, J. Chem. Phys., 65, 839 (1976).
16. A.A. Maudsley and R.R. Ernst, Chem. Phys. Lett., 50, 368 (1977).
17. A.A. Maudsley, L. Muller and R.R. Ernst, J. Magn. Reson., 28, 463 (1977).
18. G. Bodenhausen and R. Freeman, J. Magn. Reson., 28, 471 (1977).
19. A. Bax and G.A. Morris, J. Magn. Reson., 42, 501 (1981).
20. K. Nagayama, K. Wuthrich and R.R. Ernst, Biochem. Biophys. Res. Commun., 90, 305 (1979).
21. A. Bax, R. Freeman and G.A. Morris, J. Magn. Reson., 42, 164 (1981).
22. K. Nagayama, A. Kumar, K. Wuthrich and R.R. Ernst, J. Magn. Reson., 40, 321 (1980).
23. G. Wagner, A. Kumar and K. Wuthrich, Eur. J. Biochem., 114, 375 (1981).

24. S. Macura and R.R. Ernst, *J. Magn. Reson.*, 43, 259 (1981).
25. A. Kumar, G. Wagner, R.R. Ernst and K. Wuthrich, *J. Am. Chem. Soc.*, 103, 3654 (1979).
26. B.H. Meier and R.R. Ernst, *J. Am. Chem. Soc.*, 101, 6441 (1979).
27. J. Jeener, B.H. Meier, P. Bachmann and R.R. Ernst, *J. Chem. Phys.*, 71, 4546 (1979).
28. U. Piantini, O.W. Sorenson and R.R. Ernst, *J. Am. Chem. Soc.*, 104, 6800 (1982).
29. A.J. Shaka and R. Freeman, *J. Magn. Reson.*, 51, 169 (1981).
30. M.H. Levitt and R.R. Ernst, *Chem. Phys. Lett.*, 100, 119 (1983).
31. D.M. Doddrell, D.T. Pegg and M.R. Bendall, *J. Magn. Reson.*, 48, 323 (1982).
32. P. Meakin and J.P. Jesson, *J. Magn. Reson.*, 10, 290 (1973).
33. P. Meakin and J.P. Jesson, *J. Magn. Reson.*, 11, 182 (1973).
34. P. Meakin and J.P. Jesson, *J. Magn. Reson.*, 13, 354 (1974).
35. P. Meakin and J.P. Jesson, *J. Magn. Reson.*, 18, 411 (1975).
36. A.D. Bain, *J. Magn. Reson.*, 39, 335 (1980).

37. A.D. Bain, J. Bornais and S. Brownstein, Can. J. Chem., 59, 723 (1981).
38. A.D. Bain, private communication.
39. O.W. Sorenson and R.R. Ernst, J. Magn. Reson., 51, 477 (1983).
40. O.W. Sorenson, G.W. Eich, M.H. Levitt, G. Bodenhausen and R.R. Ernst, Prog. NMR Spectrosc., 16, 163 (1983).
41. K.J. Packer and K.M. Wright, Mol. Phys., 50, 797 (1983).
42. A.C. Hearn, "REDUCE2 Implementation Guide for the General Computer", University of Utah Symbolic Computation Group Technical Report No. TR-7, June 1978.
43. P.L. Corio, "Structure of High-Resolution NMR Spectra", Academic Press, New York, 1966.
44. A. Bax, J. Magn. Reson., 52, 76 (1983).
45. D.M. Doddrell, J. Staunton and E.D. Laue, J. Magn. Reson., 52, 523 (1983).
46. R. Freeman, S.P. Kempell and M.H. Levitt, J. Magn. Reson., 38, 453 (1980).
47. R.R. Ernst, J. Chem. Phys., 45, 3845 (1966).
48. J.B. Grutzner and R.E. Santini, J. Magn. Reson., 19, 173 (1975).

49. W.A. Anderson and F.A. Nelson, *J. Chem. Phys.*, 39, 183 (1963).
50. V.J. Basus, P.D. Ellis, H.D.W. Hill and J.S. Waugh, *J. Magn. Reson.*, 35, 19 (1979).
51. M.H. Levitt, T.A. Frenkiel and R. Freeman, *J. Magn. Reson.*, 47, 328 (1982).
52. D.T. Pegg, M.R. Bendall and D.M. Doddrell, *J. Magn. Reson.*, 49, 32 (1982).
53. M.H. Levitt, G. Bodenhausen and R.R. Ernst, *J. Magn. Reson.*, 53, 443 (1983).
54. M.H. Levitt, O.W. Sorenson and R.R. Ernst, *Chem. Phys. Lett.*, 94, 540 (1983).
55. M.R. Bendall and D.T. Pegg, *J. Magn. Reson.*, 53, 144 (1983).
56. D.T. Pegg and M.R. Bendall, *J. Magn. Reson.*, 55, 114 (1983).
57. T.T. Nakashima, B.K. John and R.E.D. McClung, *J. Magn. Reson.*, 57, 149 (1984).
58. A. Bax, R. Freeman and T.A. Frenkiel, *J. Am. Chem. Soc.*, 103, 2102 (1981).
59. A. Bax, R. Freeman and S.P. Kempell, *J. Am. Chem. Soc.*, 102, 4849 (1980).
60. D.P. Burum and R.R. Ernst, *J. Magn. Reson.*, 39, 163 (1980).
61. G.A. Morris, *J. Magn. Reson.*, 41, 185 (1980).

62. O.W. Sorenson, R. Freeman, T.A. Frenkiel, T.H. Mareci and R. Schuck, *J. Magn. Reson.*, 46, 180 (1982).
63. A. Bax, R. Freeman, T.A. Frenkiel and M.H. Levitt, *J. Magn. Reson.*, 43, 478 (1981).
64. A. Bax, S.P. Kempell and R. Freeman, *J. Magn. Reson.*, 41, 349 (1980).
65. K.J. Packer, *Prog. NMR Spectrosc.*, 3, 87 (1967).
66. A. Abragam, "The Principles of Nuclear Magnetism", Oxford Clarendon Press, 1961.
67. F. Bloch, *Phys. Rev.*, 70, 460 (1946).
68. J.R. Lyerla, Jr. and G.C. Levy, *Topics in Carbon-13 NMR Spectroscopy*, 1, 79 (1974).
69. H.W. Spiess, *NMR Basic Principles and Progress*, 15, 55 (1978).
70. H.G. Hertz, *Prog. NMR Spectrosc.*, 3, 159 (1967).
71. T.C. Farrar, A.A. Maryott and M.S. Malmberg, *Ann. Rev. Phys. Chem.*, 23, 193 (1972).
72. D.E. Woessner, *J. Chem. Phys.*, 37, 647 (1962).
73. D.E. Woessner, B.S. Snowden, Jr. and G.H. Meyer, *J. Chem. Phys.*, 50, 719 (1969).
74. H.W. Spiess, D. Schweitzer, U. Haeberlen and K.H. Hausser, *J. Magn. Reson.*, 5, 101 (1971).
75. A.A. Maryott, T.C. Farrar and M.S. Malmberg, *J. Chem. Phys.*, 54, 64 (1971).

76. J. DeZwaan, R.J. Finney and J. Jonas, J. Chem. Phys., 60, 3223 (1974).
77. R.G. Gordon, J. Chem. Phys., 44, 1830 (1966).
78. M. Fixman and K. Rider, J. Chem. Phys., 51, 2425 (1969).
79. R.E.D. McClung, J. Chem. Phys., 51, 3842 (1969).
80. R.E.D. McClung and H. Versmold, J. Chem. Phys., 57, 2596 (1972).
81. J.B. Lambert, R.J. Nienhuis and J.W. Keepers, Angew. Chemie, 20, 487 (1981).
82. J.G. Powles, in "Magnetic Resonance and Relaxation", R. Blinc, Ed., North Holland Publishing Company, Amsterdam, 1967.
83. H.C. Torrey, Phys. Rev., 92, 962 (1953).
84. P.S. Hubbard, Phys. Rev., 131, 275 (1963).
85. I. Oppenheim and M. Bloom, Can. J. Phys., 39, 845 (1961).
86. P.S. Hubbard, Phys. Rev., 131, 1155 (1963).
87. D.K. Green and J.G. Powles, Proc. Phys. Soc., 85, 87 (1965).
88. C.H. Wang, J. Magn. Reson., 9, 75 (1973).
89. W.H. Flygare, J. Chem. Phys., 41, 793 (1964).
90. P. Debye, "Polar Molecules", Dover Publications, Inc., New York, 1945.

91. N. Bloembergen, E.M. Purcell and R.V. Pound, Phys. Rev., 73, 679 (1948).
92. W.A. Steele, J. Chem. Phys., 36, 2404, 2411 (1963).
93. H. Shimizu, J. Chem. Phys., 43, 2453 (1965).
94. H. Shimizu, Bull. Chem. Soc. Japan, 39, 2385 (1966).
95. R.E.D. McClung, J. Chem. Phys., 54, 3248 (1971).
96. R.E.D. McClung, J. Chem. Phys., 55, 3459 (1971).
97. R.D. Mountain, J. Chem. Phys., 51, 3243 (1971).
98. R.E.D. McClung, J. Chem. Phys., 57, 5478 (1972).
99. A.G. St. Pierre and W.A. Steele, J. Chem. Phys., 57, 4638 (1972).
100. F. Bliot, C. Abbar and E. Constant, Mol. Phys., 24, 241 (1972).
101. F. Bliot and E. Constant, Chem. Phys. Lett., 18, 253 (1973).
102. T.E. Eagles and R.E.D. McClung, Chem. Phys. Lett., 22, 414 (1973).
103. J.C. Leicknam, Y. Guissani and S. Bratos, J. Chem. Phys., 68, 3380 (1978).
104. M. Bloom, F. Bridges and W.N. Hardy, Can. J. Phys., 45, 3533 (1967).
105. R.E.D. McClung, Adv. Mol. Rel. Int. Processes, 10, 83 (1977).
106. J. Homer, A.R. Dudley and W.R. McWhinnie, J. Chem. Soc. Chem. Commun. No. 23, 893 (1973).

107. P.G. King and S.N. Deming, *Anal. Chem.*, 46, 1476 (1974).
108. R.L. Streever and H.Y. Carr, *Phys. Rev.*, 121, 20 (1961).
109. Dinesh, M.T. Rogers and G.D. Vickers, *Rev. Sci. Instrum.*, 43, 555 (1972).
110. Dinesh and M.T. Rogers, *J. Chem. Phys.*, 56, 542 (1972).
111. H.T. Edzes, *J. Magn. Reson.*, 17, 301 (1975).
112. H.Y. Carr and E.M. Purcell, *Phys. Rev.*, 94, 630 (1954).
113. D.E. Woessner, *Rev. Sci. Instrum.*, 31, 1146 (1960).
114. D.M. Cantor and J. Jonas, *J. Chem. Phys.*, 28, 157 (1977).
115. E.O. Stejskal and J.E. Tanner, *J. Chem. Phys.*, 42, 288 (1965).
116. E. von Meerwall, R.D. Burgan and R.D. Ferguson, *J. Magn. Reson.*, 34, 339 (1979).
117. S. Meiboom and D. Gill, *Rev. Sci. Instrum.*, 29, 688 (1958).
118. L.A. Woolf, *J. Chem. Soc. Faraday Trans. I*, 71, 784 (1975).
119. M.A. McCool, A.F. Collings and L.A. Woolf, *J. Chem. Soc. Faraday Trans. I*, 68, 1489 (1972).

120. J.M. Le Carpentier, R. Schlupp and R. Weiss, *Acta Cryst.*, B28, 1278 (1972).
121. W.H. Flygare and J. Goodisman, *J. Chem. Phys.*, 49, 3122 (1968).
122. J.A. Ibers and J.D. Swalen, *Phys. Rev.*, 127, 1914 (1962).
123. J.A. Pople, W.G. Schneider and H.J. Bernstein, "High Resolution Nuclear Magnetic Resonance", John Wiley & Sons, Inc., New York, 1959.
124. P.B. Davis, R.M. Neuman, S.C. Wofay and W. Klemperer, *J. Chem. Phys.*, 55, 3564 (1971).
125. L. Krause and M.A. Whitehead, *Mol. Phys.*, 23, 547 (1972).
126. D.E. Woessner, *J. Chem. Phys.*, 42, 1855 (1965).
127. A.I. Andreeva, V.L. Matukhin, D.Ya. Osokin and I.A. Safin, *Sov. Phys. Solid State*, 15, 2270 (1974).
128. J.P. Jacobsen and K. Schaumburg, *J. Magn. Reson.*, 28, 191 (1977).
129. W.J. Caspary, F.S. Millet, M. Reichbach and B.P. Dailey, *J. Chem. Phys.*, 51, 623 (1969).
130. P.K. Bhattacharya and B.P. Dailey, *J. Chem. Phys.*, 63, 1336 (1975).
131. F.S. Millet and B.P. Dailey, *J. Chem. Phys.*, 56, 3249 (1972).

132. H.H. Mantsch, H. Saito and I.C.P. Smith, Prog. NMR Spectrosc., 11, 211 (1977).
133. K.F. Kuhlmann and D.M. Grant, J. Chem. Phys., 55, 2998 (1971).
134. J.R. Lyerla, Jr. and D.M. Grant, J. Phys. Chem., 76, 3213 (1972).
135. B.K. John and R.E.D. McClung, J. Magn. Reson., 50, 267 (1982).
136. D.W.G. Smith and J.G. Powles, Mol. Phys., 10, 451 (1966).
137. Y. Margalit, J. Chem. Phys., 55, 3072 (1971).

B30424